KfK 3794
August 1984

I. Materials Analysis by Ion Backscattering and Channeling
II. Materials Modification by Ion Irradiation and Implantation

O. Meyer
Institut für Nukleare Festkörperphysik

Kernforschungszentrum Karlsruhe

KERNFORSCHUNGSZENTRUM KARLSRUHE

Institut für Nukleare Festkörperphysik

KfK 3794

I. MATERIALS ANALYSIS BY ION BACKSCATTERING AND CHANNELING

II. MATERIALS MODIFICATION BY ION IRRADIATION AND IMPLANTATION

O. Meyer

Kernforschungszentrum Karlsruhe mbH, Karlsruhe

Kernforschungszentrum Karlsruhe GmbH
ISSN 0303-4003

ABSTRACT

A description will be given of the basic processes occuring during ion implantation and ion beam analyses. The usefulness of the backscattering and channeling technique is demonstrated by a discussion of the applications to thin film analysis, studies of diffusion and reactions in thin films, lattice location investigations, disorder analysis and surface studies.

Ion implantation is a valuable research tool in metallurgy. The process operates very far from equilibrium conditions and thus will influence near surface properties in a unique way. The observed modifications are related to special microscopic structures which will be considered in detail.

I. Materialanalyse mit Hilfe der Ionenrückstreuung und des Channellingeffektes

II. Materialmodifikation durch Ionenbestrahlung und Ionenimplantation

ZUSAMMENFASSUNG

Nach einer Einführung in die Grundlagen der Ionenimplantation und der Ionen-Rückstreu- und Channeling-Analysenmethode wird anhand von ausgewählten Beispielen der Einsatz der Ionenimplantation zur gezielten Veränderung der Eigenschaften von Oberflächenschichten demonstriert. Ionenstrahlanalysenmethoden sind zur Charakterisierung dieser Schichten besonders geeignet.

Foreword and Acknowledgement

The methods of ion beam analyses and ion beam modification of materials are well documented in the literature. The purpose of this summary which has been presented as lectures at the University of Pretoria, 1978, and at the Nathiagali Summer School, Islamabad, 1982, is to give an extended introduction into the basic processes underlying these techniques and to present a summary of the results which have been obtained by improving these methods and applying them to solid state analyses and modification at the Institut für Nukleare Festkörperphysik in the last 15 years.

The author would like to thank his colleagues at the INFP - J. Geerk, E.L. Haase, M. Kraatz, G. Linker, F. Ratzel and R. Smithey for constructing, maintaining and operating the equipment and for the collaboration research that has been the basis of the largest part of this article. In the course of the years many guests and students have worked with us for a few months or years and have considerably contributed to the results which are partly summarized below. Their contributions to our research program are highly appreciated. Finally, we acknowledge the cooperation of the accelerator group A. Ernst and D. Roller for providing the light ion beams.

Contents:

I. MATERIALS ANALYSIS BY ION BACKSCATTERING AND CHANNELING

INTRODUCTION

All methods of material analysis by target stimulation using photons, electron or ions yield a mixture of quantitative and qualitative information. Techniques such as photo-electron-spectroscopy or electron-energy-loss-spectroscopy usually provide information on the electronic structure of the material and on chemical binding however are not quantitative in respect of element analysis. Energetic ion beams with energies between about 100 and 3000 keV interacting with the target usually yield quantitative information however do not provide binding information at all.

The use of energetic ion beams for solid state analytical work has expanded rapidly during the last two decades, largely because of the development of improved data precessing equipment and of high-resolution nuclear particle detectors, which provide an energy-proportional signal with an energy resolution of about 1%. In normal backscattering analysis geometry the depth resolution is about 10 to 20 nm. With the newly developed electrostatic analysers the depth resolution is about 0.5 nm. The region of application is wide spread and includes:

a) thin film analysis: determination of composition and impurity content, diffusion and reaction between thin film-couples, oxidation, analysis of semiconductor doping.

b) single crystal analysis: combined with the channeling effect in single crystals energetic ion beams can be use to determine regular interstitial and substitutional lattice sites of foreign atoms in host materials with high spacial resolution ($\sim 2 \cdot 10^{-3}$ nm), crystalline disorder and radiation damage in materials, relaxation- and reconstruction phenomena on single crystalline surfaces as well a lattice site determination of adsorbed atoms.

c) analysis of environmental, biological, geophysical and other problems mainly using the proton-microprobe with a greatly reduced background radiation as compared to the electron-microprobe.

This list is by far not complete. The whole field is well documented and nearly complete information can be obtained from books and conference proceedings listed in ref. 1 to 7. In ref. 7

a comprehensive and recent bibliography is given in the field of ion beam surface modification and analysis.
Besides Rutherford backscattering one can use other close encounter processes such as nuclear reactions, proton-induced X-rays and ion-induced Auger-electrons for materials analyses with ion beams.

In the following lectures however we will concentrate on materials analysis by backscattering and by ion channeling. A few of our experimental results are presented as examples to demonstrate the usefulness of these techniques.

I. Backscattering Spectrometry

1. Equipment

Backscattering of charged particles produced in accelerators is a well-known method used for the analysis of surfaces /8/. Backscattering of He-ions from radioactive sources, for example, was applied for chemical analysis of the lunar surface /9/. The He-ion beam generated in an accelerator has the advantage of a far higher source strenght to energy resolution ratio. This makes if possible to look at small solid angles of the backscattering particles so that the energy spread caused by kinetics is small compared with the energy resolution of the detecting system. A typical experimental arrangement is shown in Fig. 1. A well collimated monoenergetic ion beam with energies between about 200 keV and 3000 keV is delivered by a Van-de-Graaff accelerator (the lower energy limit is given if one wants to avoid neutralization effects, the upper limit is due to the occurence of deviations in the Rutherford cross section by resonance scattering; both effects would influence quantitative analysis). The beam current is measured with an integrator; the target is shielded with a Faraday cup to avoid errors by secondary electron emission. The energy distribution of the backscattered He-ions is measured with a surface barrier detector. The electrical signal from this detector is amplified and stored in a pulse height analyser. The linear response of the nuclear

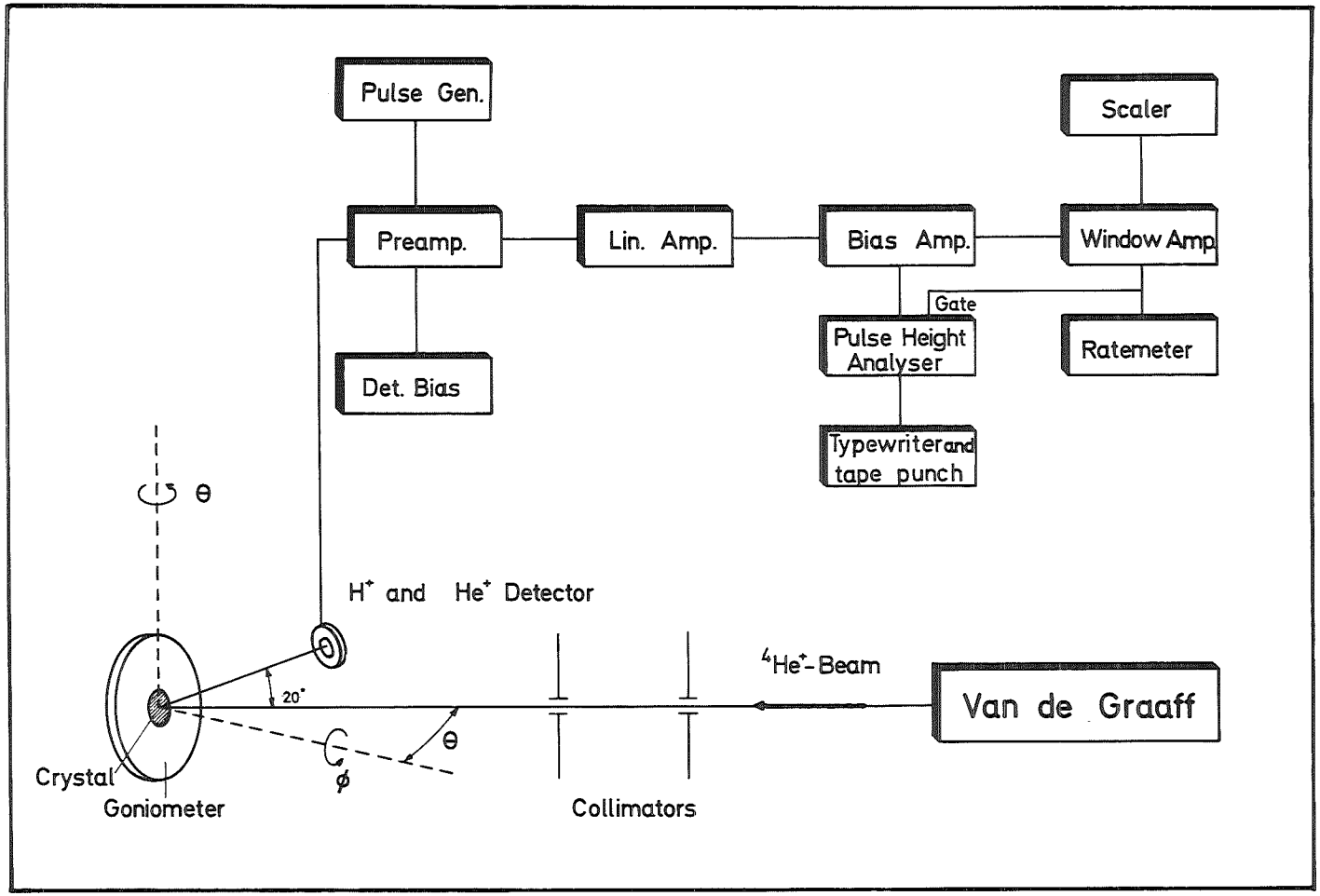

Fig. 1: Schematic illustration of the experimental arrangement together with the electronic instrumentation for the energy analysis of back-scattered particles.

particle detector provides a fixed energy per channel in the multichannel analyser. In order to include the material analysis by ion channeling in single crystalline targets, which will be discussed in chapter II, the samples are mounted on a two axis goniometer to permit the alignment of the ion beam with one of the low index crystal directions.

1.1 Energy Resolution

At energies of 2 MeV the energy resolution $\Delta E/E$ is usually not limited by the energy straggling of the accelerated ion beam but by the energy-resolution of the nuclear particle detector and the noise of the first stage in the preamplifier. Typical values for $\Delta E/E$ are 0.1% for the ion beam and 0.7% for the nuclear particle detector. The backscattered ion must be stopped in the depleted region of the p-n junction of the silicon-surface barrier detector. The stopping process is due to inelastic interaction of the incident ions with the electrons, called electronic stopping and due to elastic interaction with the target atoms via a partially screened Coulomb-potential, called nuclear stopping. During the slowing down process of 2 MeV He-ions in silicon about 99% of the energy is lost due to electronic stopping thus producing electron-hole pairs which are seperated by the strong electrical field gradient in the p-n junction and which produce the electric signal of the detector. The straggling in the nuclear energy loss will limit the energy resolution of the nuclear particle detector to about 10 keV. Together with the preamplifier noise the typical energy resolution for the detecting system is about 15 keV for 2 MeV He-ions.

1.2 Mass Resolution

The energy of a light ion scattered by an atom at the surface is K^2E_1, where K^2 is the fractional energy loss after scattering given by:

$$K^2 = E_2E_1 = [m \cdot \cos\Theta_2 + (M^2-m^2\sin^2\Theta_2)^{1/2}]^2/(m+M) \quad (1)$$

Here m is the mass of the incident light ion, M that of the target atom, Θ_2 is the scattering angle in laboratory coordinates and E_1 and E_2 are the energies of the incident and reflected ion, respectively. From eq. (1) it can be estimated that the mass resolution which will be defined as the difference in reflected ion energies for scattering from surface atoms with mass M and M+1, is rather high considering incident He-ions and target atoms with masses $\leq$ 50 however decreases strongly for M > 50. The situation can be improved using a heavy mass incident ion for example ^{16}O-ions /10/. The improved mass resolution for ^{16}O-ions is demonstrated in Fig. 2, where backscattering spectra from 2.4 MeV He-ions and 20 MeV ^{16}O-ions are compared. The calibration target consisted of 5 nm thick layers of Au, Ag and Cu evaporated on a Si slice. In the case of ^{16}O-scattering, ^{65}Cu is clearly separated from ^{63}Cu; the gain in mass resolution for M > 50 is about a factor of 4 compared to the results from ^{4}He-scattering.

1.3 Depth Resolution

Treating the mass resolution in chapter 1.2 we have considered the scattering event to occur with atoms at the surface. If the scattering event occurs at a depth t we have to take into account the energy loss due to inelastic collisions with the target electrons. If E' is the energy of the incident ion, then the energy E_1 just before collision after penetrating the surface layer to depth t is given by

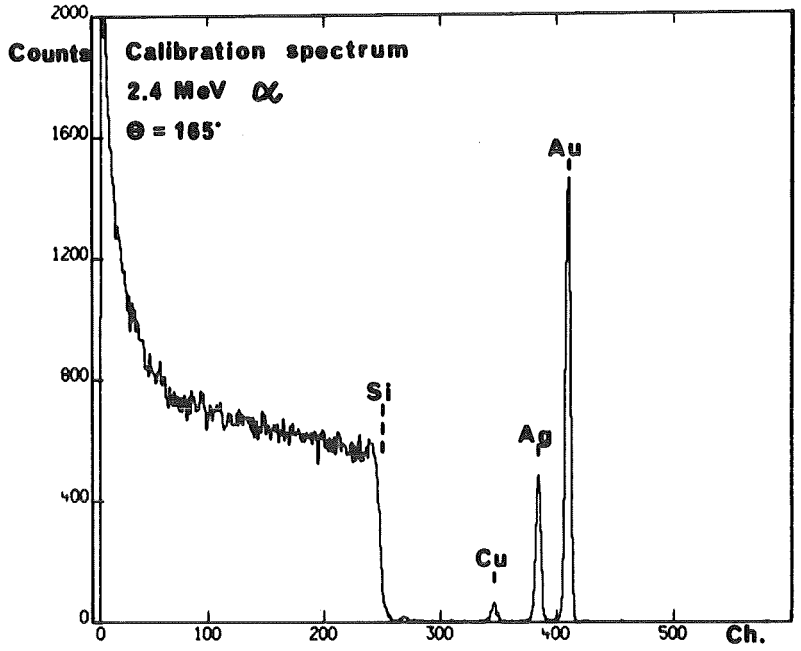

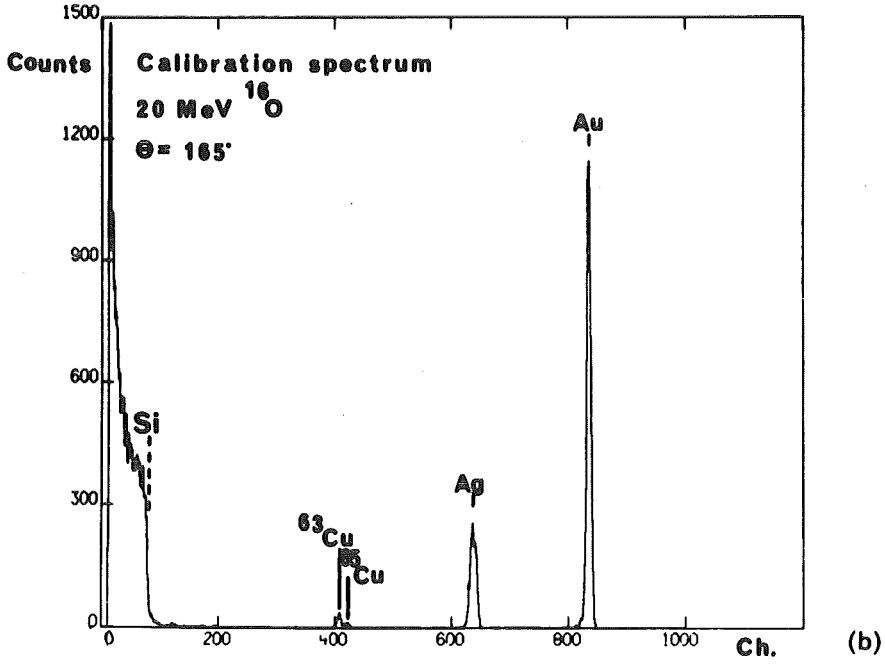

Fig. 2: Backscattered energy spectrum for 2.4 MeV He-ions (Fig. 2a) and for 20 MeV ^{16}O-ions (Fig. 2b). The target consisted of thin Au, Ag und Cu-films evaporated onto Si.

$$E_1 = E' - \left| \int_0^t \frac{dE}{dx}\, dx \right| \qquad (2)$$

The energy E_2 immediately after elastic collision at depth t is given by

$$E_2 = K^2 \cdot E_1 \qquad (3)$$

and E'', the energy of the outgoing particle as measured with the nuclear particle detector at an angle Θ ($= 180° - \Theta_2$) is given by

$$E'' = E_2 - \left| \int_0^t \frac{dE}{dx} \frac{dx}{\cos\Theta} \right| \qquad (4)$$

Inserting eqs. (3) and (2) in (4)

$$E'' = K^2 \cdot E' - \left| K^2 \cdot \int_0^t \frac{dE}{dx}\, dx \right| - \left| \int_0^t \frac{dE}{dx} \frac{dx}{\cos\Theta} \right| \qquad (5)$$

Since dE/dx changes only slowly with energy, average values of dE/dx can be used for the incoming and outgoing path respectively. Then

$$E'' \cong K^2 E' - t \cdot [S] \qquad (6)$$

where we define [S], the backscattering energy loss parameter, by

$$[S] \equiv K^2 \frac{dE}{dx}\bigg|_{\bar{E}_1} + \frac{1}{\cos\Theta} \frac{dE}{dx}\bigg|_{\bar{E}_2} \qquad (7)$$

In this definition $\bar{E}_1$ and $\bar{E}_2$ are the intermediate energies between E' and E_1, and E_2 and E'', respectively. At the energies usually used, where $t \cdot [S] << E'$ one may take $\bar{E}_1 \cong E'$ and $\bar{E}_2 \cong E_2$ with negligible loss of accuracy. Thus for thin films with thicknesses up to about 500 nm the energy scale in a backscattering spectra can be converted to a mass scale by eq. (1) and into a depth scale by eq (6).

The backscattering energy loss parameter can be calculated by using tabulated dE/dx(E)-values /4,11/. It can also directly be determined by taking backscattering spectra from evaporated films of known thicknesses. In Fig. 3, a typical backscattering spectrum from a Mo-layer on a quartz substrate is presented, illustrating characteristic results for both thickness measurement with a stylus instrument and with a backscattering measurement /12/.

2. Applications

2.1 Thin Film Growth Processes

From the previous discussion it is clear that a backscattering analysis can quickly provide information on the thin film thickness and on the impurities present /12/. We can also show that this technique is suitable to study the intermediate stages of growth of thin films and the sticking probability factor. This possibility is demonstrated in Fig. 4 where the backscattering spectra are shown for Sn-films on Si /13/. Equal quantities of Sn have been evaporated on Si at substrate temperatures of 77, 293 and 393 K. A significant reduction in the yield can be seen for layers evaporated at higher temperature (393 K) indicating island growth, and a substantially reduced peak area at room temperature indicating a greatly reduced sticking factor at this temperature.

2.2 Compound Film Analysis

A fruitful area of application is the analysis of dielectric layers on semiconductors by ion backscattering. SiO_2- and Si_3N_4-amorphous layers are extensively used in silicon devices as diffusion masks and also as passivating and insulating layers. As backscattering measurements are useful in the analysis of the depth dependence of the composition and density of the nitride and oxide layers, the various deposition processes such as thermal oxidation, chemical vapor deposition, glow discharge, sputtering etc. can be quickly optimized. One of the earlier studies on the analysis of silicon-oxide layers on silicon surfaces is given in ref. 14.

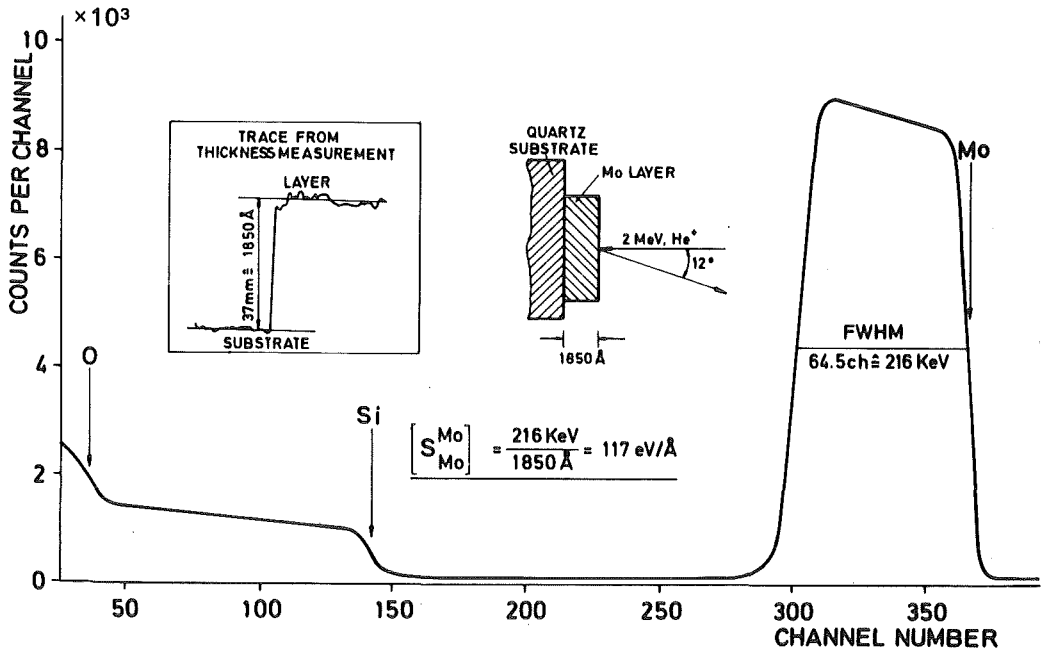

Fig. 3: A typical backscattering spectrum from a Mo layer evaporated on a quartz substrate. A trace from a stylus instrument for a thickness measurement of this layer is included together with a diagrammatic representation of the analysis geometry.

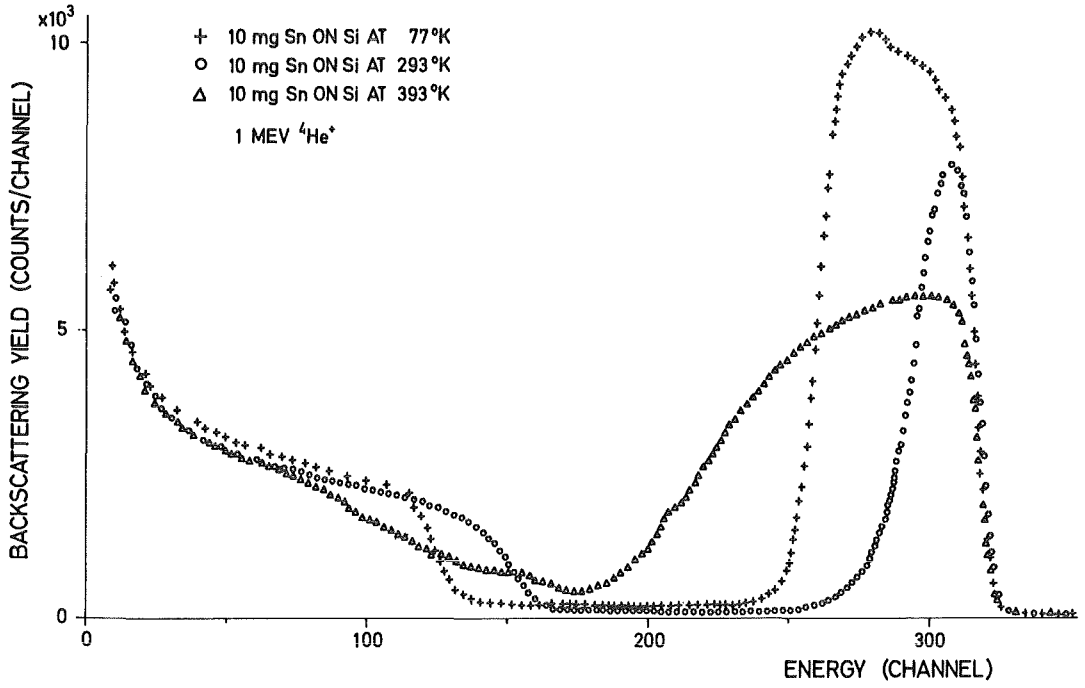

Fig. 4: Backscattering energy spectra from Sn-layers evaporated on Si. Equal amount of Sn were evaporated at 77 K (+), 293 K (0) and 393 K (Δ) substrate temperature.

Analyzing a compound A_mB_n we have to assume that the atomic stopping cross sections ε_A and ε_B, where $\varepsilon = \frac{dE}{dx} \cdot \frac{1}{N}$, can be added, weighted proportionally to their abundance in the compound. This postulation is known as Bragg's rule /15/. The specific energy loss for a compound is then given by

$$\left.\frac{dE}{dx}\right|^{AB} = \varepsilon_A N_A^{AB} + \varepsilon_B N_B^{AB} \qquad (8)$$

where AB stands for A_mB_n and N_A^{AB}, N_B^{AB} are the atomic densities of A and B atoms in AB respectively. Eq. (8) has now to be inserted in eq. (7) to give the backscattering energy loss parameter for light ions scattered at A-atoms $[S_A^{AB}]$ or B-atoms $[S_B^{AB}]$ in the compound where

$$[S_A^{AB}] = N_A^{AB}[\varepsilon_A] + N_B^{AB}[\varepsilon_B] \qquad (9)$$

with

$$[\varepsilon_A] = K_A^2\varepsilon_A\Big|_{E_1} + \frac{1}{\cos\theta}\,\varepsilon_A\Big|_{E_2} \quad \text{and} \quad [\varepsilon_B] = K_A^2\varepsilon_B\Big|_{E_1} + \frac{1}{\cos\theta}\,\varepsilon_B\Big|_{E_2}$$

For $[S_B^{AB}]$ K_A^2 has to be replaced by K_B^2 in $[\varepsilon_A]$ and $[\varepsilon_B]$. With these equations available one can determine the constituent atom ratio $Y = N_A^{AB}/N_B^{AB}$ in a compound by measuring the heights H_A^{AB} and H_B^{AB} (yield) from the A and B atoms in the backscattering spectrum

$$Y = \frac{[S_A^{AB}] \cdot H_A^{AB}\cdot\sigma_B}{[S_B^{AB}] \cdot H_B^{AB}\cdot\sigma_A} \qquad (10)$$

The scattering process due to Coulomb interaction can be described by the well-known Rutherford differential scattering cross section. In laboratory coordinates it is given by:

$$\frac{d\sigma}{d\Omega} = \left(\frac{Z_1Z_2e^2}{2E\,\sin^2\theta_2}\right)^2 \frac{\{\cos\theta_2 + [1 - (\frac{m}{M}\sin\theta_2)^2]^{1/2}\}^2}{[1 - \frac{m}{M}\sin\theta_2{}^2]^{1/2}}$$

Z_1 and Z_2 are the atomic number of the projectile and target atom. E is the energy of the projectile immediately before scattering and Θ_2 is the laboratory scattering angle. The average differential scattering cross section σ is taken over a finite solid angle, Ω, given by the sensitive area of the detector and the distance from the substrate. Knowing these numbers one could determine the total number of target atoms per unit area, $N\delta x$ from the height of the spectrum, H that is the number of counts per channel, on an absolute scale $H = Q\sigma\Omega N\delta x$ where Q is the total number of projectiles (charge). By use of [S] as defined in eq. (7) one obtaines

$$H = Q \cdot \sigma \cdot \Omega \cdot N \cdot \delta E/[S] \qquad \text{or}$$

$$H = Q \cdot \sigma \cdot \Omega \cdot \delta E/[\varepsilon]$$

where δE is the energy to channel conversion factor.

It is often more convenient to measure the composition on a relative scale by relating the height of an elemental target H_A to the height H_A^{AB} in a compound

$$Y = \frac{H_A^{AB}[\varepsilon_B]}{[\varepsilon_A](H_A - H_A^{AB})} \qquad (11)$$

Both methods have been applied for example for the analysis of reactively sputtered NbN-layers /16/. Such refractory compound with B1-crystal structures are known to have good superconducting properties. In Fig. 5 a typical backscattering spectrum from a NbN layer sputtered onto a carbon substrate (dashed line) is compared to a spectrum from a Nb layer evaporated onto quartz. The height of the Nb peak in the compound, R_{Nb}^{NbN} is strongly reduced as compared to the height R_{Nb}^{Nb} of the pure Nb layer. Eq. (11) can immediately be applied to determine Y, the ratio of the Nb to N atoms. Eq. (10) can be applied using the heights R_{Nb}^{NbN} and R_N^{NbN} as determined from the spectra. From these

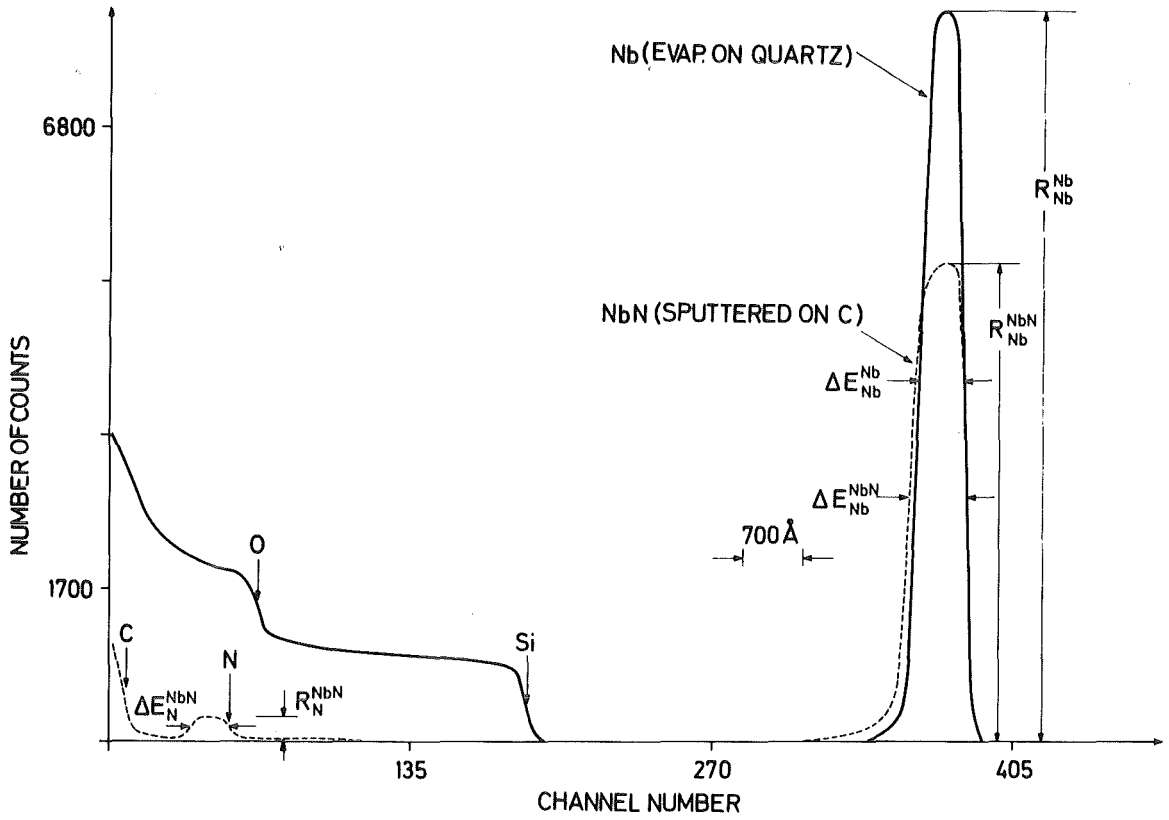

Fig. 5: Typical backscattering spectra from a Nb layer evaporated onto a quartz substrate (solid line) and from a NbN layer, reactively sputtered on a carbon substrate.

data we concluded that violations of Bragg's rule in nitrides are not larger than about 5%.

Compounds can also be produced by high dose ion implantation. Implantation at a single ion energy will produce a Gaussian shape distribution of the implanted species. In order to obtain a homogeneous profile several energies can be used and the fluences can be varied in such a way that a homogeneous implantation profile emerges. In Fig. 6 a calculated implantation profile is shown for N in Re. Energies and fluences used are indicated in Fig. 6. Except at the surface region, a reasonable homogeneous distribution is seen. The homogeneity of the implantation as a function of depth was tested with the backscattering spectrometry using 2 MeV He-ions. As an example, such spectra of a Re film before and after implantation of 45 at.% N are shown in Fig. 7. A decrease accompanied by a broadening of the implanted layer is seen as compared to the unimplanted sample. These effects are due to an increased energy loss of the He particles during their penetration of the implanted film. The total peak area which is independent of the energy loss, is proportional to the total number of Re atoms.

Thin film X-ray analysis showed that the hcp-crystal structure of Re was no longer present. The cubic NaCl-structure $Re_{55}N_{45}$ had formed during the implantation process /17/.

2.3 Diffusion Studies

Diffusion processes are important in the formation of metal electrodes and compounds in surface layers of crystals. An early example was the application of backscattering to study the diffusion of Au in Cu /18/. Further, diffusion processes are important during doping of semiconductors by ion implantation. Radiation enhanced diffusion during implantation or during annealing may significantly change the doping profile.

As an example, the change of an Sb-peak as a function of annealing time at a temperature of 900°C is shown in Fig. 8 /19/. Implantation of Sb in silicon samples was carried out at an ion energy of 400 keV using a dose of $8 \cdot 10^{14}$ Sb/cm^2 at room temperature. The implanted peak shape is nearly symmetric about the peak

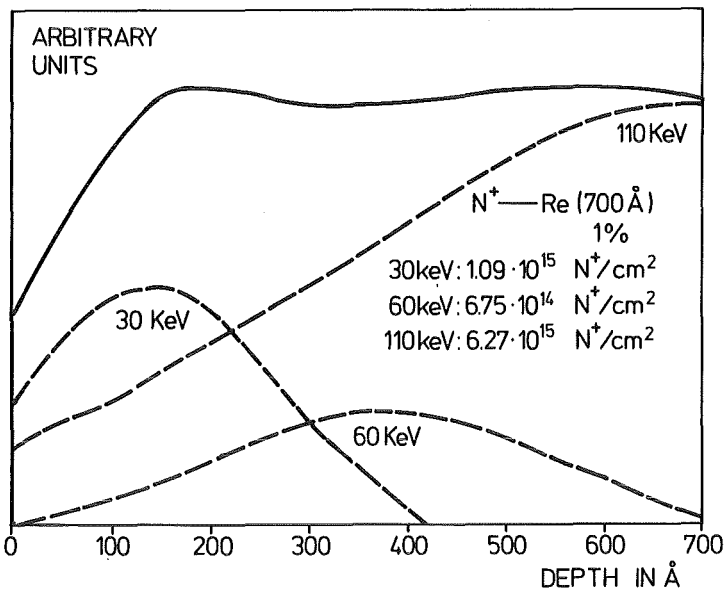

Fig. 6: Calculated implantation profile for N in Re. Energies and fluences are given for 1 at.% N.

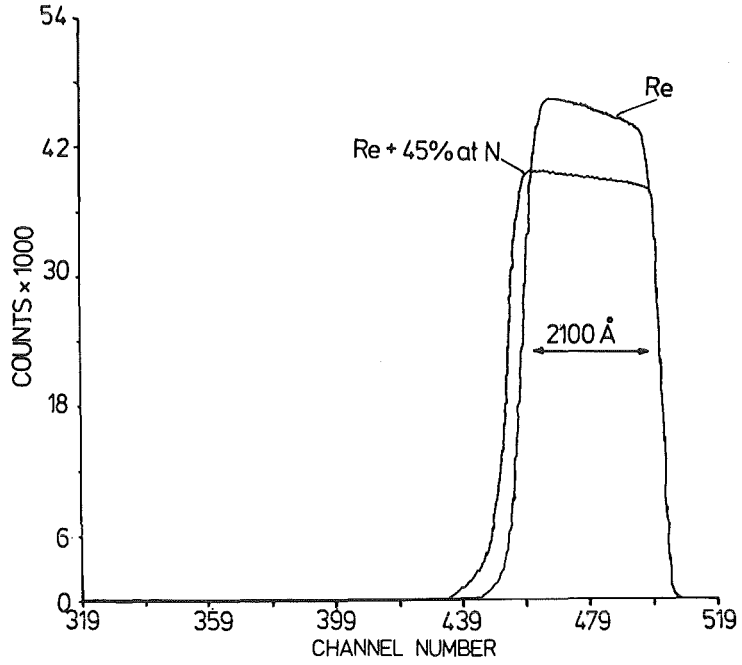

Fig. 7: Backscattering spectra of a Re film before and after implantation of 45 at.% N. The smoothness of the plateau indicates that the implanted ions are homogeneously distributed.

maximum. The number of implanted ions N_i/cm^2 can be calculated by comparing the area A_i from the impurity peak (here Sb) with the height of the silicon spectrum H_h (h = host) for random orientation:

$$N_i = \frac{A_i \cdot \sigma_h N_h \delta E}{H_h \sigma_i [S]_h} \qquad (12)$$

σ_h and σ_i are the Rutherford cross sections for the host and the impurity atom respectively ($\sigma \cong Z^2$); N_h ist the atomic density of the host and δE is the energy/channel conversion factor in the spectrum. Relating the peak area A_i to the height of the host spectrum has the advantage that the integrated charge and the solid angle of the detector cancel and need not to be considered. The as-implanted impurity peak profile can be described by the equation

$$n(x) = [N_i/(2\pi\Delta R_p^2)^{1/2}] \exp[-(x-R_p)^2/2\Delta R_p^2] \qquad (13)$$

where n is the concentration of the implanted ions and x is the distance from the surface. R_p is the mean projected range and ΔR_p is the standard deviation of the distribution. For a Gaussian shape, R_p coincides with the position of the peak maximum, whereas $2.35 \cdot \Delta R_p$ is equal to the full width at half maximum (FWHM). It can be shown that eq. (13) with ΔR_p replaced by $(\Delta R_p^2 + 2Dt)^{1/2}$ is a particular solution of the true diffusion equation where D and t are the diffusion coefficient and time, respectively. The dashed line shows the initial distribution of the implanted Sb atoms in Fig. 8. In the isothermal anneal sequences it can be seen that the distributions at lower channel numbers corresponding to deeper depth are relatively unchanged. However, there is a decrease observed in the height of the distribution and a broadening of the distribution towards the surface. The observed asymmetrical distribution indicates a non-constant diffusion coefficient throughout the implanted layer. The solid lines are calculated with a value of $D = 10^{-16}$ cm^2/sec (the normal value for Sb in Si at 900°C) for the deeper flank of the profile,where-

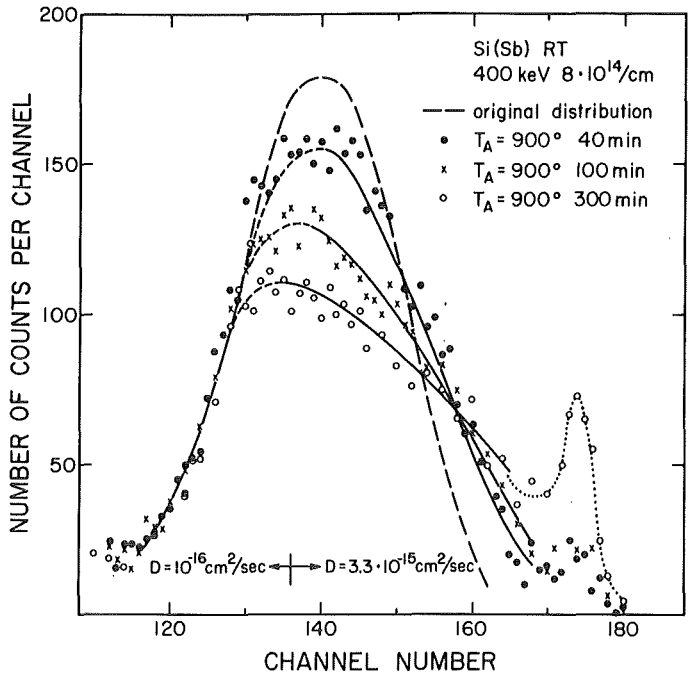

Fig. 8: Random energy spectra of He-ions backscattered from Sb atoms implanted in Si at 400 keV. 10 channels correspond to a depth of 0.56 nm.

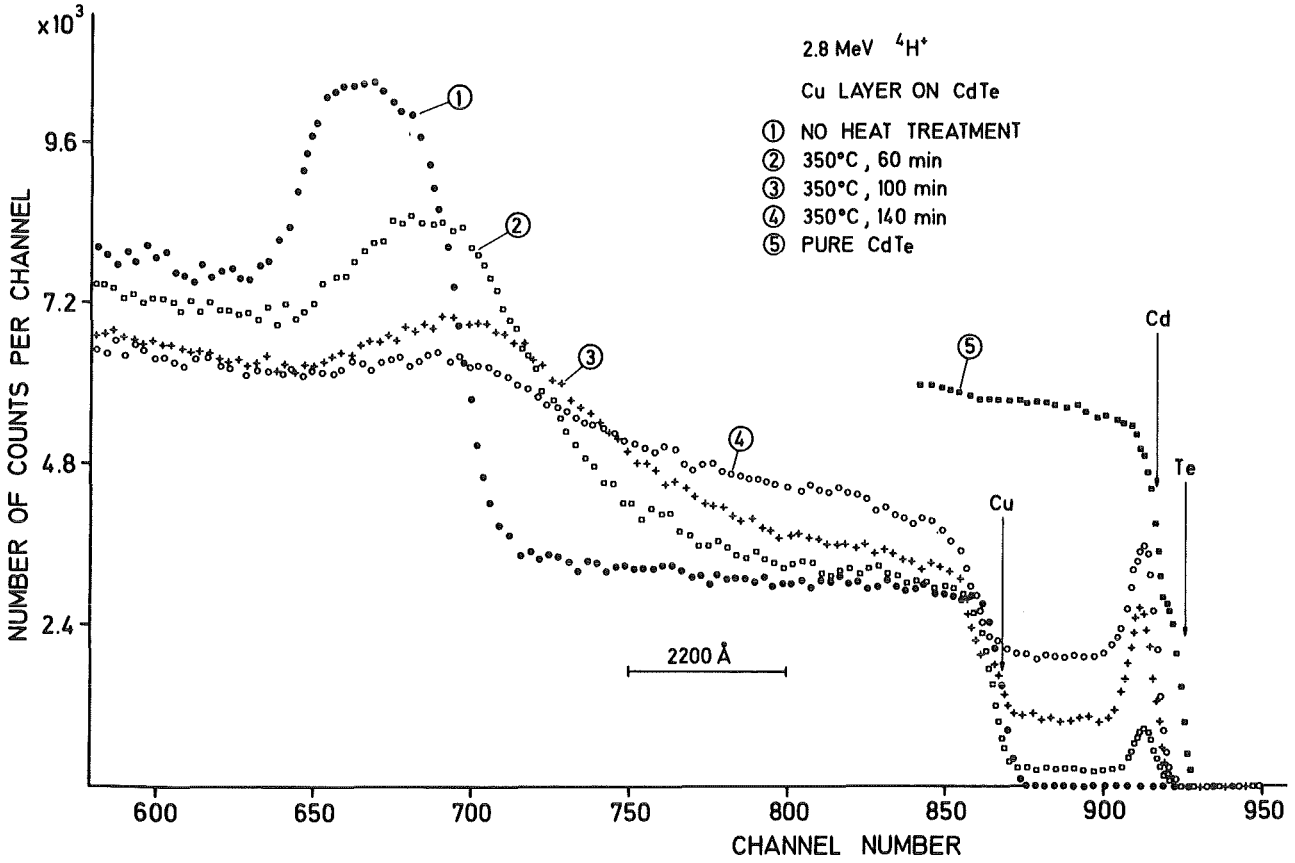

Fig. 9: Backscattering spectra illustrating outdiffusion of Cd through an evaporated layer of Cu on CdTe. By comparison with a spectrum for a CdTe crystal without a Eu layer it is clearly seen that Cd outdiffusion has occured.

as a D value of $3.3 \cdot 10^{-15}$ cm^2/sec described the peak decrease as well as the region from peak to surface. At the surface, the growth of a peak indicated that Sb atoms have diffused to the surface and become trapped. A more detailed description of enhanced diffusion and out-diffusion in ion implanted silicon is given in ref. 19.

As a last example diffusion processes at the Cu/CdTe interface for evaporated and chemically plated Cu layers are considered. Here the backscattering analysis allows the simultaneous measurement of compound formation and diffusion /20/. After evaporation of a thick Cu layer (about 1 µm) the backscattering spectrum is given by the curve No. 1 in Fig. 9. Due to the high energy loss of the He-ions in the Cu layer the energy of He ions scattered from the CdTe surface is shifted from channel 920 to channel 690. The energetic overlap of He-ions scattered from Cu and from CdTe produces a peak from channel 660 to 690. The step at channel 870 is the leading edge of Cu, the step at channel 695 is the leading edge of CdTe and the step at channel 660 is the trailing edge of Cu. During successive heat treatments at 320°C (not shown in Fig. 9) the thickness of the Cu-layer decreases, causing the leading edge for CdTe and the trailing edge for Cu to move towards higher energy. This process is also seen for spectrum No. 2 in Fig. 9. Besides the indiffusion of Cu, which leads to the observed shifts as discussed above it is clearly seen in Fig. 9 that Cd diffuses through the Cu layer and precipitates at the surface. With increasing annealing time the Cu layer is enriched with Cd. From measurements at different temperatures the diffusion coefficient D for Cu in CdTe could be determined /20/.

II. Ion Channeling in Materials Analyses

3. Introduction

The motion of energetic charged particles in a crystalline target is strongly influenced by directional effects due to densely packed rows or planes of atoms in the crystal lattice. This phenomenon called channeling was first discovered by computer studies /21/, simulating the slowing down process of charged particles in materials taking the lattice structure into account. The influence of the channeling effect on the ranges and range distributions of charged particles was far more pronounced in experiments, using single crystalline targets and perfect alignment between the incident beam direction and low index crystal directions /22,23,24/. Since this late discovery of the channeling effect numerous studies have been performed on the principles as well as on the applications of this effect for materials characterization. Excellent reviews have been published /25,26,27/ which provide detailed and comprehensive treatment of the subject. The intention of this review is to give a short introduction and to summarize recent development in three main fields of application, namely:

a) foreign atom location b) radiation damage c) surface studies.

From the computer studies it was concluded that the channelled particles experience many glancing collisions with atoms in successive lattice planes. This leads to the simple concept that the potential in binary collisions between charged particles and crystal atoms can be replaced by a potential, U(r), between the particle and a string of atoms /27/ characterized only by the distance d between neighbored atoms in the string. A characteristic angle ψ_1 exists, called Lindhard's characteristic angle, separating particles with glancing collisions from those with $\psi > \psi_1$ which will not feel the steering force of densely packed rows or planes. $\psi_1 = (2Z_1Z_2e^2/(dE))^{1/2}$ where Z_1 and Z_2 are the atomic numbers of the particle and atom respectively and E is the particle energy. For a charged particle moving in a channel bordered by atomic planes or rows, in a first approximation, neglecting inelastic

energy lossed due to interactions with electrons, the transverse energy is conserved. The total transverse energy $E_\perp$ is the sum of the transverse potential energy, U(r), and the transverse kinetic energy, $E \cdot \psi^2(r)$.

Assuming that this transverse energy remains constant, the motion of the particle with $E_\perp$ is restricted to an area $A(E_\perp)$ in the xy-plane within the channel where $E_\perp > U(r_{in})$. $U(r_{in})$ is the potential energy which the ion obtains when entering the channel at a position r_{in} away from the potential minimum at r = 0. $A(E_\perp)$ is a function of E, ψ and r_{in} and there is an equal probability of finding the ion anywhere within this area. Considering a beam of particles uniformly incident over the total channel area, we may add up these uniform distributions inside the various areas $A(E_\perp)$. This will lead to a high flux density in the middle of the channel in the region of lowest U(r). The knowledge of such flux peaking effects and flux depression near the atomic rows is necessary for the determination of regular interstitial lattice sites and of the lateral distribution of lattice defects. Conservation of transverse energy and flux peaking are the most important features of the channeling effect.

4. Lattice location of foreign atoms

Physical properties of materials are determined by the specific location of foreign atoms in the host lattice. Information on the lattice sites can be obtained by using the angular dependence of close impact parameter events such as Rutherford scattering, nuclear reactions or ion-induced X-rays in ion channeling experiments.

4.1 Backscattering spectra and substitutional lattice positions of impurity atoms

Rutherford backscattering is the most widely used close-encounter process in channeling studies. The experimental arrangement is schematically shown in Fig. 1 and has been described in chapter I.

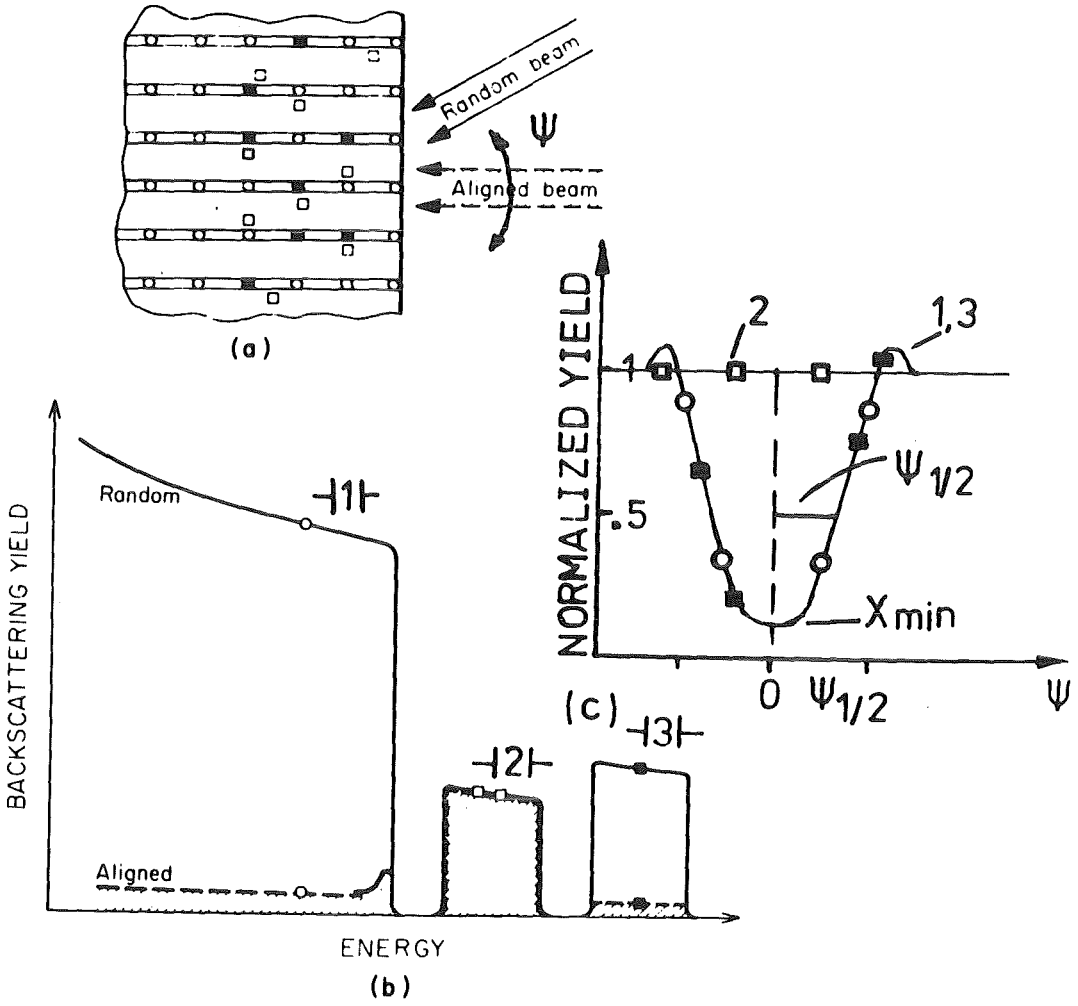

Fig. 10: Schematic random and aligned backscattering spectra (a) for MeV He-ions incident on a single crystal containing heavy impurity atoms (b) on substitutional (■) and on random interstitial (□) sites. Angular yield curves when measured in windows 1 to 3 are shown in (c).

Fig. 10a schematically illustrates the incident beam well aligned or randomly oriented with respect to the atomic rows. Indicated in Fig. 10a are the host atoms with mass M_2 (o), foreign atoms on random interstitial lattice sites M_3 (□) and foreign atoms on substitutional lattice sites M_4 (■) with the assumption $M_4 > M_3 > M_2$. Typical backscattering energy spectra are shown in Fig. 10b for the random as well as for the aligned beam. Particles backscattered from target atoms of different masses near the surface are seen to be well seperated on the energy scale. Particles from target atoms at some depth suffer an energy loss due to inelastic interactions with electrons and will produce nearly rectangular shaped spectra as shown schematically in Fig. 10b. The energy scale can be converted into a mass scale and into a depth scale (see chapter 1.3).

When the beam is aligned with an axial direction, about 95 to 98% of the incident particles will be steered by the strings of atoms (channelled component) and a strong reduction of the backscattered yield from the lattice atoms as well as from substitutional impurity atoms is noted in Fig. 10b. The backscattered yield as a function of the angle ψ between random and aligned incidence when monitored in the energy windows 1 to 3 and normalized to the random yield is shown in Fig. 10c. These angular yield curves are characterized by two important quantities: the minimum yield, χ_{min} for perfect alignment and the critical angle, $\psi_{1/2}$, the half angle at height $(1-\chi_{min})/2$.

In Fig. 10c it can be seen that if χ_{min} and $\psi_{1/2}$ for the host lattice and the substitutional impurity atoms are the same, 100% of the impurity atoms occupy substitutional sites. The substitutional fraction, f_s is determined by $f_s = (1-\chi_i)/(1-\chi_h)$ were χ_i and χ_h are the normalized minimum yields for the impurity and the host respectively. No reduction of the yield is shown for mass M_3, indicating that those impurity atoms are localized at random interstitial sites.

For precise lattice location studies it is most important to take complete angular yield curves as is demonstrated in Figs. 11a and b for Ga implanted in an Al-single crystal /28/ at room temperature.

In the as-implanted sample $\psi_{1/2}$ for Ga is smaller and χ_{min} larger than the values measured for the host. This indicates that Ga is slightly off the substitutional lattice site (about 0.015 nm), presumably because Ga atoms have a disturbed neighborhood, for example a neighbored Ga-atom or a vacancy. After annealing with short electron pulses with a width of about 150 nsec and a total energy of 2.4 J/cm^2 (4 steps with 0.6 J/cm^2) a complete annealing and a substitutional fraction of 1 is reached as is demonstrated in Fig. 11b.

4.2 Analysis of angular yield curves and lattice vibrations

The $\psi_{1/2}$- and the χ_{min}-values may be compared to calculated values using the empirical formuls from Barrett /29/ based on Monte Carlo computer calculations:

$$\psi_{1/2} = 0.8\ F_{RS}\ (1.2\ U_1/a)\ \psi_1 \quad \text{and} \quad \chi_{min} = 18.8\ N\,d\,U_1^2$$

The Thomas-Fermi screening radius a is given by $a = 0.885\ a_o (Z^{2/3}+Z^{2/3})^{1/2}$ where a_o is the Bohr radius (a_o = 0.0528 nm). The one-dimensional rms thermal vibration amplitude U_1 is calculated from Debye theory of thermal vibrations:

$$U_1 = 1.21\ [\Phi(x)/x + .25)/M_2\Theta_D]^{1/2} \quad \text{in nm,}$$

where Θ_D is the Debye temperature in K and $\Phi(x)$ the Debye function with $x = \Theta_D/T$. F_{RS} and $\Phi(x)$ are tabulated in /12/ and /7/ respectively. N is the number of host atoms per unit volume.

Analysis of angular dependent backscattering spectra from crystals with complicated structures and with defects can be performed using Monte Carlo computer calculations /30/. For compounds with parallel rows of atoms with different atomic numbers and anisotropic lattice vibrations a detailed knowledge of the flux profile is required for the quantitative analysis of the channeling results. In such programs the elastic interaction between incident ions and the lattice atoms is treated

as a series of independent binary collisions. For the calculation of the deflection angle at each interaction the classical scattering theory in momentum approximation is used /31/. The Moliére-approximation /32/ to the Thomas-Fermi potential is used as scattering potential. The electronic energy loss is calculated from an impact-parameter-dependent term due to collisions with closed-shell electrons and from a constant part, which is due to collisions with valence electrons which are treated to be equally spread over the lattice, and to plasma excitations. The energy loss due to nuclear interaction is neglected since the ion energies are in the MeV-region. The mean squared angular spread of the channelled beam due to multiple scattering from electrons, directly proportional to the inelastic energy loss rate, is also included in such programs. The influence of amorphous surface layers on the divergence of the beam can also be simulated by choosing the transverse momentum of the starting ion from a Gaussian distribution.

As an example of such a computer calculation, channeling results from the compound V_3Si, a superconductor with A15 crystal structure, are compared with calculated values in Fig. 12a,b /33/.

Good agreement is obtained between calculated and measured angular yield curves for the V - as well as for the Si-sublattices. Protons from the $^{28}Si(d,p_8)^{29}$ Si-reaction have been used to measure the channeling data from the Si-rows /34/. The anisotropic vibrational amplitudes used in the computer program were taken from X-ray diffraction results and the anisotropy of the thermal vibrations of the V-atoms was taken into account. The rms-amplitude of V-atoms in the chain parallel to <100> is 13% smaller than the amplitude perpendicular to the chain. Replacing this anisotropy by a mean isotropic value leads to results given by a dashed line in Fig. 12a,b.

It is seen that the $\psi_{1/2}$ <100>-value is not affected whereas the $\psi_{1/2}$ <110> decreased by 0.04°. This change of $\psi_{1/2}$ is only slightly above the limit of accuracy of current measurements and calculations.

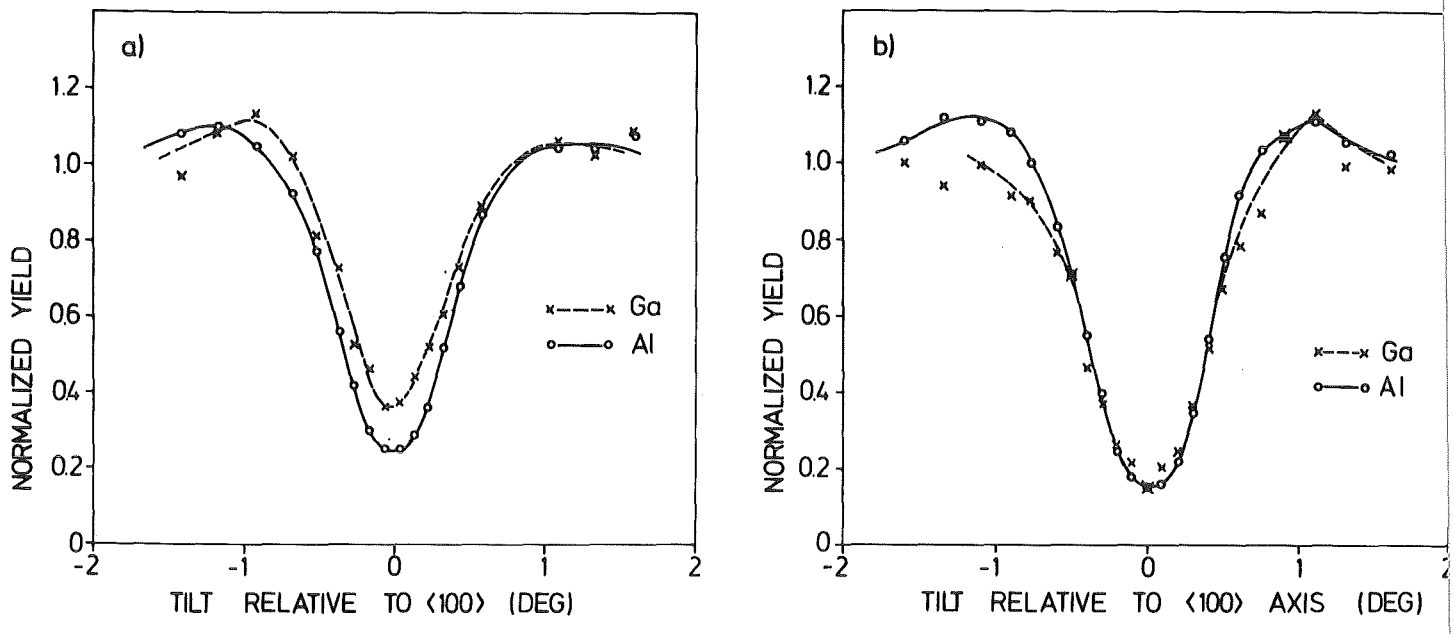

Fig. 11: Angular yield curves for Ga implanted in Al, before (a) and after annealing with a pulsed electron beam (b).

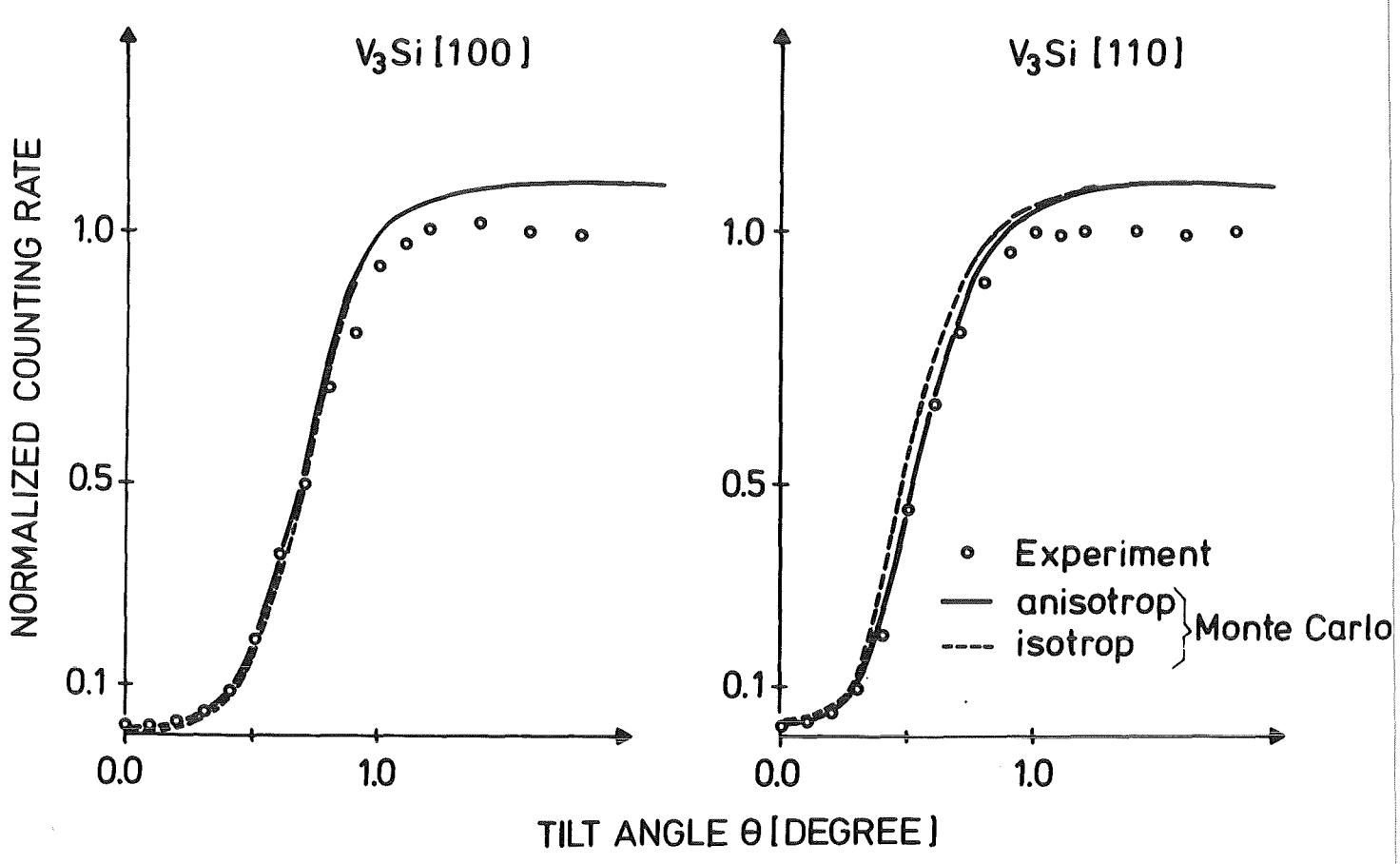

Fig. 12: Theoretical and experimental angular yield curves through the <100>- and <110>-channeling directi-ns in V_3Si. Calculations are performed using isotropic (dashed curves) and an isotropic thermal vibration amplitudes of the V-atoms.

4.3 Interstitial positions

Physical properties of metals are modified by the incorporation of light ions especially hydrogen, helium, oxygen and nitrogen. These light atoms occupy well defined interstitial positions mainly tetrahedral and octahedral sites at low temperatures and may migrate at higher temperatures. Such processes are important in many applications like hydrogen storage and reactor technology. Lattice location and diffusion processes can be monitored with the ion channeling technique. Recent review articles on this subject are found in ref. 35.

The knowledge of the flux distribution as a function of transverse energy is most important for the analysis of interstitial lattice positions. The transverse energy of the channelled particles will increase with increasing tilt angle. The flux profile will widen and the peaking will disappear. At the same time the flux and therefore the yield from foreign atoms located at interstitial positions near the rows of lattice atoms will increase. This behaviour has been calculated /36/ using the multi-row analytical method /26/ for example for 3.5 MeV ^{14}N ions incident along the <100> axial direction in Fe and is shown in Fig. 13a,b,c. Fig. 13a shows the channel bordered by 4 rows of Fe-atoms and impurity atoms located at positions O, A and B. The flux distribution along SOS' for the incident beam at angles $\psi_1 = o$, $\psi_3 = \psi_{1/2}$ and $\psi_1 < \psi_2 < \psi_3$ with respect to the <100> direction is shown in Fig. 13b. The variation of the flux at the positions O, A, B and S as function of the tilt angle is given in Fig. 13c. As the flux is proportional to the reaction yield, Fig. 13c reflects the angular yield curves that may be obtained in an experiment and which will lead to the decision about the exact location of the regular interstitial positions. For a clear-cut decision of the exact location usually further measurements along other low index crystal directions and planes are necessary. Examples for experimental results can be found in ref. 35.

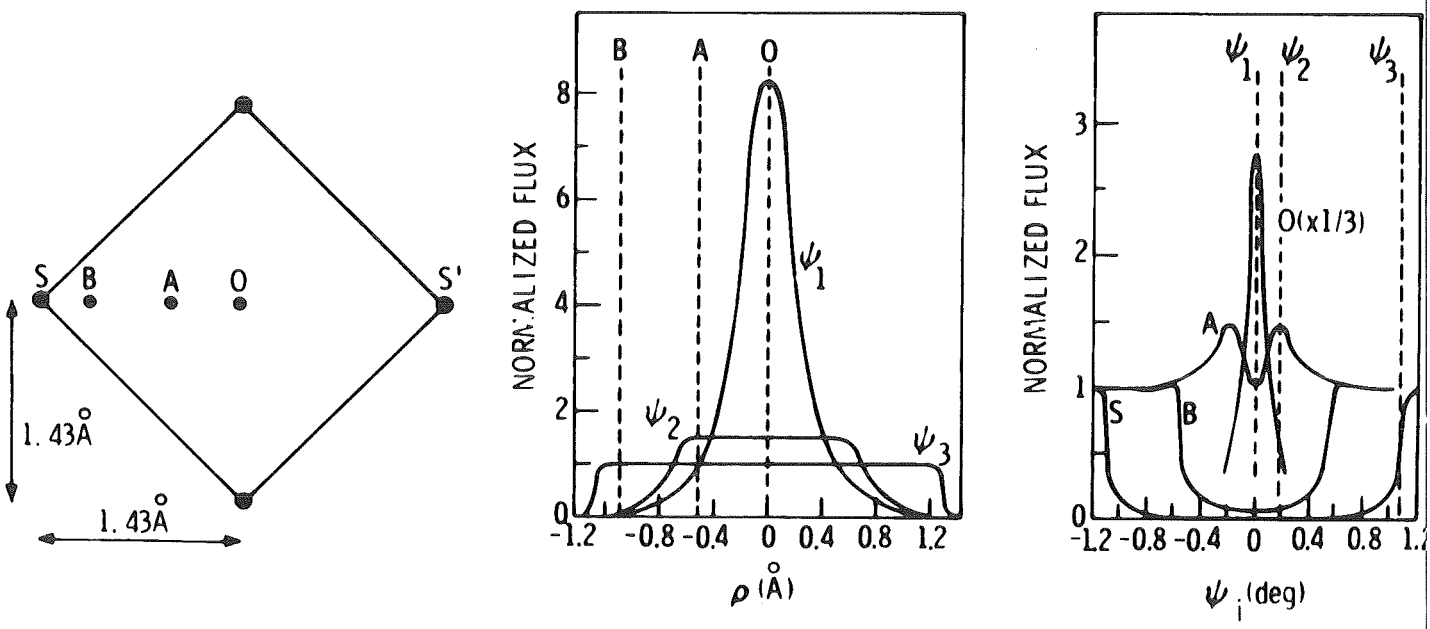

Fig. 13: Calculated spatial and angular distributions of 3.5 MeV N-ions incident along the <100> axial direction in Fe. (From ref. 30).

5. Disorder analysis

The advantage of the channeling technique for disorder analysis is, that it provides a fast and simple tool to determine the crystalline quality of the sample and to control annealing processes as has been proved in semiconductor doping by ion implantation. The disadvantage is that the method is not very sensitive, the lower limit of detection is about 1 at.% of displaced atoms of the crystal using single alignment. The analysis is ambiguous if several defect structures such as point defects, dislocation loops, clusters, stacking faults, twins etc. are present in the same sample. Other measurements, such as transmission electron microscopy should be used to determine absolute dechanneling cross sections σ_D for the various kinds of defects. Reviews on this topic may be found in ref. 4.

5.1 Amount and depth distributions of point defects

As mentioned above the incident beam along channeling directions is thought to be composed of two components, - the channelled component with the transverse energy nearly conserved and the random component, consisting of particles with impact parameters $\rho > \rho_c$, where ρ_c is the critical impact parameter leading to a deflection angle $> \psi_{1/2}$. The random component rapidly increases by increasing the angle between beam direction and axial lattice direction i.e. by increasing the transverse energy. During the motion of channeled particles inside a perfect crystal these particles will suffer multiple scattering by electrons and by thermally vibrating lattice atoms. This leads to an increase of the transverse energy and particles will be transferred from the channeled component to the random component. This effect is called dechanneling and is seen as an increase of the yield with depth in the aligned spectra. Disorder will similarly increase the transverse energy of channeling particles. This is schematically shown for displaced atoms in Fig. 14a and for a dislocation in Fig. 14b.

Large-angle deflections from displaced atoms will lead to a direct reaction yield in the backscattering analysis. Small angle scattering from displaced atoms with scattering angles larger than the critical angle for channeling will increase the dechanneling yield and will lead together with the dechanneling yield of the perfect crystal to an increase of the backscattering yield at larger depth. Locally displaced atoms are mainly observed in crystals where covalent bonding prevails, in metals mainly extended defects are present at room temperature and there is a negligible contribution to direct backscattering.

Implantation of N or of Ne into Mo provides an example for a direct backscattering component and for just an enhanced dechanneling at deeper depth /37/. By implanting N-ions in Mo the Mo-atoms are displaced from their lattice sites and an amorphous Mo structure is formed as was shown by X-ray diffraction. This amorphous layer produced a large disorder peak as can be seen in the aligned spectrum of Fig. 15. The same amount of Ne ions implanted in Mo will not stabilize displaced Mo-atoms. In this case the normal agglomeration of point defects occurs without any indication of direct backscattering. The superconducting transition temperature T_c of the disordered layer is increased from .9 to 9.2 K, after Ne implantation T_c is not affected.

5.2 Small Atomic Displacements

If the host atoms are statistically displaced from their original lattice site then, as for the determination of interstitial positions, the flux distribution F(z,y) has to be taken into account. The defect concentration $N_D(x)$ is determined by $N_D(z) = \iint N_D(x,y,z) \cdot F(z,y)dzdy$ where $N_D(x,y,z)$ is the spatial distribution of displaced atoms. The defect distribution in transverse direction perpendicular to the channel can be explored by utilizing the angular dependence of the spatial distribution of the channeled component. For such analysis it is most convenient to use a computer program and to insert into the program the depth profile as well as the lateral profile of the damage across the channel. The number and the lateral distri-

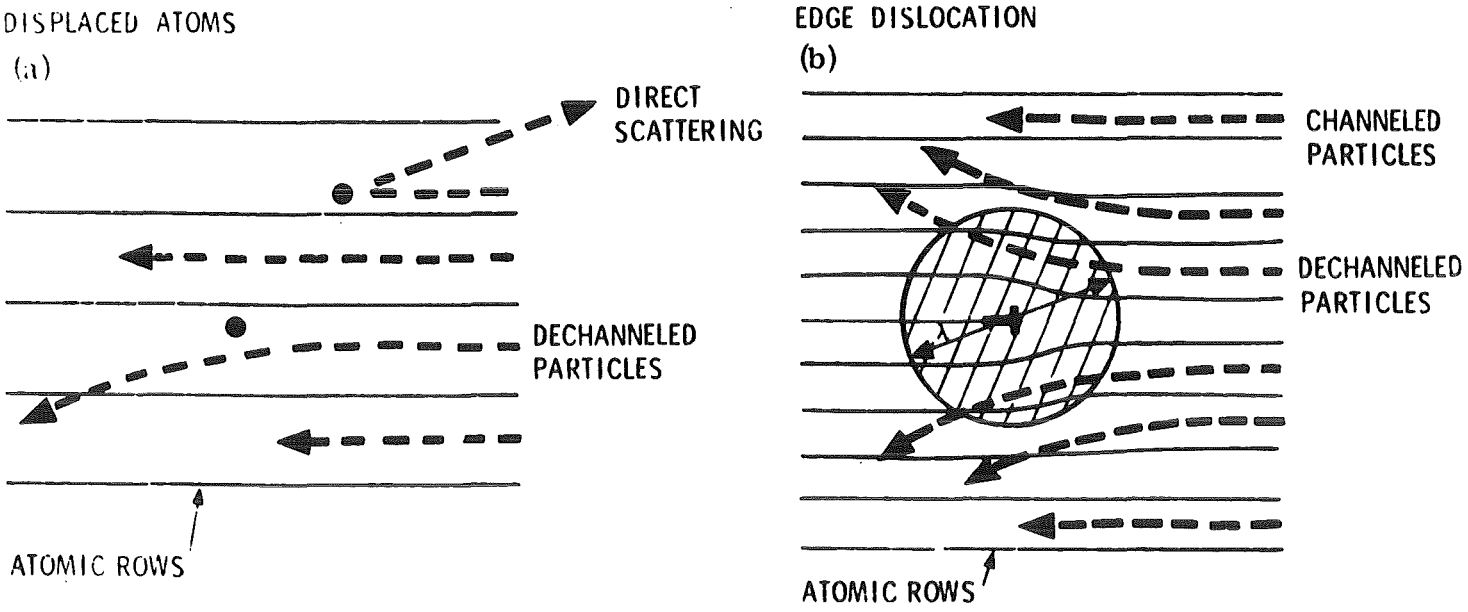

Fig. 14: Schematic representation of direct backscattering from displaced atoms (a) and dechanneling from displaced atoms (a) and from a dislocation (b).

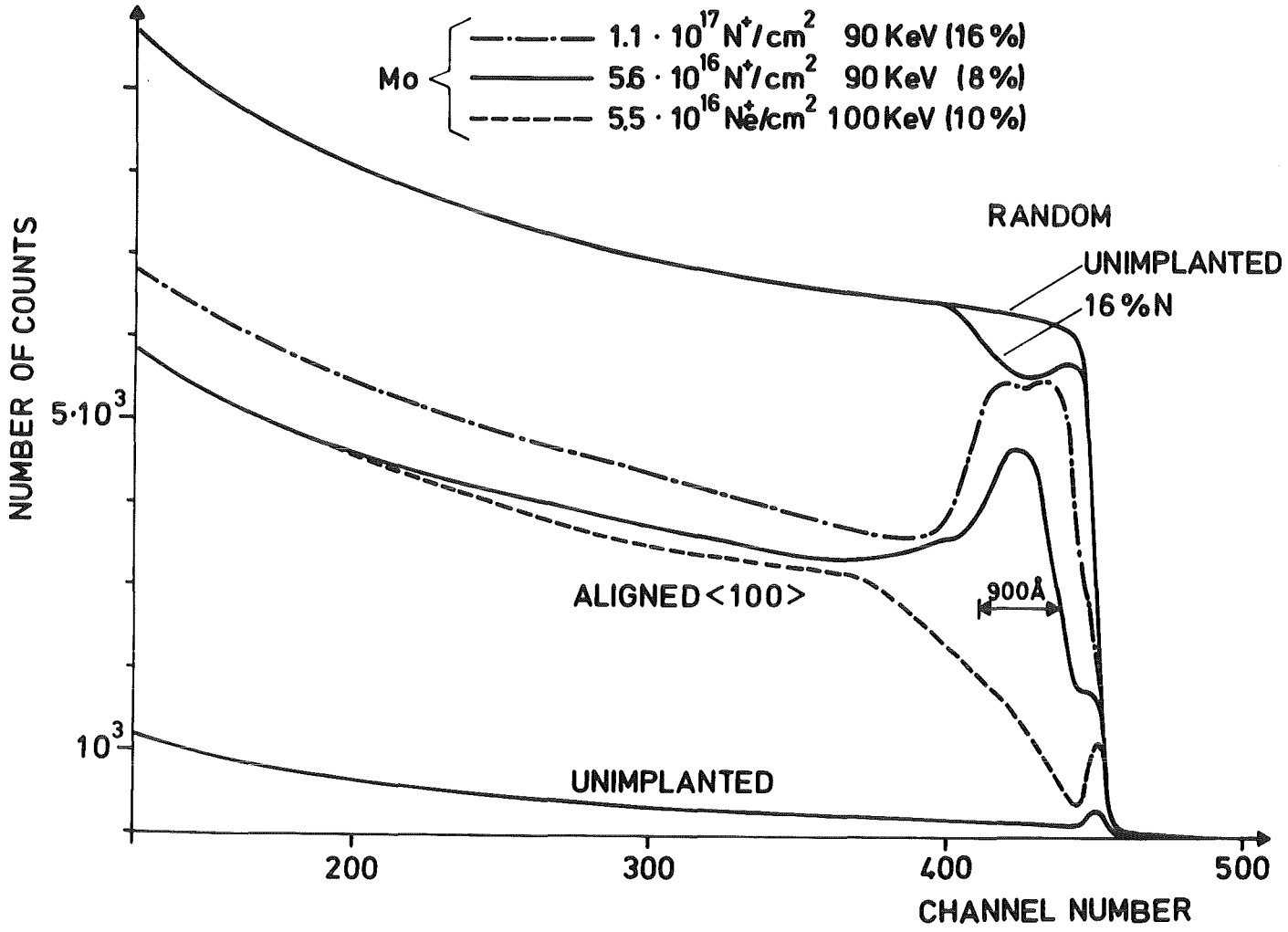

Fig. 15: Aligned backscattering spectra of 2 MeV He-ions scattered from a Mo crystal, prior to and after implantation of Ne- and N-ions.

bution of displaced atoms can be varied until the measured backscattering aligned yields in dependence of the incident beam angle can be reproduced by the calculation.

Small atomic displacements have been studied in superconductors with A15 and B1 structure as it is observed that the strong reduction of the superconducting transition temperature is correlated with the increase of disorder during preparation or irradiation. For refractory materials like NbN_x and NbC_x, T_c is found to decrease strongly with increasing amount of vacancies in the non-transition metal sublattice. The displacement fields around C-vacancies in NbC_x have been studied by measuring the temperature dependence of angular yield curves /38/. Displacement of the first Nb neighbors of $U_1 = 0.12 \pm 0.025$ Å and of the second Nb neighbors of $U_2 \leq 0.03 \pm 0.01$ Å around isolated C vacancies have been determined. These static displacements as measured with the channeling method were in good agreement with the results of X-ray diffraction experiments /39/.

High T_c superconductors with A15 crystal structure are very sensitive to radiation damage. The defect structures produced by irradiation with light and heavy ions have been intensively studied using ion channeling /40,33/. In Fig. 16 it can be seen that after irradiation of a V_3Si single crystal with 4 and $10 \cdot 10^{16}$ He-ions/cm^2 at 300 keV and at room temperature produces a direct backscattering peak at a depth of about 7000 Å where the He-ions come to rest. Near the surface up to a depth of 2000 Å only a slight increase of the minimum yield is noted. Irradiating a film of V_3Si with a thickness of 2000 Å and below with a fluence of $4 \cdot 10^{16}$ He^+/cm^2, however will reduce T_c from 16.5 to 2 K. Thus it is necessary to study in detail the damage produced in the surface near region up to 2000 Å. Angular yield curves have been measured in the energy windows as indicated in Fig. 16 and the results are shown in Fig. 17. After irradiation a narrowing of the angular yield curve is noted which can be attributed to small distortions in the order of 0.1 Å of the

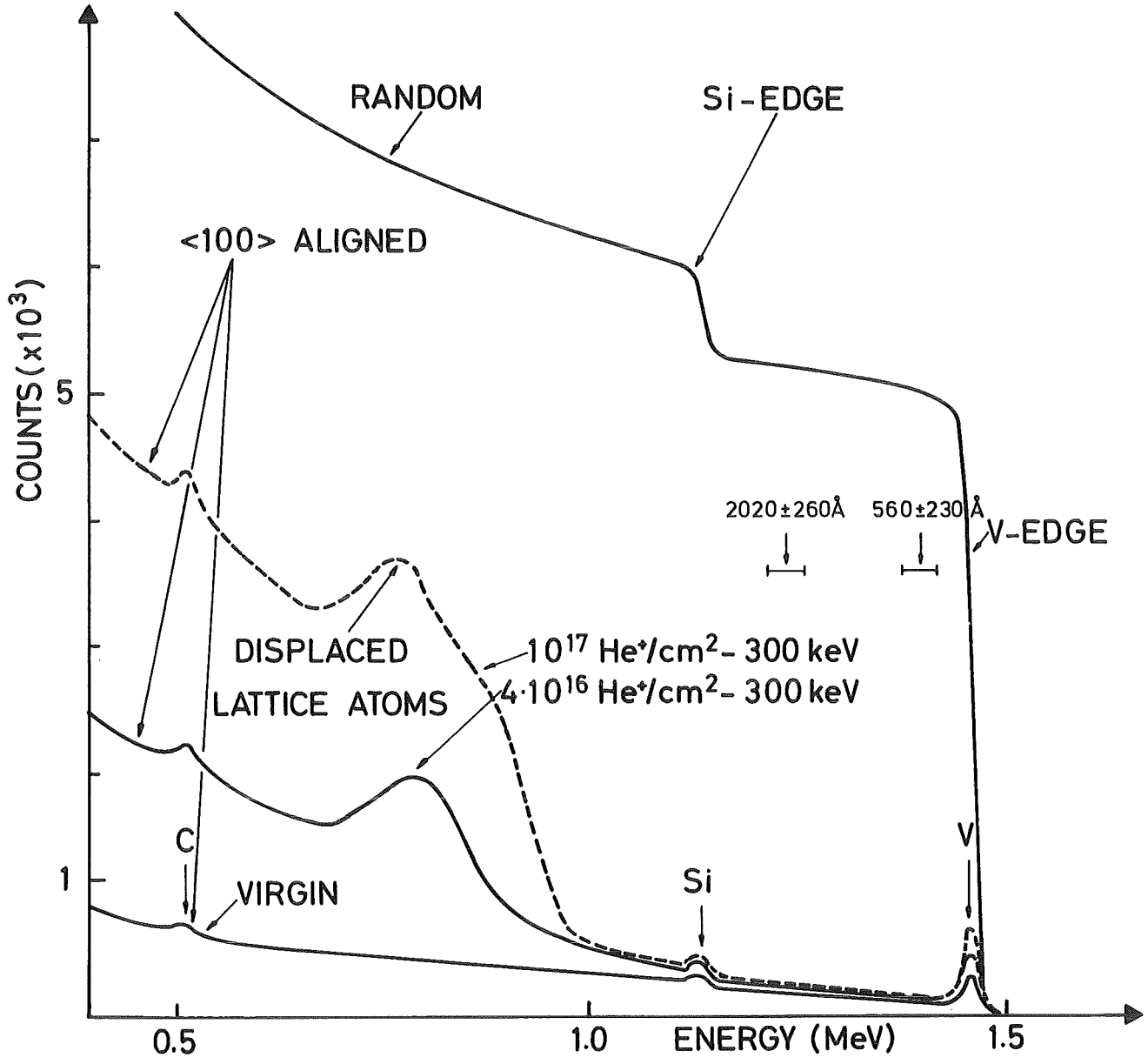

Fig. 16: Backscattering spectra for a V_3Si single crystal before and after implantation of 4 and $10 \cdot 10^{16}$ He^+/cm^2 at 300 keV.

lattice atoms. This distortions have also been measured for the Si-sublattice using a $^{29}Si(d,p_8)^{29}$ Si-reaction /41/.

5.3 Impurity defect complexes

Point defects which are produced during irradiation with energetic ions can be trapped by solute atoms. Trapping and annihilation of trapped defects as a function of the substrate temperature as well as the microscopic structure of the trapped system can be determined with in situ channeling measurements. Numerous results for many solute atoms in Al, Mg, Cu etc. have been obtained mainly by the Chalk River group /42/. One specific result for 0.13 at.% Cu in Al is shown in Fig. 18. Experimental and calculated angular yield curves are shown for backscattering of 1.5 MeV He^+-ion at 30 K. The crystal was irradiated at 70 K with $9 \cdot 10^{15}$ He^+/cm^2 at 1.5 MeV in order to form Al-Cu mixed dumbbells. The channeling analysis confirms the existence of dumbbell configurations where the Cu atoms are displaced 0.148 nm along <100> from their initial substitutional lattice positions.

6. Surface Layers and Phase Transformations

In chapter 2.2 examples have been discussed showing the usefulness of backscattering for the analysis of amorphous thin films. In the case that this thin films have been grown on a single crystalline substrate, the sensitivity of the technique will be greatly inhanced if the analyzing beam is aligned with a low index crystal direction of the substrate /14/.

Numerous examples are given where backscattering and channeling of MeV He-ions have been successfully applied to the analysis of silicon oxide /14,43c/, silicon nitride /43a,b/ and phosphosilicate glass layers on Si single crystals /43d/. Here we will give only one example for such an analysis of phosphosilicate glass (PSG) layers which are of great importance in semiconductor device technology as they show enhanced passivating properties, especially by gettering the mobile alkali ions known

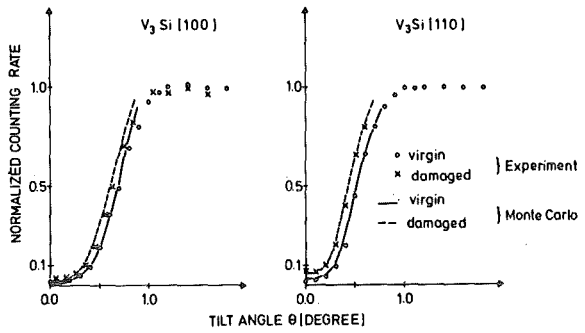

Fig. 17: Normalized angular scan curves at 500 Å below the surface through the [100] and [110]-channeling direction using 2 MeV He-ions scattered from V-atoms. Results are measured before and after irradiation with $6 \cdot 10^{16}$ He^+/cm^2 at 300 keV and are compared to calculated angular scan curves /33/.

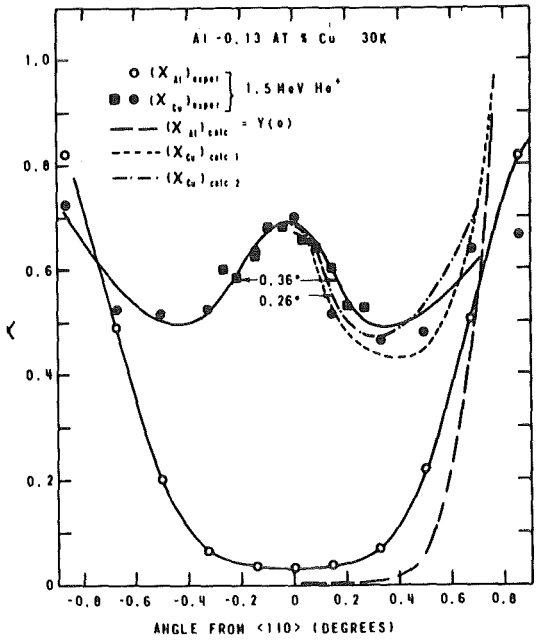

Fig. 18: Angular scan curves for an Al-crystal containing 0.13 at.% Cu after irradiation with 1.5 MeV He-ions at 70 K in order to form Al-Cu dumbbells (from Ref. 39).

to cause device instabilities. Fig. 19 clearly shows that the yield from the silicon substrate is strongly reduced by aligning the <111> crystal axis with the incident beam direction. The peak called HW_o is due to scattering from the oxygen atoms in a SiO_2-layer. The high mass resolution using 2.8 MeV He-ions allowed to seperate ^{29}Si from ^{28}Si as well as an easy seperation of P-atoms in the PSG (not shown in Fig. 18) /43d/.

Besides the analysis of thin amorphous films on single crystalline substrates information can be obtained on the process of epitaxial growth and on phase transformations of ion implanted metastable phases. During phase transformations the interface conditions between implanted and unimplanted region play an important role in the nucleation and growth process. As an example we will discuss the nucleation and growth of A15 V_3Ga from ion-implanted supersaturated Ga-V solid solutions /44/. The bcc solid solution phase field extends beyond 25 at.% Ga at high temperatures and the A15 phase forms by a congruent reaction on cooling from high to medium temperature. Implantation of Ga has been performed at room temperature to form a supersaturated alloy at room temperature. By thermal activation the alloy will then undergo a non-equilibrium transformation into the A15 high T_c phase at relatively low temperatures. In Fig. 20 random and <111>-aligned backscattering energy spectra are shown for a V single crystal implanted with 21 at.% Ga and after a heat treatment for 30 min at various temperatures as indicated. Helium ions backscattered from gallium atoms are well seperated in energy (channels 390-430) from those backscattered from vanadium atoms (channels 390 and below). From the depth scale, which is about 3.5 nm per channel, the width of the gallium profile can be estimated to be about 140 nm, in reasonable agreement with the calculated profile. The gallium concentration can be estimated from the hight of the gallium yield and the vanadium profile using eq. (11) to be about 21 at.% near the surface and about 19 at.% near the interface between implanted an unimplanted vanadium. The gallium atoms are on substitutional lattice sites and stay substitutional in the isochronal annealing process up to 775°C,

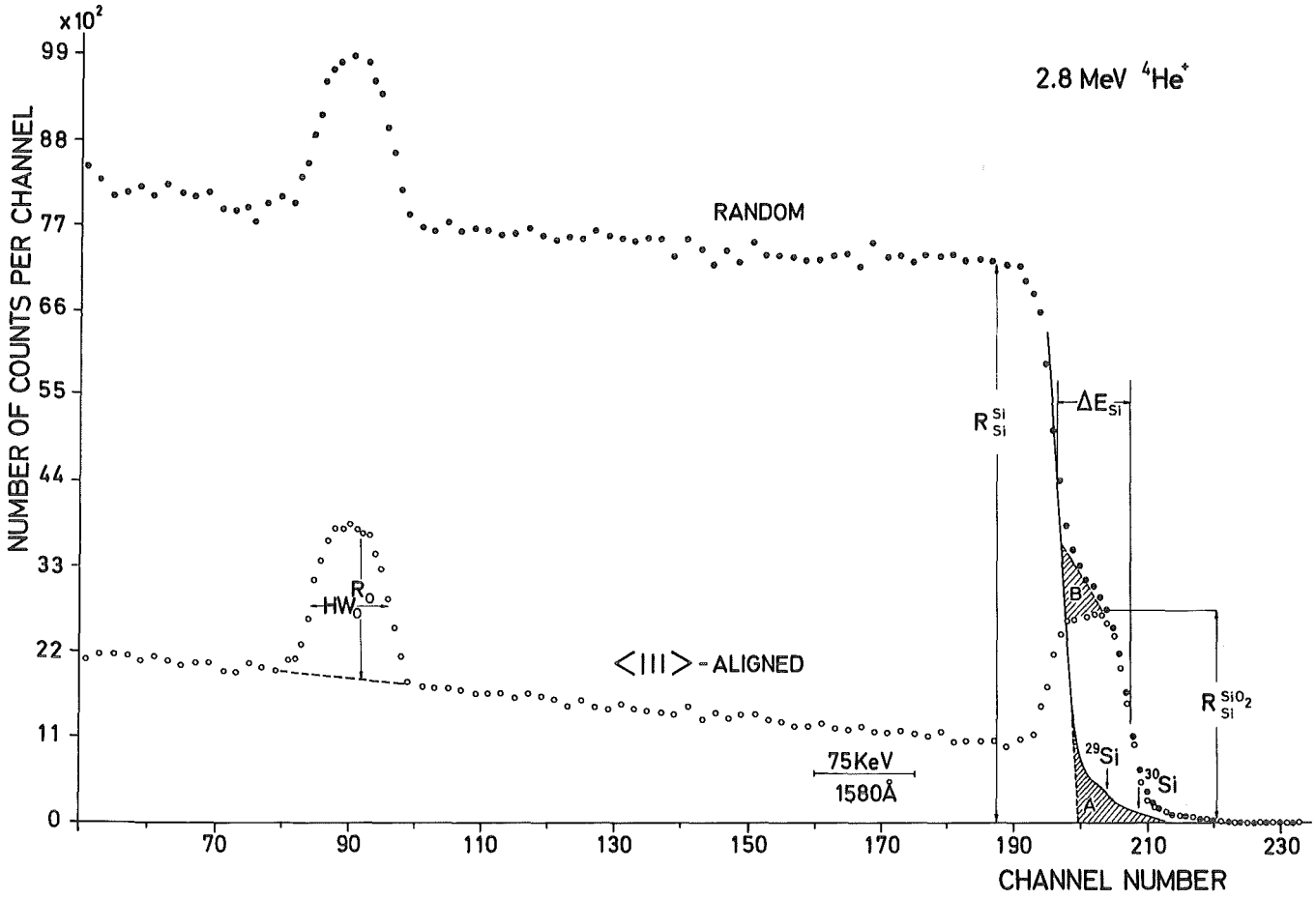

Fig. 19 Random and <111> aligned spectra of a SiO_2 layer on a single crystal Si substrate. Area B in the random spectra is due to He-ions backscattered from ^{29}Si.

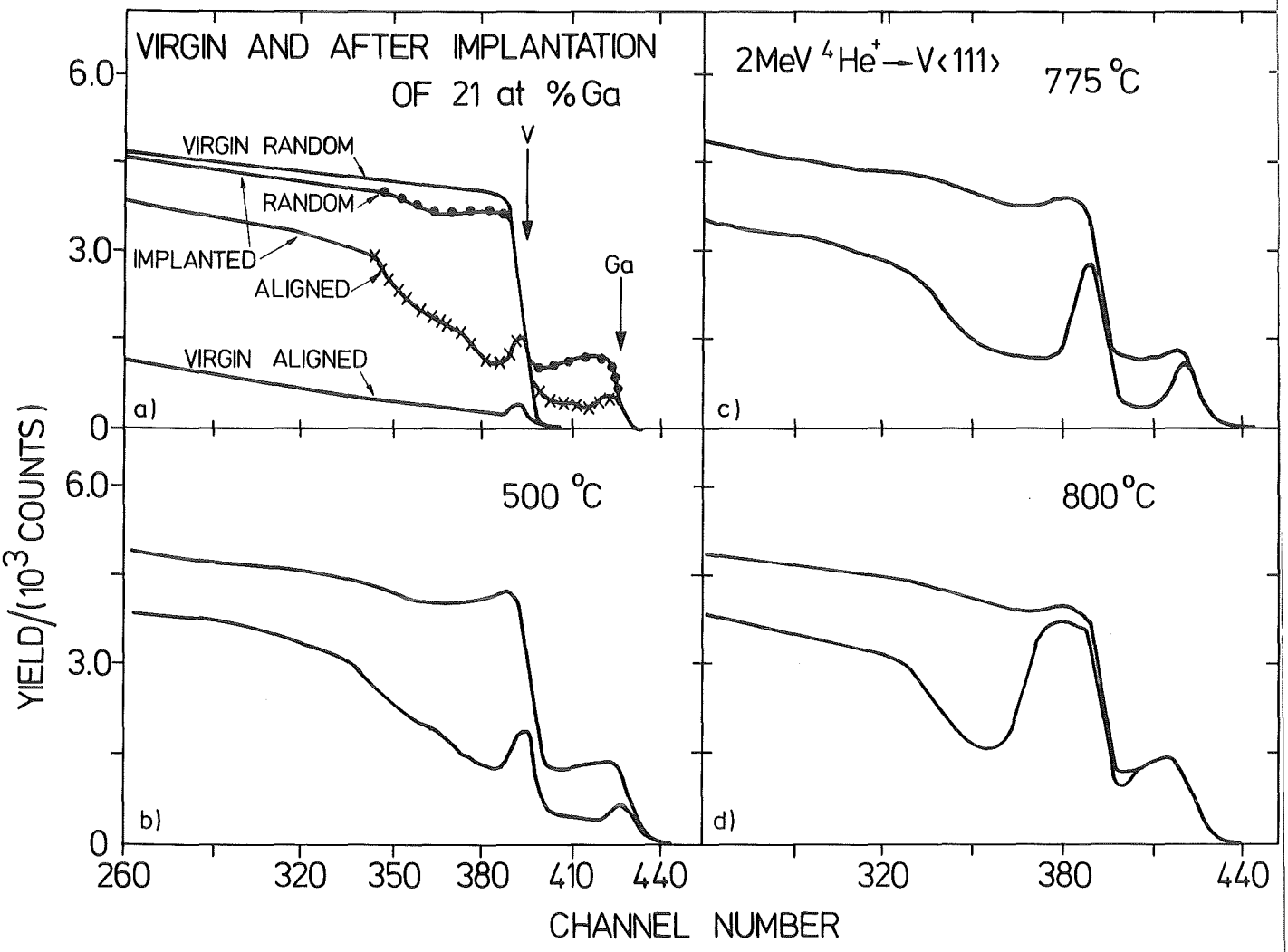

Fig. 20: Tpyical channeling and backscattering energy spectra for a homogeneous high dose (21 at.%) gallium implantation in a vanadium single crystal as a function of annealing temperature to demonstrate the nucleation and growth of the A15 phase (a) virgin crystal and after implantation; (b) 500°C; (c) 775°C; (d) 800°C.

where the transformation into the A15 phase starts at the surface. The growth is almost complete at 800°C. Thin film X-ray measurements and inductive T_c measurements clearly prove that the A2 phase has transformed to A15. Further results on the interface behaviour especially at higher Ga concentrations may be obtained in ref. 44.

7. Surface Studies

In the last years ion channeling became an important tool to provide informations on clean and covered single crystal surfaces. Relaxation and reconstruction phenomena have been studied and quantitative values for the coverage and the position of adsorbate atoms have been obtained. A recent review on that topic is given in ref. 7.

Applications of basic interest are the determination of surface relaxations Δd of the outermost layers on a single crystal and the dependence of this relaxation amplitude on temperature and on the adsorption of foreign atoms. Of further interest are the location of adsorbed atoms and the reconstruction of the outermost layer of host atoms as a function of temperature and adsorption. Such studies have been performed using experimental arrangements as shown in Fig. 1 /39/, the combined use of channeling and blocking /40/ where the crystal is well aligned with the incident beam and the detector is tilted through a blocking axis, and by surface channeling /40/, where the beam enters the single crystal surface at angles smaller than the critical angle for axial channeling. The aligned backscattering spectrum as for example in Fig. 15 for the unimplanted Mo single crystal always shows a clearly resolved surface peak which provides a quantitative measure of the number of unshadowed lattice atoms per cm^2. The surface peak may include surface atoms which are oxidized and therefore be displaced from their lattice sites. Thus it is essential that the surface is cleaned in situ in the UHV chamber.

Fig. 21 illustrates how the surface peak area will change if the surface structure varies as indicated. For a clean unreconstructed surface having a 1 x 1 LEED pattern the surface peak area is direct proportional to the number of atoms in the first layer. For He-ion beam energies below 1 MeV the atom of the second layer are completely shadowed by the atoms of the first layer (Fig. 21a). If a surface reconstruction does occur (Fig. 21b) then the peak area will increase as the atoms in the second layer are no longer shadowed by those of the first layer. For the case of a relaxation of the first layer the channeling experiment has to be performed through two different low index crystal directions. The surface peak area will increase if the atoms are no longer perfectly aligned under a certain crystal directions (Fig. 21c). A surface covered with adsorbate atoms may have a reduced surface peak area if the adsorbate atoms are sitting on top of the surface atoms as shown in Fig. 21d. As discussed in chapter 1.2 the sensitivity of ion scattering to atomic mass permits a discrimination between substrate an adsorbate. The channeling processes can be simulated by Monte Carlo calculations using the surface crystal structure as a model parameter. Some ambiguity of the calculated data is due to the fact that for the vibrational amplitude of surface atoms, bulk values of the Debye temperature are used and isotropic vibrations are assumed. Both assumptions are probably not correct for atoms close to or at the surface. Temperature dependent measurements under different crystal directions may be useful to solve such problems.

Although it is by no means possible to treat the subject in any detail in such a short review the reader may have gained some impression on the potentials of the ion beam techiques for materials analysis.

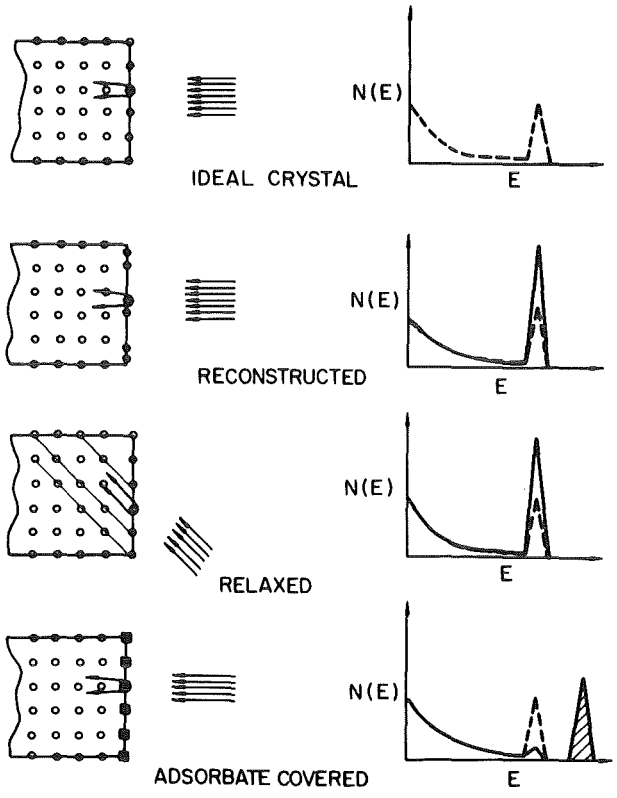

Fig. 21: Influence of different surface structures on the yield of the surface peak in the aligned backscattering spectra /7/.

References

/1/ J.F. Ziegler, New Uses of Ion Accelerators, Plenum Press, New York (1975)

/2/ J.W. Mayer, J.F. Ziegler (eds.), Ion Beam Surface Layer Analysis, Thin Solid Films, Vol 19 (1973)

/3/ O. Meyer, G. Linker, G. Käppeler (eds.), Ion Beam Surface Layer Analysis, 2 vols, Plenum Press, New York (1976).

/4/ W.-K. Chu, J.W. Mayer, M.-A. Nicolet Backscattering Spectrometry, Academic Press, New York (1978)

/5/ D.V. Morgan (ed.), Channeling, Wiley, New York (1973)

/6/ D.S. Gemmell, Rev. Mod. Phys. 46, 129 (1974)

/7/ L.C. Feldman, J.W. Mayer, S.T. Picraux, Materials Analysis by Ion Channeling, Academic Press, New York (1982)

/8/ S. Rubin, Nucl. Instr. and Meth. 5, 177 (1959)

/9/ A.L. Turkevich, Science 134 (1961) 672 and J. Geophys. Res. 70 (1965) 1311

/10/ S. Petersson, P.A. Tove, O. Meyer, B. Sundqvist and A. Johansson in Ref. 2, p. 157

/11/ J.W. Mayer and E. Rimini (eds.), Ion Beam Handbook for Materials Analysis, Academic Press, New York (1977)

/12/ G. Linker, O. Meyer and M. Gettings in Ref. 2, p. 177

/13/ O. Meyer, H. Mann and G. Linker, Appl. Phys. Lett. 20 (1972) 259

/14/ O. Meyer, J. Gyulai and J.W. Mayer, Surface Science 22 (1970) 263

/15/ W.H. Bragg and R. Kleeman, Phil. Mag. 10 (1905) 318

/16/ O. Meyer, G. Linker and B. Kraeft in Ref. 2, p. 217

/17/ A. ul Haq and O. Meyer, J. Low Temp. Phys. 50 (1983) 123

/18/ R.F. Sippel, Phys. Rev. 115 (1959) 1441

/19/ O. Meyer and J.W. Mayer, J. Appl. Phys 41 (1970) 4166

/20/ H. Mann, G. Linker and O. Meyer, Solid State Commun. 11 (1972) 475

/21/ M.T. Robinson and O.S. Øen in the Proceedings of the Conf. "Le Bombardement Ionique ed. I. I. Trillat, C.N.R.S., Paris (1961)

/22/ G.R. Piercy, F. Brown, J.A. Davies and M. McCargo, Phys. Rev. Lett. 10 (1963) 399

/23/ H. Lutz and R. Sizmann, Phys. Lett. 5 (1963) 113

/24/ R.S. Nelson and M.W. Thompson, Phil. Magn. 8 (1963) 1677

/25/ Channeling-Theory, Observation and Applications, ed. D.V. Morgan (Wiley and Sons, London 1973)

/26/ D.S. Gemmell, Rev. Mod. Phys. 14 (1974) 129

/27/ J. Lindhard, Phys. Lett. 12 (1964) 126

/28/ T. Hussain, J. Geerk, F. Ratzel and G. Linker, Appl. Phys. Lett. 37 (1980) 298 and Solid State Commun. 44 (1982) 745

/29/ J.H. Barret, Phys. Rev. B3 (1971) 1527

/30/ H.D. Carstanjen and R. Sizmann, Rad. Effects 12 (1972) 225

/31/ Chr. Lehmann and G. Leibfried, Z. Phys. 172 (1963) 465

/32/ G. Molière, Z. Naturforschung 2A (1947) 142

/33/ R. Kaufmann and O. Meyer, Rad. Effects 40 (1979) 97 and 161

/34/ O. Meyer, R. Kaufmann, B.R. Appleton and Y.K. Chang Solid State Commun. 39 (1981) 825

/35/ H.-D. Carstanjen, phys. stat. sol. (a) 69 (1980) 11

/36/ R.B. Alexander, P.T. Collaghan, and J.M. Poate, Phys. Rev. B9 (1974) 3022

/37/ G. Linker and O. Meyer, Solid State Commun. 20 (1976) 695

/38/ R. Kaufmann and O. Meyer, Phys. Rev. B28 (1983) 6216

/39/ T.H. Metzger, J. Peisl and R. Kaufmann, J. Phys. F 13 (1983) 1103

/40/ O. Meyer and B. Seeber, Solid State Commun. 22 (1977) 603

/41/ O. Meyer, J. Nucl. Mat. 72 (1978) 182

/41/ O. Meyer, R. Kaufmann, B.R. Appleton and Y.K. Chang Solid State Commun. 39 (1981) 825

/42/ L.M. Howe and J.A. Davies in Site Characterization and Aggregation of Implanted Atoms in Materials, Ed. A. Perez and R. Coussement (Plenum Press, N. Y. 1980)

/43/ a. O. Meyer and W. Scherber, J. Phys. Chem. Solids 32 (1971) 1909

b. J. Gyulai, O. Meyer and J.W. Mayer, J. Appl. Phys. 42 (1971) 451

c. S. Petersson, G. Linker and O. Meyer, phys. stat. sol. (a) 14 (1972) 605

d. G. Linker, O. Meyer and W. Scherber, phys. stat. sol. (a) 16 (1973) 377

/44/ J.M. Lombaard, G. Linker and O. Meyer,
J. of the Less-Common Metals 96 (1974) 191

/45/ J.A. Davies in Material Characterization using Ion Beams ed. J.P. Thomas and A. Cachard (Plenum Press, N. Y. 1978)

/46/ W.C. Turkenburg, W. Soszka, F.W. Saris, H.H. Kersten and B.G. Colenbrander, Nucl. Instr. Meth. 132 (1976) 587

/47/ R. Sizmann and C. Varelas, Nucl. Instr. Meth. 132 (1976) 633
C. Varelas, H.D. Carstanjen and R. Sizmann, Phys. Lett. 77A, 469

II. MATERIALS MODIFICATION BY ION IRRADIATION AND IMPLANTATION

Contents

GENERAL INTRODUCTION

Ion implantation is a process by which nearly all elements can be introduced into near surface regions of materials without any metallurgical constraints. The concentration and the depth distribution can be well controlled, leading to a high degree of reproducibility in altering chemical and physical properties of the materials.

The process of implantation can be divided into different steps which will be considered separately in the following:

1. Sticking factor and sputtering: If a beam of ions with energies between typically 10 and 500 keV will hit the surface of a target, some ions may not penetrate into the target but will be reflected by large angle collisions with the host atoms in the outermost layers thus leading to a sticking factor below one. In such head on collisions the host atom may receive a high recoil energy in forward direction. The momentum may be reversed in further collisions leading to an ejection of a host atom. This process will be called sputtering.
2. Energy loss process: In the slowing down process the ion will interact with many target atoms. The problem can be treated as a series of binary collisions. The collisions depend on the interatomic potential V(r) which will determine the trajectories of both colliding particles. The knowledge of the interaction potential is of fundamental importance. The amount of energy lost in each collision until the incident ion comes to rest will determine the total path length i.e. the range of the particle. To a good approximation the energy loss process can be considered either to occur by inelastic collisions with the target electrons (excitation of atomic electrons) or by elastic collisions with the target atoms where the kinetic energy is conserved. The interaction in the second process may be described by a partially screened Coulomb potential as interatomic potential.

3. Range and range distribution: The sequence of elastic and inelastic collisions is a stochastic process. Thus the range and range distribution will be given by a probability distribution. In agreement with the experiment the distribution will be Gaussian-shaped as long as an amorphous target is used. In single crystals the depth distribution may be strongly distorted by the channeling effect. If the ions enter a single crystal nearly parallel to a low index crystal direction under an angle smaller than the so-called critical angle than they are steered by a series of small angle collisions to a depth which is significantly larger than the mean penetration depth in an amorphous target. Other penetration anomalies such as enhanced diffusion due to the mobility of point defects at elevated implantation temperatures have been noted and will be discussed later.
4. Radiation damage: During the slowing down process of the incident energetic ion, energy is transferred to the target atoms by elastic collisions. The average energy to displace a target atom, called the displacement energy, is typically 25 eV. Thus it is obvious that heavy ions having energies in the keV region cause considerable damage. The recoiled host atom may itself displace further host atoms and produce cascades of displaced atoms. Under certain conditions, if almost all atoms in a small region are displaced the concept of a sharp displacement energy breaks down resulting in a nonlinear cascade or "spike process".
5. Annealing: A large amount of displaced atoms will return to regular lattice sites in annealing processes. Annealing may occur over a short time scale already during the implantation process. Important features are the temperature dependent mobilities of point defects and the nucleation and growth processes which depend on the temperature as well as on chemical binding energies. Annealing can also be applied as a seperate thermally activated process following the implantation. Radiation damage itself may

influence the chemical and physical properties of the implanted region and may mask the doping effects of the implanted foreign ions. The knowledge of the mechanisms of damage production and annealing is therefore of great importance.

6. Lattice site location and compound formation: The lattice location of the implanted ion directly after the slowing down process or after annealing will determine the chemical and physical properties of the sample. Ion implantation is a non-equilibrium process and it is expected that metastable alloys can be produced, which do not exist in the equilibrium phase diagram. From the replacement collision theory it can be inferred that the implanted ion should have a high probability to get trapped on a regular lattice sites. Beside the formation of supersaturated interstitial and substitutional solid solutions other effects have been observed such as amorphization and compound formation.

The whole field is well documented in the literature. Basic ion-atom collision processes are described in references /1 to 3/. Applications to semiconductor doping and their electrical properties are treated in references /4 to 6/. Applications to metals and insulators are treated in a recent book /7/ and in the proceedings of the conferences on Ion Beam Modification of Materials /8 to 11/.

In the following review a short description of the basic processes of ion target interactions will be presented in chapter 1. In chapter 2 some applications in materials science will be discussed emphasizing the various advantages of ion implantation as a non-equilibrium technique. A few of our experimental results are presented to demonstrate the unique features of ion beam modification by irradiation and implantation.

1. Basic Processes

Ion ranges, range distributions and disorder profiles will be governed by the collisions of atoms in the slowing down process. The slowing down process is considered as a sequence of binary collisions where each collision consists of two colliding point masses in a central force field. In such a conservative system the total energy is conserved and there is only an exchange between kinetic and potential energy. The collision is then called elastic. In this description the electronic structure of the colliding atoms and the excitations of the electrons are completely ignored. Clearly, such inelastic excitation processes will occur in each collision and will slightly influence the trajectories and the kinetic energies of the colliding atoms. In praxis however it turns out that to a good approximation the correlation between elastic and inelastic processes can be neglected and both processes can be treated separately.

1.1 Atomic Collisions and Energy Loss

When a charged particle penetrates a thin film of thickness Δx the amount of energy loss (ΔE) of the projectile with energy E to the target is defined as

$$dE/dx(E) = \lim_{x \to 0} \Delta E/\Delta x$$

The thickness of the film may be described by the number of atoms per unit area, $N \cdot \Delta x$, thus the atomic stopping cross section (S) can be expressed by $dE/(N \cdot dx)$ in $eV \cdot cm^2$. Considering the slowing down process as a series of binary collisions S can be described by

$$S = \sum_i T_i P_i = \int_{T_{min}}^{T_{max}} T d\sigma \qquad (1)$$

T_i is the kinetic energy transferred to the i-th target atom in elastic nuclear collisions ($S \equiv S_n$) or to the i-th electron in inelastic electronic collisions ($S \equiv S_e$) with a probability P_i for an energy transfer between T and T+dT. The integral extends over all possible energy losses in individual collisions and $d\sigma$ is the cross section for the energy transfer. The total energy loss is then given by $S = S_n + S_e$ and the range of the projectile is obtained as

$$R(E) = \int_0^{E_o} dE/(S \cdot N) \qquad (2)$$

In order to evaluate eqs. (1) and (2) the basic collision processes will shortly be discussed.

a) Elastic collisions: the motion of two point masses in a central force field is a straightforward exercise of classical mechanics applied to describe the planetary motion. The general solution of the equations of motion is the wellknown scattering integral which provides the connection between the angle of deflection ϕ in the center of mass system and the impact parameter p:

$$\phi = \pi - 2p \int_{\infty}^{r_{min}} dr/(r^2 \cdot \{1 - V(r)/E_R - p^2/r^2\}^{1/2}) \qquad (3)$$

r is the distance of separation between the masses M_1 and M_2, r_{min} is the minimum distance of approach, E_R is the relative energy of collision, $E_R = M_2 \cdot E_o / M_1 + M_2$, and V(r) is the interatomic potential. Since the system is conservative, the energy transfer for a given scattering angle ϕ is independent on the form of the interaction potential. Thus the final asymptotic values of velocities and energies can be calculated by just considering energy and momentum conservation in the center of mass system. The energy transferred to a target atom is $T = E_o - E_1$ with E_o and E_1 being the energies of the incident particle before and after collision, respectively, is then given by

$$T = E_o \cdot \{ \frac{4M_1M_2}{(M_1+M_2)^2} \sin^2\phi/2 \} \qquad (4)$$

The maximum transferred energy in a head on collision is

$$T_M = \frac{4M_1M_2}{M_1+M_2} E_o$$

The differential scattering cross section $d\sigma$ for the scattering processes with impact parameters between p and p + dp and scattering angles ϕ and $\phi + d\phi$ is given by

$$d\sigma = 2\pi p\, dp \quad \text{and} \quad d\sigma/d\Omega = pdp/(\sin\phi d\phi) \qquad (5)$$

Equation (3) provides the dependence between ϕ and p. Thus, in order to calculate energy transfers and differential cross-sections for a given energy transfer, eq. (3) has to be solved completely. This can be done numerically for all potentials, analytically however only for interaction potentials with $V(r) = C/r^s$. These inverse power potentials represent the Coulomb potential for s = 1, the Nilson potential for s = 2 and the hard core potential for s = 0.

A detailed evaluation of the differential cross section $d\sigma = 2\pi p\, dp$ for energy transfer provides the important result that $d\sigma$ increases with decreasing T for s = 1 and 2. From eq. (2) T decreases with decreasing ϕ thus the scattering is large in forward direction. For the hard sphere case s = 0 $d\sigma$ is independent of T and thus from eqs. (2) and (1) independent of ϕ and p with the result that all energy transfers

from 0 to T_m and all scattering angles are equally probable, the scattering is isotropic. The total collision cross section σ_{tot} is infinit for real potentials $\sigma_{tot} = \int_{p=0}^{p=\infty} d\sigma$ and finite for the hard sphere case (from p = 0 to p = r_{min}). The case s = 1 was first treated by Rutherford and resulted in the famous Rutherford differential scattering law for α-particles penetrating thin films. The differential cross section can conveniently evaluated in the so-called momentum approximation when p is large or E_o is large and ϕ is small and in the hard sphere approximation for nearly head-on collisions where p is small and the deflection angle is large. Lindhard /12/ has provided the inverse power potential as a good approximation to the scattering integral for all values of s. Besides the power law potential, screened potentials are used,especially the Thomas-Fermi-Potential

$$V(r/a) = (a/r) \frac{Z_1 Z_2 e^2}{r} \phi(r/a) \qquad (6)$$

where the Thomas-Fermi screening radius is given by

$$a = a_o \cdot 0.8853 \, (Z_1^{2/3} + Z_2^{2/3})^{-1/2} \qquad (7)$$

Universal curves are obtained for both the stopping power and the range energy relation by introducing dimensionless parameters ρ and ε for the range and energy, respectively

$$\rho = RN \, 4 \cdot \pi a^2 \frac{M_1 M_2}{(M_1+M_2)^2} \qquad (8a)$$

$$\varepsilon = E \frac{a \cdot M_2}{Z_1 Z_2 e^2 (M_1+M_2)^2} \qquad (8b)$$

With these parameters the differential scattering cross section can be given by a one-parameter equation

$$d\sigma = \pi a^2 \, f(t^{1/2}) \cdot dt/(2 \cdot t^{3/2}) \qquad (9)$$

where $t = \varepsilon^2 \sin^2\phi/2$. Evaluation of eq. (1) lead to an universal expression for S_n

$$S_n = -4\pi a^2 \frac{M_1}{M_1+M_2} \frac{Z_1 Z_2 e^2}{a} \left(\frac{d\varepsilon}{d\rho}\right)_n \qquad (10a)$$

where $$\left(\frac{d\varepsilon}{d\rho}\right)_n = \frac{\ell n \varepsilon}{2\varepsilon(1-\varepsilon^{-3/2})} \qquad (10b)$$

The universal curve for S_n is shown in Fig. 1 /13/ revealing a maximum for $\varepsilon \leq 1$.

b) Inelastic collisions. The treatment of electronic stopping is more complex. For the high energy region S_e reveals a maximum for a projectile velocity $v_1 = Z_1^{2/3} v_o$ with Bohr's velocity $v_o = e^2/h$ (see Fig. 1). For velocities larger than v_1, S_e decreases with 1/E. In this energy region which is called the Bethe-Bloch region, direct energy transfer is provided to single electrons. S_e is given by

$$S_e = \frac{4\pi Z_1^2 Z_2 e^4}{m_e v^2} \left[\log \frac{2 m_e v^2}{I} + \ldots \right] \qquad (11)$$

This energy region is important for the materials analysis with light ions in the MeV region. In the low energy region, which is important for slow moving heavy ion as in the case of ion implantation it is seen in Fig. 1 that no longer a universal curve exists for S_e. S_e is seen to increase linearly with $\varepsilon^{1/2}$ and the proportionality factor k is 0.14 ± 0.03 as long as $Z_1 \gtrsim Z_2$. In this low energy region all electrons are excited collectively and the plasma frequency ω_p of the host lattice electrons becomes important. Firsov /14/ considered a simple geometrical model of momentum exchange between projectile and target atom during interpenetration of

electron clouds. Here we will simply present the often used proportionality factor k as given by Lindhard /12/

$$k = \frac{0.0793\ Z_1^{2/3} Z_2^{2/3} (M_1+M_2)^{3/2}}{Z^{1/2} M_1^{3/2} M_2^{1/2}} \qquad (12)$$

1.1.2 Range and Range Distribution

The reduced range $\rho(\varepsilon)$ can now be determined by evaluating eq. (2) in reduced parameters ρ and ε. This equation gives the average total path length for an ion slowing down from an energy E_o as the total path is composed of many small pieces in different directions caused by large angle deflections. The total average path length projected on the original direction of the incident ion is defined as the projected range R_p. Clearly, for individual projectiles the number of collisions, the energy transferred and thus the total path length will vary and the variation can be described by a Gaussian distribution curve to express the distribution curve of implanted ions, N(x)

$$N(x) = N_p \exp -0.5 \left\{\frac{x-R_p}{\Delta R_p}\right\}^2 \qquad (13)$$

The peak concentration is $N_p = N_s/(\sqrt{2\pi} \cdot \Delta R_p) \cong 0.4 N_s/\Delta R_p$ where N_s is the number of implanted ions/m^2, and ΔR_p is the standard deviation. At $x = R_p \pm \Delta R_p$ $N(x) = N_p/\sqrt{e}$.

Values for the average projected range R_p and the average standard deviation of the projected range ΔR_p are presented in tabulator or graphical form /15,16,17,18/ mostly based on the LSS-theory /19/.

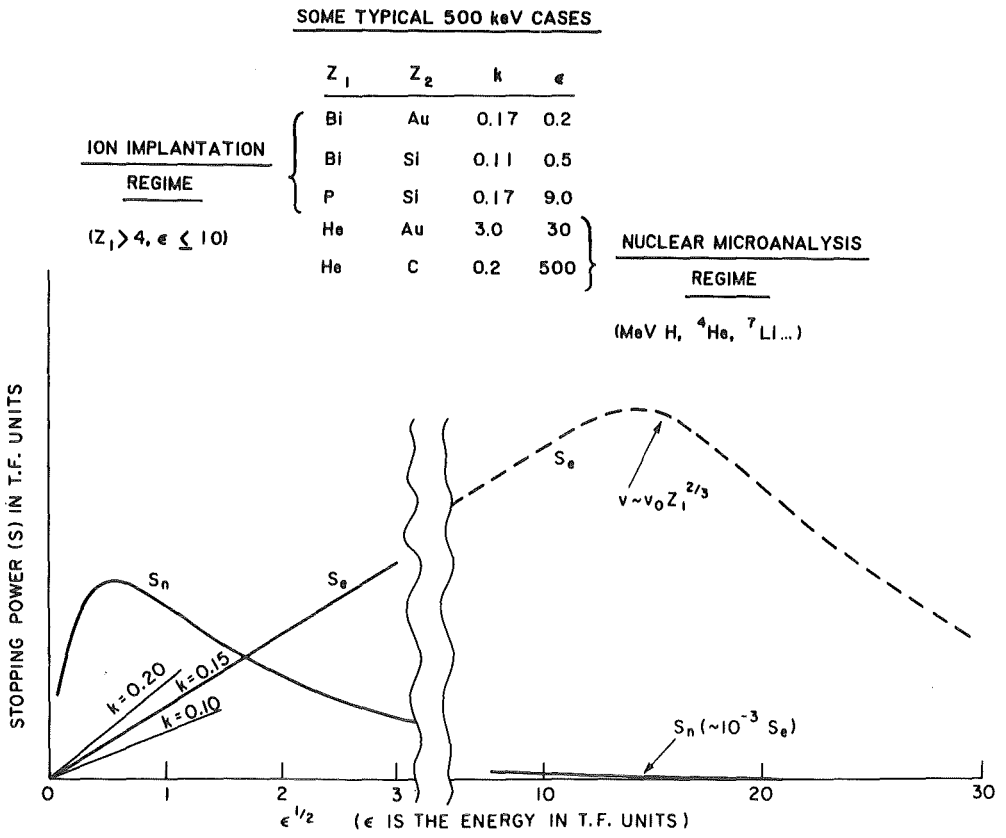

Fig. 1 Energy dependence of the nuclear (S_n) and electronic (S_e) stopping powers in dimensionless units /13,19/.

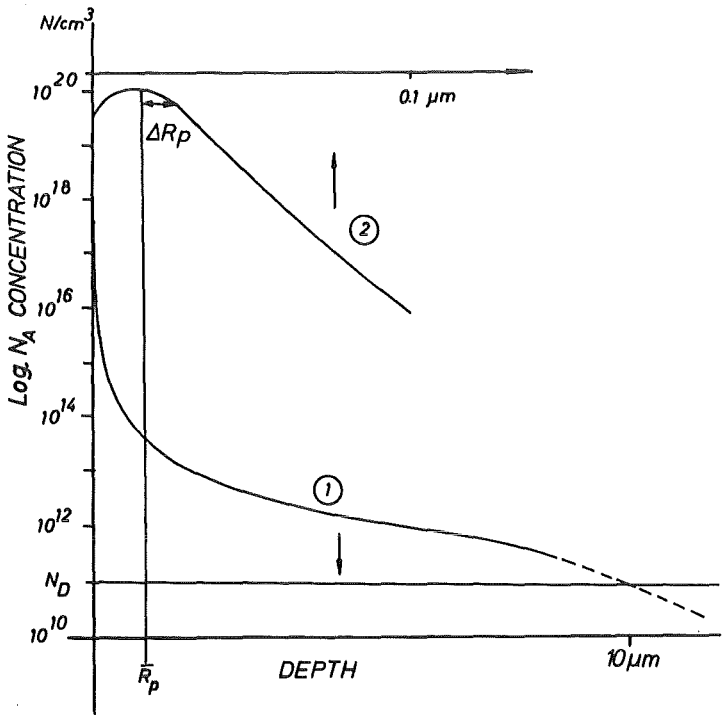

Fig. 2 Schematic concentration distribution of electrically active centers in a boron-implanted p-n junction.

a) Measurements techniques: Methods for the determination of implanted ion density profiles may be divided in destructive and non-destructive techniques. In the first group, layers of well-known thicknesses are removed by anodic stripping, vibratory polishing or sputtering. The implanted ions are detected by their electrical activity, if they are dopants in semiconductors, by radiotracer methods for radioactive ion species or by secondary ion mass spectroscopy (SIMS) during sputtering. Non-destructive techniques are the Rutherford-Backscattering Spectroscopy (RBS) of light ions in the MeV region, the capacitance-voltage method and the window thickness-voltage method for implanted p-n junctions in semiconductors.

b) Comparison with experiment: The radiotracer techniques provide the most sensitive detection methods. Using various radiotracer ions implanted in amorphous Ta_2O_5 /21/ excellent agreement with range values as predicted by the LSS-theory was obtained. In general it was observed that for amorphous targets the agreement between calculated and measured R_p- and ΔR_p-values for all ion-target atom combinations are in the order of 20% in the energy range between 10 and 300 keV.

c) Penetration anomalies: For crystalline target the influence of the channeling effect on the range profile can hardly be avoided. If the angle of incidence between the direction of a heavy ion beam and low index crystal direction is smaller than a critical value ψ_c

$$\psi_c \cong \left(\frac{2Z_1 Z_2 e^2}{dE} \cdot \frac{a}{d} \right)^{1/2} \qquad (14)$$

where d is the lattice spacing between the atoms along a row. Then the ion is steered by a series of successive small angle collisions to large depth which may be 3 to 8 times R_p depending on ψ_c, the degree of orientation and the temperature /22/.

The depth profile may further be seriously distorted by radiation enhanced diffusion, especially in metals of low melting point such as Pb, Zn or Cd /23/. Radiation enhanced diffusion may also occur during layer removal using the sputtering technique and may influence the measured depth profile. Thus theoretical ion ranges may be exceeded by at least a factor of ten.

With radiotracer techniques a deep penetration tail of the implanted species in the order of 1% of the total implanted amount was found in W which is a factor of 100 deeper than the theoretical R_p value /24/. This tail is thought to be due to the diffusion of interstitials which have a small probability of not being trapped. A deep penetration tail of similar size has also been observed for different dopants in Si using the window thickness-voltage method where the electrical activity of the implanted ions is measured over 3 to 4 orders down to a minimum detectable concentration of about 10^{12} ions/cm^3 /25/. In Fig. 2 a schematic drawing of the distribution of electrically active centers for boron-implanted contacts in high resistivity n-type Si is given near R_p (upper scale) and is compared to the measured results (lower scale). The donor concentration is $6 \cdot 10^{10}$ cm^3 for Si with a specific resistivity of 80 kΩcm.

In summary, although experimental and theoretical values for R_p and ΔR_p are in rather good agreement ($\pm$20%) various effects may influence the implanted ion profile and have to be taken into account.

1.2 Radiation Damage

Radiation Damage is a very complex subject where subtile interactions occur between defect production and defect annealing by athermal atomic motions, thermally activated motions and motions caused by other thermodynamic driving forces such as differences in binding energies and formation enthalphies etc.

The basic processes of damage production are well treated in the literature /2,3/. Here we will present only a few general guidelines and we will restrict our discussion to damage effects which may influence the results of high dose heavy ion implantation.

In order to study details of the defect production processes and to compare them with theoretical predictions based on the theoretical framework as discussed above it is necessary to separate the different possible influences. One possible way to study intrinsic defects, especially point defects and the formation small defect clusters is to irradiate very pure elemental targets with electrons at low temperatures (below 4K). At these temperatures it is known that interstitial atoms, having a rather high activation energy of formation (3-4 eV) but a very low activation energy of migration ($\sim$0.1 eV) are not yet mobile. At these temperatures annealing will mainly occur by athermal motions due to the high strain energy in the displacement field around the point defects. A spontaneous recombination volume between 50 and 100 atomic volumes is generally observed in agreement with computer calculations. While interstitials are mobile between 4 and 40 K, single vacancies have higher activation energies of migration (0.4 to 1.8 eV) although the formation energies are lower ($\leq$ 3 eV) than those of the interstitials. Thus the influence of vacancies on the annealing processes usually occurs at higher temperatures.

1.2.1 Cascade Effects

In contrast to electron irradiation, where well-separated point defects are produced, the slowing down of heavy ions causes so-called collision cascades. The incident ion may transfer a large amount of it's energy to a target atom in a primary knock-on event. The knocked-on target atom will collide with another lattice atom which in turn will displace a further

lattice atom. Thus we obtain an avalanche-like process of moving atoms which distribute the energy in successive collisions until the energy is below about E_d the minimum energy necessary to displace an atom from its equilibrium lattice site. The threshold displacement energy E_d is about 25 keV. A good demonstration of such an avalanche-like cascade production is given in Fig. 3 where computer calculations are shown simulating the slowing down process for 100 keV Ar-ions in Cu /26/. Individual cascades, called subcascades can be seen to be formed along the track of the primary ion. The number of subcascades formed and their distribution has to be taken into account in order to estimate the deposited energy density in a special ion-target combination. Under certain conditions, for example for low energy heavy ions implanted into a heavy mass target the probability for subcascade formation is less pronounced and the damage is uniformly distributed throughout the volume of a single cascade. Volume correction factors as a function of the mass ratio (M_2/M_1) have been evaluated in Ref. 27.

The number of displaced atoms N_d within a cascade can be evaluated, starting with eq. (10) which gives the nuclear stopping S_n via primary collisions during the slowing down process of the primary incident ion. In addition the slowing down process of secondary energetic recoils has to be considered and it has to be noted that the energy loss is again due to both electronic excitations and nuclear collisions, $\nu(E)$. Therefore $\nu(E)$ is about 20 to 30% smaller than the integrated nuclear stopping power ($\int_{E_d}^{E_o}$) value of the primary ion. Assuming that only those recoiled atoms become displaced which received an energy $E > E_d$, the total number of displaced atoms is obtained by dividing $\nu(E)$ by $2E_d$ /28/

$$N_d = \frac{0.8\ \nu(E)}{2E_d} \qquad (15)$$

N_d can now be compared with experimental results. For metals, although irradiated at 4 K, the observed number of displaced

atoms is usually about a factor of 10 smaller than predicted, suggesting that a large amount of spontaneous recombinations does occur during cascade production as it was discussed above for point defect production by electron irradiation.

In semiconductors, especially in Si, the measured number of displaced atoms is by a factor of 2 to 10 larger than predicted. This result clearly indicates that the binding properties of the materials play a prominent role in defect stabilization. Whereas in simple metals the binding is non-directional and the cohesive energy is below about 1 eV/At, in semiconductors strong covalent bonding prevails with about 2 to 3 eV/bond. For Si it was observed that for similar values of the nuclear energy loss $\nu(E)$ the number of N_d increases with increasing mass of the incident ions and that this effect is especially pronounced at lower energies indicating that non-linear energy density behaviour such as "spike-effects" may occur /29/. The concept to describe the slowing down process by a series of successive binary collisions with a fixed threshold energy does no longer hold if in a small cascade volume each atom receives more than 1 eV/At. A collective motion of all atoms in the cascade volume would be a better picture to describe this state. A detailed treatment of non-linear cascade effects from the theoretical point of view as well as from experimental manifestations is given in a recent review /13/. Within the thermal spike concept the cascade volume with radius r = 20 Å is considered to be in the liquid state and is quenched at a rate of t_q where $t_q \cong r^2/4D \cong 10^{12}$ sec, where D is the thermal diffusitivity ($D \cong 10^{-2}$/sec). These quench times are far smaller than those reached for splat cooling (10^{-6} sec) and pulsed laser irradiation ($\sim 10^{-9}$ sec) and are even smaller than those reached by vapor quenching on a LHeT-cooled substrate. From this result is may be inferred that cascade quenching would be an effective method to produce amorphous materials. The question which of the above mentioned techniques for amorphization is the most effective one is hard to solve as up to now

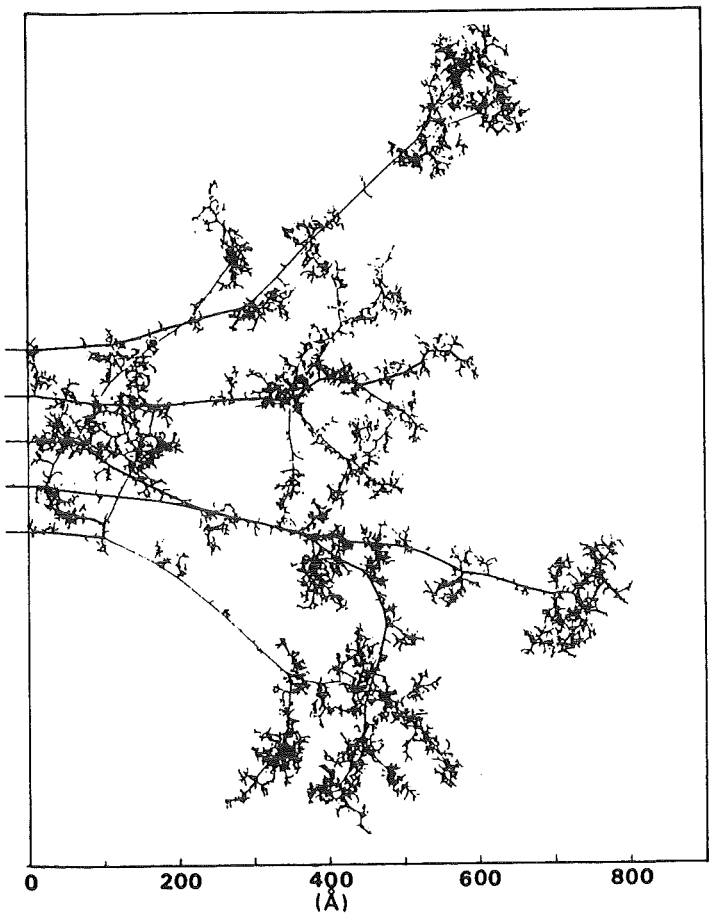

Fig. 3 Individual cascades as simulated in computer calculations (100 keV Ar^+ → Cu) /26/.

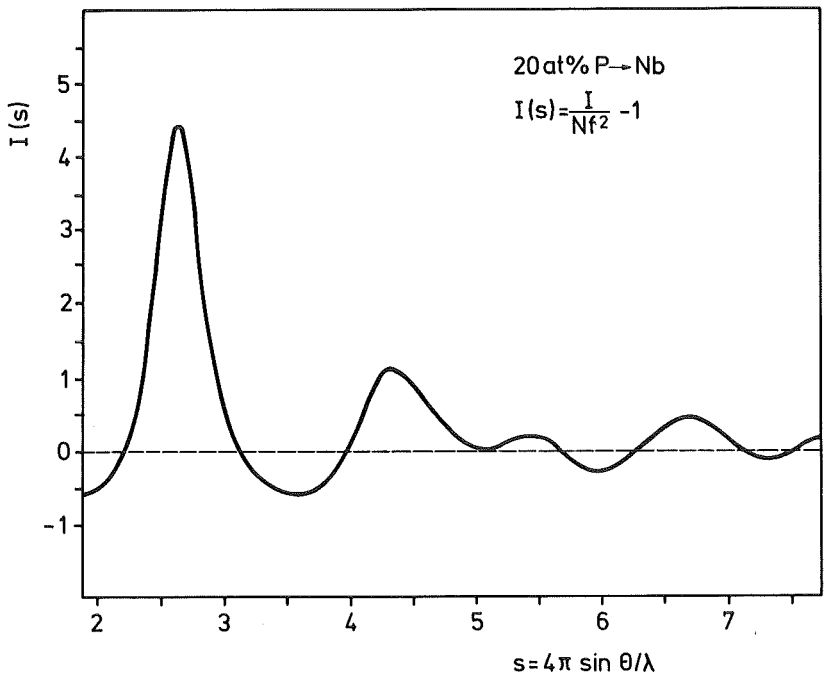

Fig. 4 Interference function of a Nb-layer implanted homogeneously with 20 at.% P /33/.

only amorphous two-component metallic systems have been stabilized by vapor quenching as well as by irradiation with about the same success /30/. The stabilization of the amorphous phase is then due to chemical binding forces or due to differences in the atomic radii which provide structural stability of a random atomic arrangement. For pure gallium, as an exception /31/, the amorphous state can be stabilized by vapor quenching. In a recent study it was shown that pure gallium could also be amorphizised by low-temperature (< 10 K) ion irradiation /32/. The importance of the energy density within the cascade for the phase transformation has been demonstrated in these experiments by using He, Ne and Ar-ions. Amorphization is obtained only be Ne and Ar-ion irradiation. Further it was demonstrated that the crystal structure of the surrounding matrix plays a crucial role for the recrystallization process during irradiation. Irradiation of the less stable β-Ga crystalline phase did not lead to a phase transformation.

Amorphous materials as produced by vapor quenching, by ion irradiation or implantation are often contrasted to so-called glassy metals which have been formed by rapid or by very slow cooling (undercooling) from the melt. It is thought that the amorphous states would reveal different short range order. Apart from all the difficulties to determine the short range order from radial distribution functions such a study has been performed for a-$Nb_{80}P_{20}$ produced by homogeneous P-implantation in a Nb thin film /33/. First evaluations of the interference function shown in Fig. 4 indicate that a liquid like amorphous phase had indeed formed.

1.3 Lattice Location

From the theoretical point of view, considering the slowing down process as a series of binary collisions, the implanted ion should have a certain probability to end up on a substitutional lattice site by undergoing a replacement colli-

sion. The conditions for such a replacement collision can be given according to /34/ as follows: the energy T transferred to a host atom must be equal or greater than E_d, the threshold displacement energy. If the rest energy E-T of the primary ion is smaller than E_d then there exists a certain probability that the ion will recombine with the lattice vacancy and become substitutional. The probability for replacement collisions has been calculated for all ion-target combinations and lies between zero and 0.8 /34/. The theory is based purely on ballistic arguments and does not consider the chemical nature of the incident ion. On the other hand, nonlinear cascade theory can be applied. The incident ion comes to rest in a region, where all atoms are in motion on a time scale of 10^{-12} sec. The nonlinear cascade region is then quenched by thermal diffusion, followed by a recrystallization from the surrounding crystalline matrix. The lattice site of the primary ion would then depend on the state in the cascade region. If this state is liquid-like then the lattice site occupation would depend on the solubility of the foreign atom in the liquid host and thus on thermodynamic arguments.

The experimental results on diluted solid solutions produced by ion-implantation have been summarized in recent reviews /35/. The results are usually depicted in a Durken-Gurry plot (electronegativity, χ, versus atomic radius, r). Applying the Hume-Rothery criteria for equilibrium alloys ($\Delta r/r_h = \pm 0.15$ (h=host); $\Delta\chi = \pm 0.4$) it has been noted that these rules are exceeded for implanted solid solutions. Modified rules have been suggested /9/ ($\Delta r/r_h = -.15$ and $+.40$; $\Delta\chi = \pm 0.7$) and these rules are valid for about 90% out of 63 implanted alloys. As an example the Darken-Gurry plot for various ions implanted into V is shown in Fig. 5a. There are several remarkable exceptions to the modified Hume-Rothery rules (dashed line). Iodine and selenium are substitutional although they are outside the limits given by the modified rules. Whereas implanted species from groups III_a to VII_a have a high substitutional solubility those of groups I_a and II_a are relatively insoluble in V in agreement with similar observations made previously for Al,

Cu and Fe as host lattices /35/. First results for Cs implanted at 5 K and analyzed at this temperature showed that the substitutional fraction SF, is about 0.5. For the system VXe SF is also about 0.5. These results show that point defect migration during implantation at room temperature drastically influence the local atomic arrangement near the foreign atom. As VXe and VCs are extreme cases concerning electronegativity and atomic radii, respectively, it is concluded that the Hume-Rothery-coordinates play a minor role for implanted systems.

Besides the Hume-Rothery coordinates the lattice site occupation may be determined by cascade effects. Thus the measured SF will be compared to the theoretically determined replacement collision probability /34/. For VBi SF is about 1, irrespective of the implantation temperature (see Fig. 5b). This value is far larger than that determined from the replacement collision theory. In agreement with the conclusion drawn previously for CuBi and CuW /35/ it is clear that replacement collisions alone are not sufficient in explaining substitutionality. It is remarkable, however, that the results for VXe and VCs are in agreement with theory. The results for VCu, VSe and VKr are not yet conclusive as the concentration dependence of SF has not been studied in detail up to now.

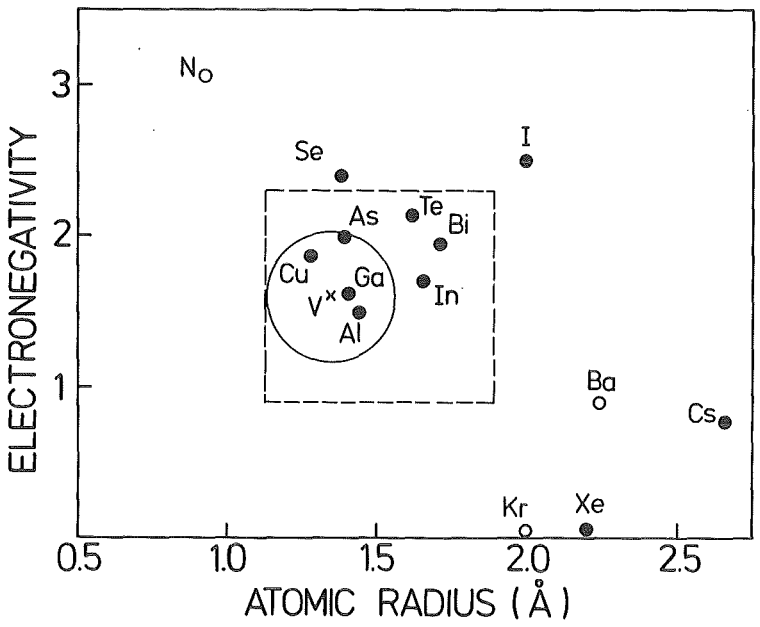

Fig. 5a Darken-Gurry plot for dilute implanted alloys in V.
● substitutional;
o nonsubstitutional.
The circle indicates the Hume-Rothery zone, the dashed line represents the modified Hume-Rothery zone /36/.

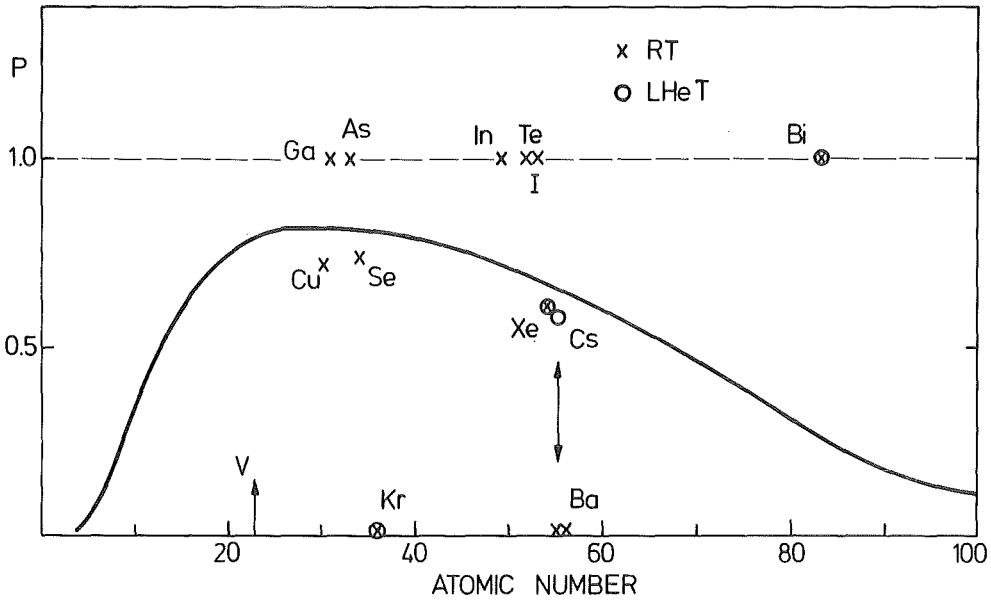

Fig. 5b Replacement collision probability in V (solid line /34/ and measured substitutional fraction of diluted (∿0.01 - 0.1 at.%) alloys produced by ion implantation.

2. Applications in Materials Science

Ion implantation is extensively used by the semiconductor device industry as a method for doping semiconductors with acceptor or donor centres in order to form p-n junctions. The main advantage as compared to doping by thermal diffusion is that the amount of dopants and the dopant profil can accurately be controlled and reproducibly be specified. High value resistors in integrated circuits can also be manufactured by ion implantation in a controlled way. In special devices such as the metal-oxide semiconductor transistors which are extensively used in large-scale integrated circuit stray capacitance can be substantially reduced and threshold voltages can be adjusted by ion implantation. These potentials are treated in detail in references /4,5,6/ for example. Here we will shortly describe the production and performance of an ion implanted nuclear particle detector. In a second example the formation of supersaturated Si-As alloys by ion implantation and pulsed electron beam annealing is studied.

The application of ion implantation to modify other material properties including corrosion, oxidation, mechanical and catalytic behavior, optical effects and superconductivity are treated in Ref. /7/. Here we concentrate on basic metallurical effects which are mainly responsible for the observed changes in the physical properties of metals.

2.1 Semiconductor Doping

High resolution nuclear particle detectors have been produced by implantation of P and B-ions at low energies up to 10 keV in the front and rear area of high resistivity n-type Si (10 - 135 kΩcm, 0.3 - 4 mm thick) respectively to produce $p\text{-}n\text{-}n^+$ junctions /37/. This devices can be fully depleted such that the space charge region extends up to the back-contact. Electron-hole pairs as produced by nuclear radiation can be collected over the whole thickness of the silicon slice. The

response of such an ion-implanted detector to alpha-particles of an ^{241}Am-source is shown in Fig. 6. The implantations have been performed within 0.5 degree parallel to the <111> Si-crystal direction. By using well-channeled ions at low concentrations damage effects were minimized. Low temperature annealing up to 300°C for 10 min was found sufficient to produce junctions iwth good current/voltage-characteristics and long lifetimes of the minority carriers (1-2 msec). Such detectors proved to be more stable to changes of ambient athmosphere and of vacuum than surface barrier detectors.

The annealing of radiation damage is a most serious problem in semiconductor doping by ion implantation. For high dose implants in Si the implanted region becomes amorphous and thermal annealing has to be applied near 600°C in order to trigger an epitaxial regrowth of the amorphous layer starting from the crystalline to amorphous interface /4/. We have studied the effects of pulsed electron beam annealing of ion implanted Si-crystals /38,39/. The generally accepted annealing mechanism due to irradiation by high-energy pulsed laser or electron beams, involves melting of the surface layer followed by a liquid phase epitaxial regrowth. This has the advantage that the molten zone can extend beyond the less sharp amorphous to crystalline interface which may not completely anneal out in the thermally activated solid state regrowth process. The dopant concentrations incorporated into substitutional lattice sites can largely exceed the equilibrium solid solubility limit at the melting temperature of the substrate.

We have produced supersaturated surface alloys by very high dose ($0.8 - 2.6 \cdot 10^{17}/cm^2$) implantation of As-ions into silicon and studied the effect of subsequent pulsed electron-beam annealing (PEBA) by means of the Rutherford-backscattering and channeling technique /38/. The energy density deposited by the pulsed electron beam was in the range from 1.0 to 2.3 J/cm^2. The melting threshold is reached at 1.0 J/cm^2. The pulse duration was 300 ns and the maximum accelerating voltage was about 18 kV /39/. The annealing capability of PEBA is demonstrated in Fig. 7.

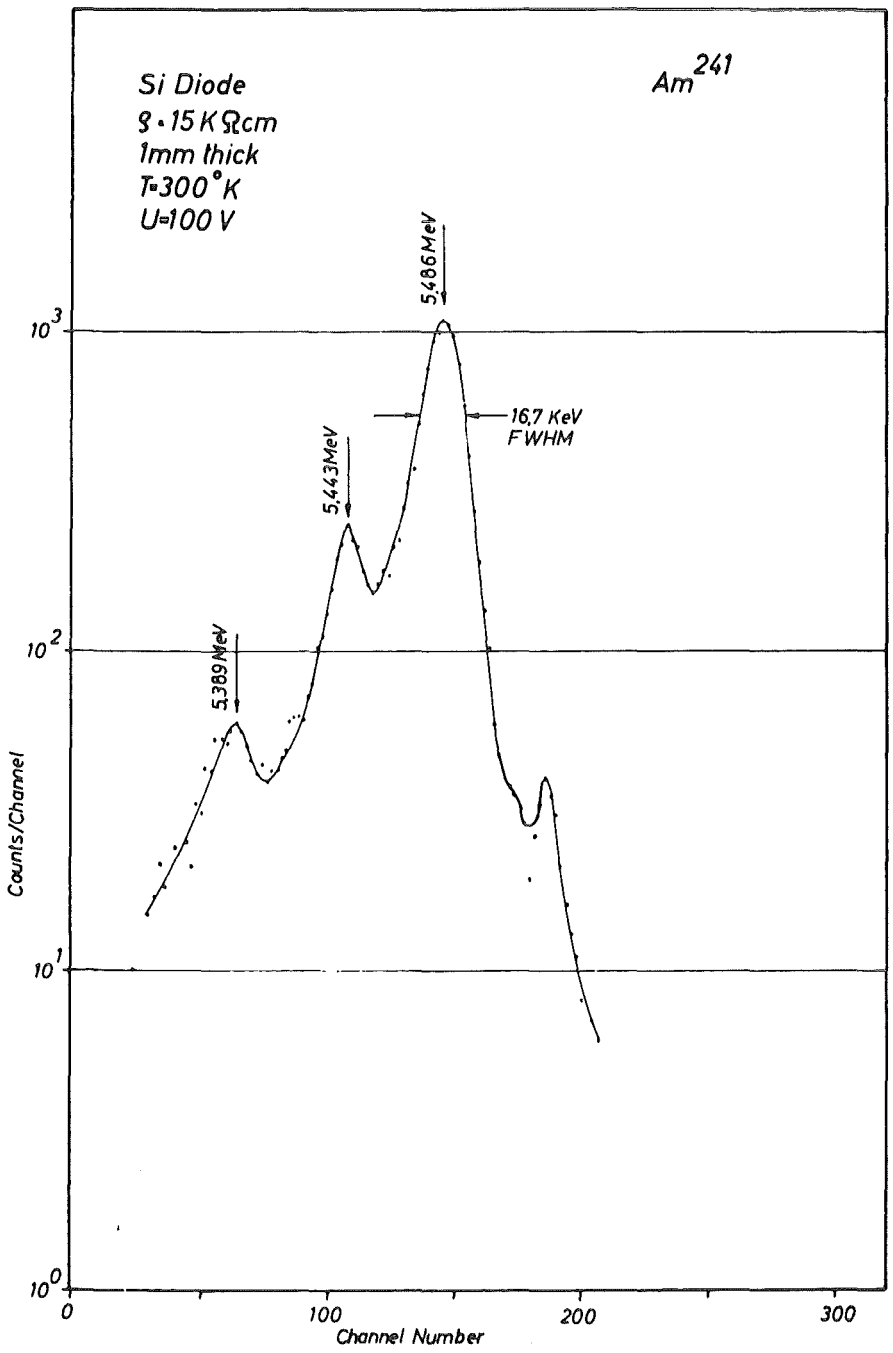

Fig. 6 Response of an ion-implanted nuclear particle detector to ^{241}Am alpha-particles /37/.

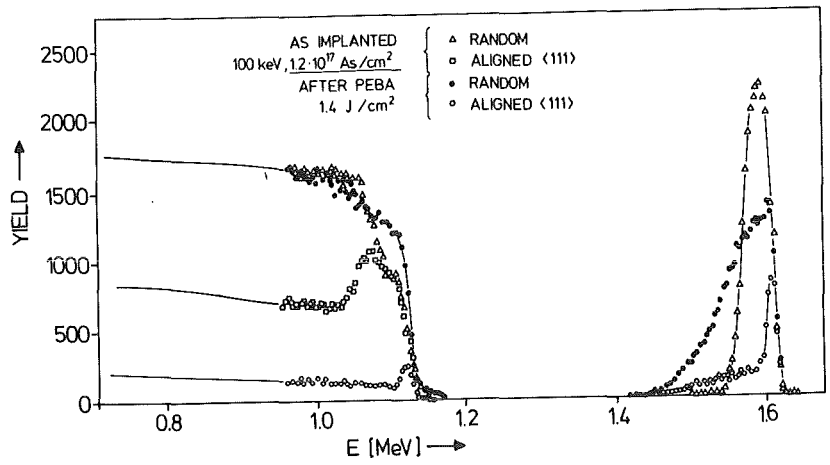

Fig. 7 Random and <111> aligned backscattering spectra from an As-implanted Si-single crystal before and after pulsed electron beam annealing, PEBA /38/.

After implantation of $1.2 \cdot 10^{17}$ As^+/cm^2 the implanted region is completely amorphous. It is interesting to note that the stopping power changes strongly in the implanted region due to the high As-concentration ($\sim$ 25 at.%) and induces a reduction of the Si-yield (step in the random spectra at the Si edge) in the amorphized region. The arsenic depth distributions is Gaussian like (see eq. 13) with the maximum located at a depth of 500 Å. After pulse annealing with 1.4 J/cm^2 a broadening of the As-depth distribution is observed. The peak concentration is reduced to 13 at.%. The reduction of the As peak concentration is also indicated in the reduced step height of the random spectra at the Si-edge. The aligned spectrum shows a strong reduction of the scattering yield for both the host and the As-atoms. The minimum yield from Si (7%) is somewhat higher than that from the virgin crystal (3.5%) indicating that at such high As concentration some defects are left, mainly produced by small displacements (0.01 nm) of the As atoms from their substitutional lattice sites. This result was obtained by evaluating angular scan measurements as a function of As-concentration /38/. The maximum solubility limit was found to be $7 \cdot 10^{21}$ As/cm^3. This value exceeds the equilibrium value by a factor of 4 and is slightly higher than in the liquid ($5 \cdot 10^{21}$ As/cm^3) at the retrograde temperature. From these results one can conclude that ion implantation combined with pulse annealing is a very efficient technique to form supersaturated alloys in semiconductors.

2.2 Implantation Metallurgy

The formation of metastable phases by ion implantation is unavoidably connected with the production of radiation damage which in turn will effect the physical properties of the material. Ion implantation may also lead to radiation induced phase transformations in multicomponent systems and thus hide the doping effect of the implanted ions. One way to unravel radiation induced effects from ion implantation effects is to perform additional so called irradiation experiments using self-

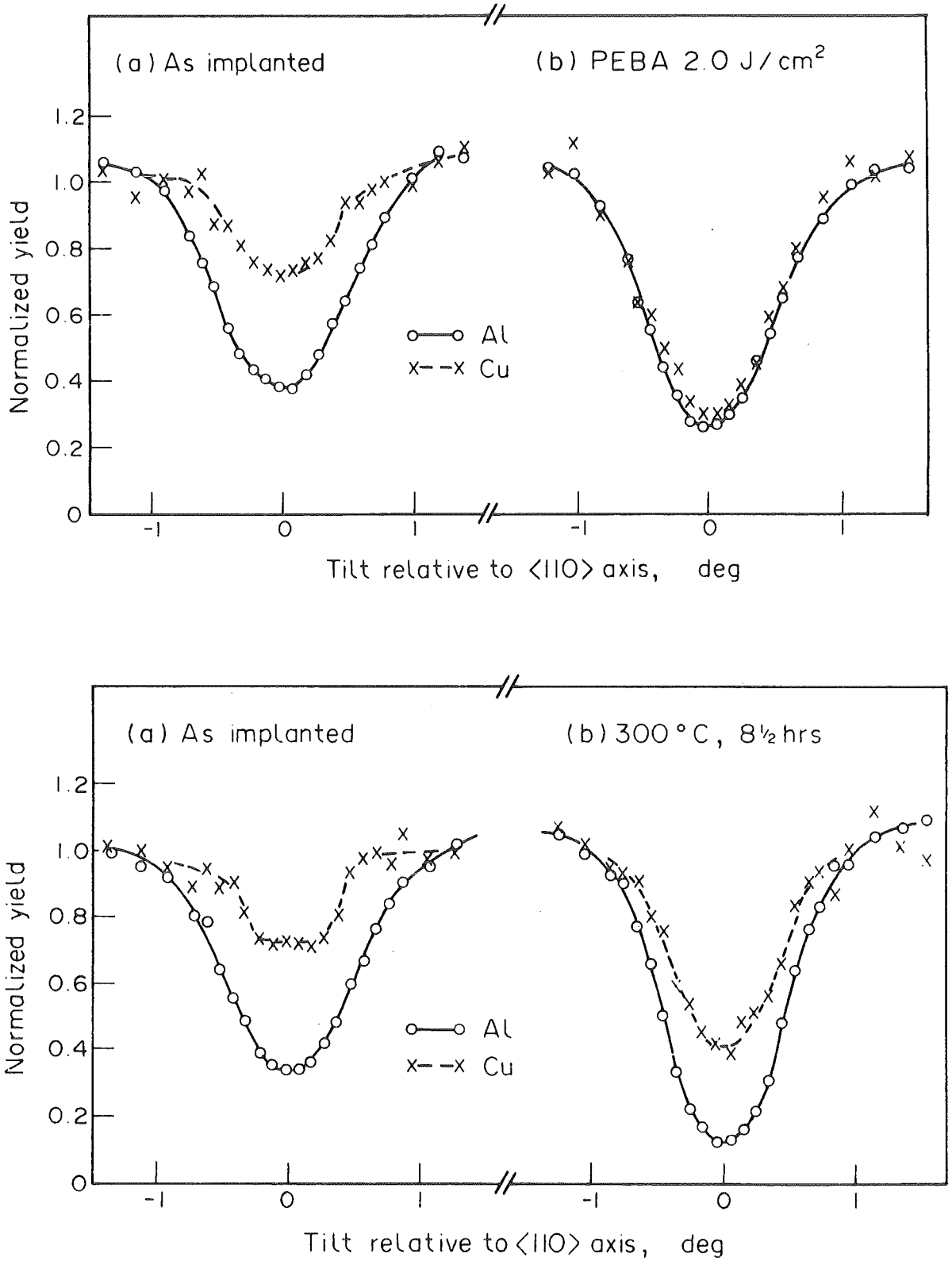

Fig. 8 Angular scans through the <110> axis for an as-implanted Al-crystal (2.9 x 10^{16} Cu^+/cm^2) (a) and after PEBA with 2 J/cm^2 deposited energy density /40/. For comparison the effect of furnace annealing at 300°C for 500 min is shown in Fig. 8b.

ions or noble gas ions which are chemically inert. The formation of intrinsic defects such as point defects and extended defects and their influence on the materials properties as well as the influence of cascade effects and of radiation enhanced diffusion can be studied by such irradiation experiments of pure monocomponent targets. If the target contains impurities in low concentrations, impurity stabilized defects may be produced such as dumbbells or amorphous zones. Irradiation of multicomponent targets may lead to radiation induced lattice site exchange of atoms metastable compound formation, and amorphization. Some examples of such irradiation experiments will be treated in the chapter on radiation damage effects. In the next two sections the formation of extended alloys and the formation of compounds by ion implantation will be discussed.

2.21 Extended Solid Solubilities

In chapter 1.3 it was shown that ion implantation is a suitable technique to form supersaturated substitutional alloys in most of the metals as a large amount of the defects produced will anneal out during implantation at room temperature. This observation is in contrast to results from implantation experiments in many semiconductors, where amorphization will occur during implantation at room temperature and damage annealing by epitaxial regrowth in the solid phase or from a short-lived melt has to be performed as discussed in chapter 2.1 for Si. Transient annealing techniques such as laser or electron beam annealing have also been used for the processing of ion-implanted metals to form metastable alloys with solubility levels exceeding the values from equilibrium phase diagrams.

The system Cu_2Al_{98} is discussed to demonstrate that by electron pulse annealing above the melting threshold the synthesis of supersaturated alloys is more successful than by thermally activated annealing in the solid phase /40/. Though the equilibrium solubility of Cu in Al at room temperature is very low (< 0.1 at.% at 250°C) a supersaturated solid solution with 2.1 at.% Cu on substitutional sites was formed by pulsed

electron beam annealing using deposited energy densities of about 2.0 J/cm^2. This result is obtained by evaluating the angular scan curves in Fig. 8a. The substitutional fraction S for the Cu-atoms is given by $S = (1 - \chi_i)/(1 - \chi_h)$ where χ_i and χ_h are the normalized minimum yield values for the impurity and the host atoms respectively. In the as-implanted sample S is about 0.4 whereas after PEBA an almost complete agreement of the angular scans from the impurity and the host lattice atoms is observed resulting in a substitutional fraction of about 0.95. Angular scans from the crystal before and after thermal annealing at 300°C for 8 1/2 h are shown in Fig. 8b. For the as-implanted sample S is about 0.4 while after thermal annealing a value of 0.66 has been determined. The disagreement between the critical angles of the host and impurity atoms shows that after thermal annealing the impurity atoms are still somewhat displaced from the regular lattice sites. For prolonged annealing time at 300°C diffusion of Cu into the Al-sample has been observed.

In summary, an improvement of the solubility above the value from the equilibrium phase diagram has been obtained by PEBA. This result is thought to be due to the fast quenching rate ($\sim 10^{-9}$ sec) preserving the high solubility of Cu in Al in the liquid state down to room temperature. The reduced substitutional fraction for the as-implanted sample indicates that the rapid quench mechanism from a liquid-like nonlinear cascade region as discussed in chapter 1.3 can not directly be applied. Further studies will be carried out to elucidate this point for low melting point metals where radiation enhanced diffusion effects are known to occur /23/.

The formation of interstitial solid solutions by implanting hydrogen and deuterium ions in different metals and alloys at liquid helium temperature has led to the discovery of many interesting superconducting alloys /41/. Some of these alloys have later also been produced by using high pressure or electrical H-charging at low temperatures ($\sim$ 200 K). The T_c-values ob-

tained by the implantation technique have been confirmed. From these results it can be concluded that defects produced during implantation either anneal out or do not influence T_c.

In this paragraph we will discuss the formation of interstitial solid solutions of oxygen and nitrogen in transition metals where the solid solubility is limited to 3.5 at.% O and to about 1 at.% N /42/. T_c is found to decrease almost linearly by 0.9 K/at.% for oxygen in niobium and the lattice parameter a_o increases linearly by $4.3 \cdot 10^{-2}$ nm/at.% /42/. By implantations of oxygen and nitrogen ions in molybdenum /43/ and niobium /44/ thin films, substantial changes of T_c and a_o have been observed. In these experiments T_c of Mo increases from 0.9 up to 9.2 K and T_c of Nb decreases from 9.2 to 1.4 K. The increase of a_o with increasing N-concentration in Nb is shown in Fig. 9 /44/. The slope of about $4 \cdot 10^{-2}$ nm/at.% up to 20 at.% N is in good agreement with the value obtained for O in Nb as mentioned above. In the nitrogen concentration range above 20 at.% the high angle X-ray lines disappears and only broad low angle lines were observed indicating heavy structural distortions towards amorphization. At 30 at.% N new lines appear in the X-ray photographs due to the formation of niobium nitride phases. This compound formation processes will be discussed in the next chapter.

The formation of supersaturated interstitial alloys by implanting C, N or O-ions is accompanied with local displacement fields which can be determined by evaluating the X-ray line intensities using modified Wilson plots /44/. Such plots are shown in Fig. 10 for four different concentrations of N in Nb. The slopes of the lines are seen to increase with increasing nitrogen concentration indicating growing distortions of the structure and a weakening of the transition metal bonds by the lattice dilatation caused by the nontransition metal. The weakening of the transition metal bonds may lead to a stable amorphous phase at about 20 at.% impurities as was observed for Mo /33,45/, Re /46/ and for Nb /47/. The

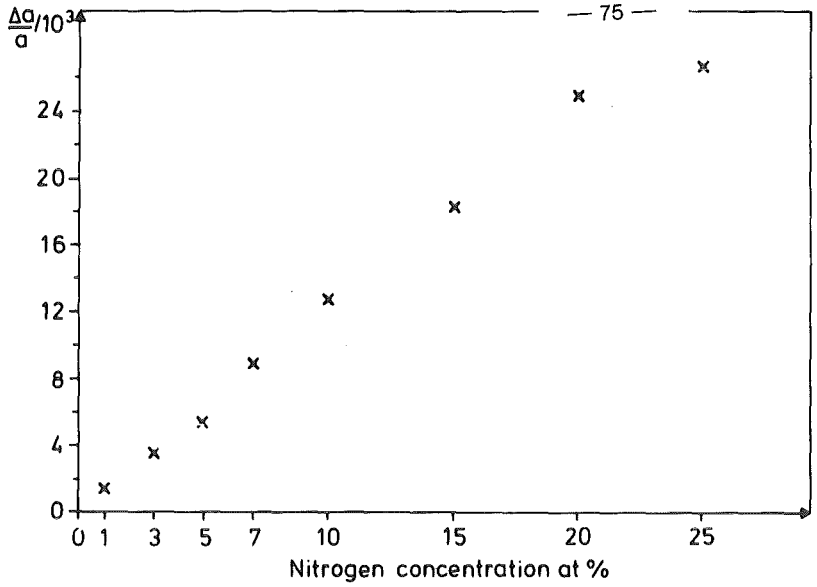

Fig. 9 Relative increase of the lattice parameter of Nb as a function of the concentration of implanted N /44/.

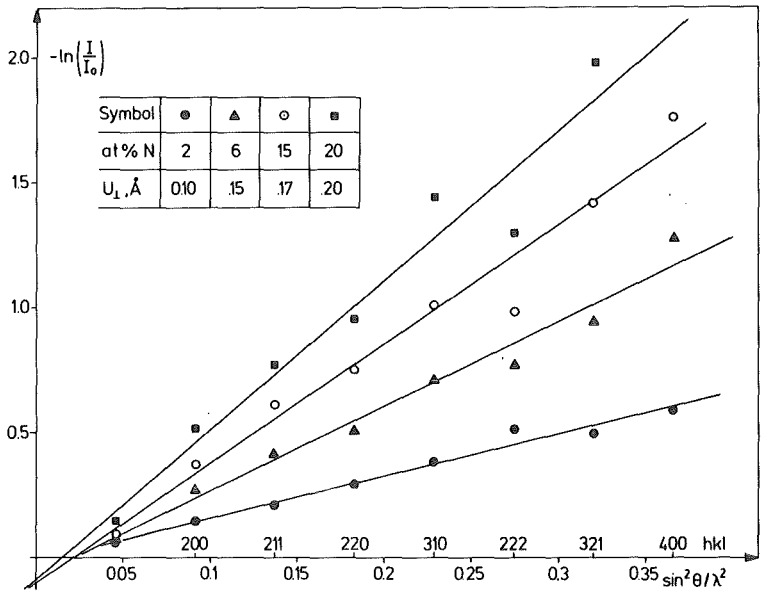

Fig. 10 Wilson plots for nitrogen implanted Nb-layers. Displacement values u as calculated from the slopes are indicated in the figure /44/.

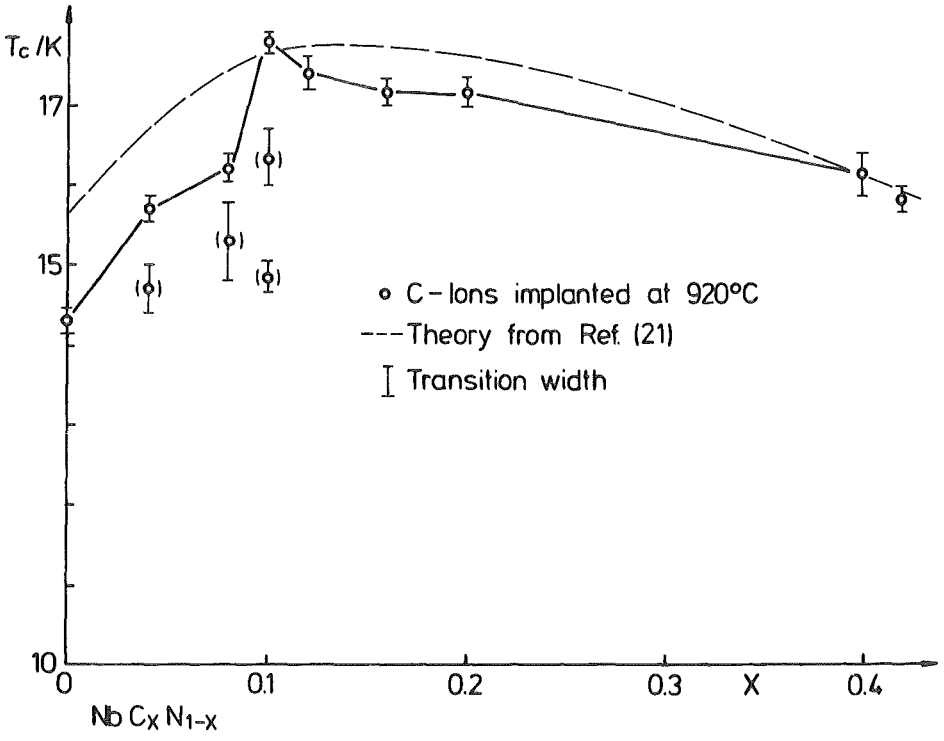

Fig. 11 Superconducting transition temperature of NbC_xN_{1-x} vs. composition x as altered by C-ion implantation /51/.

process of amorphization by ion implantation will be discussed in chapter 2.3.3.

In summary, supersaturated interstitial alloys have been produced by ion implantation. The conclusion that the implanted impurities are located on interstitial sites is not only drawn from the lattice parameter increase having a similar slope-value than interstitial alloys in thermal equilibrium but also from channeling experiments /48/, where the interstitial lattice site of N in Nb has directly been determined.

2.2.2 Compound Formation by Implantation

The use of high dose heavy ion implantation as a method to form metastable compounds may be affected by the sputtering effect. From the sputtering yield and the mean range of the ions one can easily evaluate the maximum concentration retained in a target. The sputtering yield will not only limit the amount of impurities that can be implanted but will also affect the implanted profile. One way to overcome this disadvantage of ion implantation is to use atomic mixing of atoms by irradiations of the interface of a thin film couple with heavy self-ions or noble-gas ions and to study the ion-induced interfacial reactions. Ion beam mixing has been used to form metastable alloys and compounds /49/. The question whether atomic mixing will occur by ballistic effects or be caused by thermodynamic forces can not be answered in a general way and does depend clearly on the chemical bonds which prevail in the used materials. In some systems e.g. for Pd layers on Si the amount of mixing was found to increase strongly by passing over from the linear collision cascade regime to nonlinear cascade mixing /49/.

In the following examples of compound formation by ion implantation will be discussed. It will be shown that for high dose light ion implantation the sputtering effect is small and stoichiometric nitrides with NaCl-structure can be produced by nitrogen implantation in transition metals with bcc- or hcp-

structure. These nitrides with B1 crystal structure are stable against ion-irradiation and they do form by implantation although in the equilibrium phase diagram these phases are indicated as metastable or do no exist at all as for example MoN /50/.

Many refractory materials show deviations from stoichiometry as these compounds reach a minimum of the free energy by incorporating a certain amount of vacancies. The T_c-values are known to decrease with increasing vacancy concentrations in both sublattices. Ion implantation would be a useful technique to compensate these deviations from stoichiometry if optimum conditions for disorder annealing could be found. This subject has been discussed in more detail in a recent review /30/. Carbon implantations have been performed in $VC_{0.88}$ and in $NbC_{0.83}$. Radiation damage analysis was carried out using the channeling technique /30/. The influence of light ion implantation in NbC has also been studied /30/.

Here we will shortly describe the results of C-ion implantation into $NbN_{0.85}$ single crystals with B1 structure and a T_c-value of 14.3 K in order to form $Nb(C_xN_{1-x})$ compounds /51/. The main result of this study is shown in Fig. 11. The implantation temperature of 920°C was found to be an optimum between radiation damage annealing and enhanced diffusion which would tend to drive the system back to the thermal equilibrium. In Fig. 11 T_c increases up to a maximum value of 17.8 K at about 10 at.% C. This maximum T_c-value which is in close agreement with values obtained for bulk samples indicates that the implanted C-ions are located on the nontransition metal lattice sites due to short distance diffusion after implantation at 920°C.

In chapter 2.2.1 it was shown that by ion implantation of nitrogen into molybdenum an amorphous phase was produced with a T_c of 9.2 K at a N concentration of about 20 at.%. For higher N concentrations a phase transformation from the bcc to a fcc-phase via the amorphous phase was observed. The lattice parameter of these phases, which have been produced not only by

ion implantation but also by reactive sputtering in a N/Ar gas mixture or in a pure N plasma are shown in Fig. 12 as a function of N-concentration. The specific resistivity for MoN films with stoichiometric composition reached values up to 1000 μΩcm, probably due to columnar growth with small grain size /50/.

In contrast to the formation of MoN via bcc/amorphous/fcc transformations with increasing N concentration, the hcp rhenium phase and the fcc rhenium nitride phase formed by N implantation /46/ were both present for N-concentrations between 13 and 45 at.%. Above 45 at.% N only the fcc phase was observed. For stoichiometric ReN the lattice parameter was 4.021 Å, the specific resistivity was 230 μΩcm and T_c was 4.5 K. Implantation of N at liquid nitrogen temperature caused a phase mixture of B1 ReN and an amorphous phase. Storage of ReN at RT for 2 months caused a decomposition indicating that the implanted phase was unstable.

Besides the formation of intermetallic compounds during the implantation process another possibility is the production of supersaturated solid solutions or amorphous mixtures by implantation and to transform these mixtures by a thermally activated nonequilibrium process into a compound. As an example for such a transformation the nucleation and growth of V_3Ga with A15 structure from ion-implanted supersaturated Ga-V solid solutions has been studied /52/. The implantation of Ga in V single crystals and V thin films was performed at room temperature. Channeling measurements (see Fig. 13) and thin film X-ray diffraction studies revealed that the as-implanted Ga is substitutional up to about 35 at.%. This concentration is limited by the sputtering effect. The nucleation of the A15 phase starts at the surface as can be seen in Fig. 13c. The transformation is completed at 800°C (Fig. 13d). For Ga concentrations above 25 at.% a polygonization of the implanted layer is observed after isochronal annealing at 700°C for 30 min and thus nucleation centers (grain boundaries) are now available within the whole implanted region.

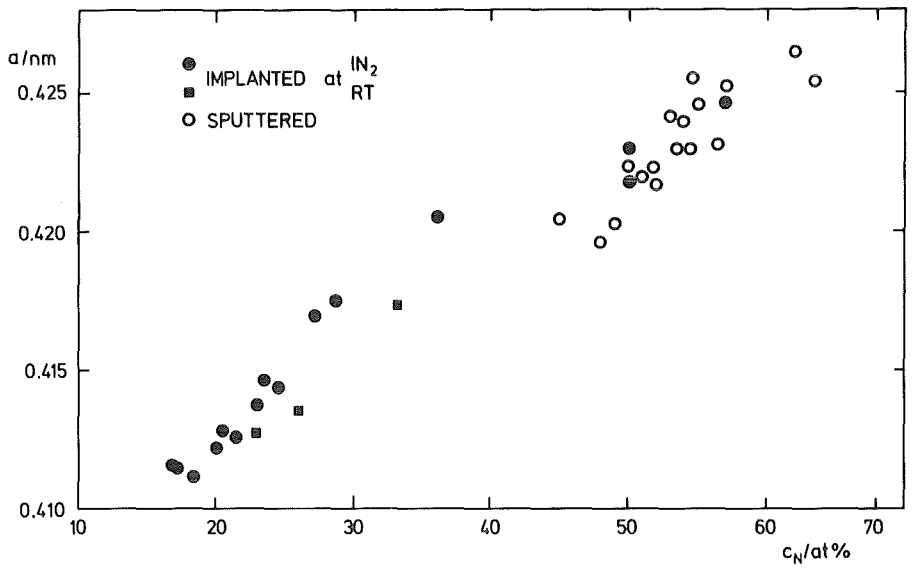

Fig. 12 Lattice parameter as a function of N-concentration in B1-MoN_x as prepared by reactive sputtering and by N-ion implantation /50/.

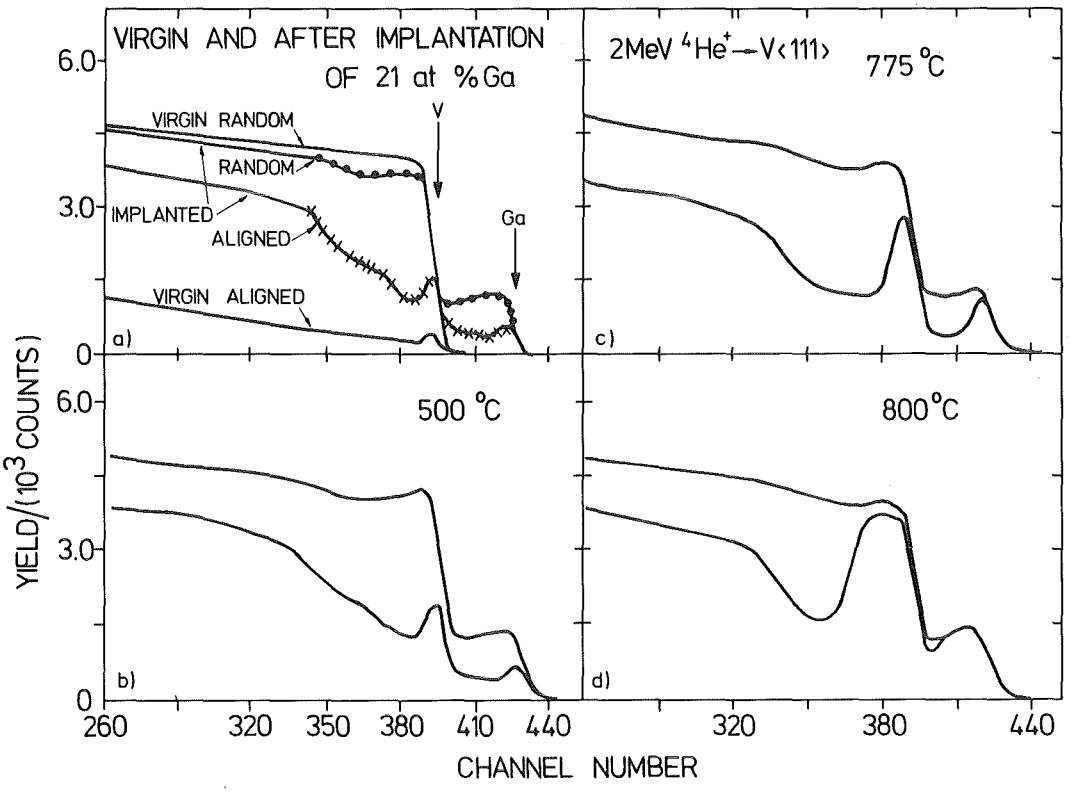

Fig. 13 Typical channeling and backscattering spectra for a homogeneous high dose (21 at.%) Ga-ion implantation in a V-single crystal as a function of the annealing temperature to demonstrate the nucleation and growth of the A15 phase /52/.

Besides thermally activated phase transformations of supersaturated solid solutions and amorphous mixtures as produced by ion implantation pulsed electron or laser beam annealing can be applied /53/. Both annealing procedures have been applied to $Nb_{75}Ge_{25}$ mixtures either being amorphous or being in the A15 phase however distorted by different degrees of radiation damage. Nb_3Ge with A15 structure is the material which has the highest T_c of 23 K known. Irradiation with electrons or protons will reduce T_c to a saturation value of about 4 K without affecting strongly the crystalline structure. In contrast, irradiation with Ar-ions will completely amorphize Nb_3Ge however the T_c-value of amorphous Nb_3Ge is also about 4 K. Thus the effectivity of the annealing process can be checked by registering the T_c-recovery. From Fig. 14 it can be seen that the maximum T_c-value obtained in the isochronous annealing process at about 850°C, is strongly dependent on the amount of damage in the sample before annealing. Complete T_c recovery is only obtained for the H^+-irradiated slightly damaged samples. Samples which were X-ray amorphous after high dose Ar^+ irradiation revealed similar recovery curves as those obtained by annealing sputtered amorphous $Nb_{75}Ge_{25}$ films. Annealing of amorphous $Nb_{75}Ge_{25}$ mixtures by pulsed electron beams using energy densities up to 5 J/cm^2 lead to the formation of crystalline A15 phases with moderate T_c-values together with the stable tetragonal phase. Thus it is concluded that the growth velocity during pulse annealing may be too high to form well ordered A15 compounds.

The equilibrium A15 phase with the composition $Nb_3(Ge_{0.8}Nb_{0.2})$ and a T_c-value of 6.5 K has been implanted with Ge at room temperature and was then subjected to a similar isochronal annealing process. The results are also included in Fig. 14. Also the implanted surface region was found to be amorphous after implantation, it did epitaxially regrow on the crystalline bulk sample /54/. A possible explanation for the rather low maximum T_c-value would be the incorporation of defects during the regrowth from amorphous phases.

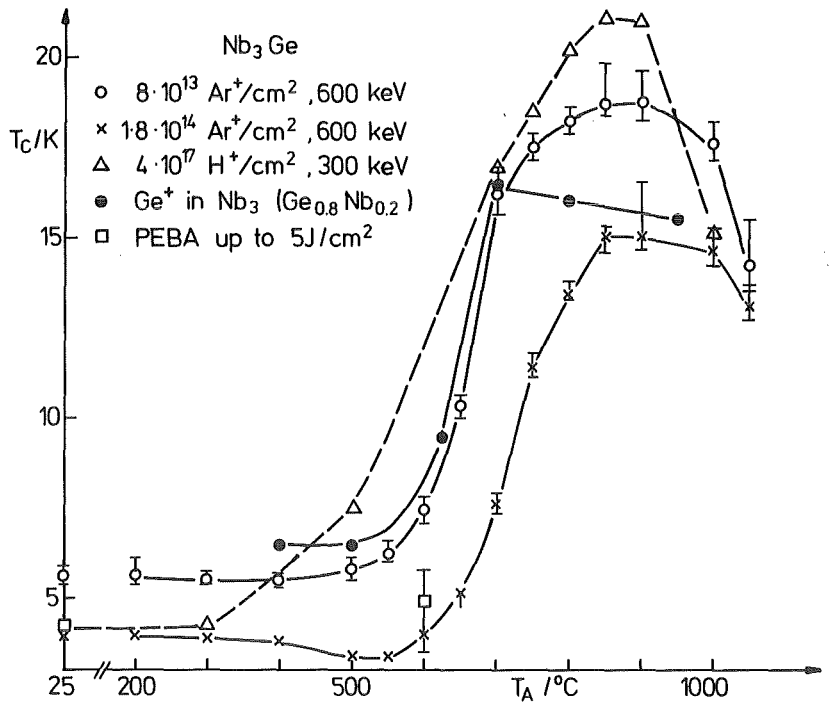

Fig. 14 T_c-recovery of Nb_3Ge films, predamaged to different levels of disorder. Thermal annealing of a Ge-implanted $Nb_3(Ge_{0.8}Nb_{0.3})$ A15 phase is included for comparison /53/.

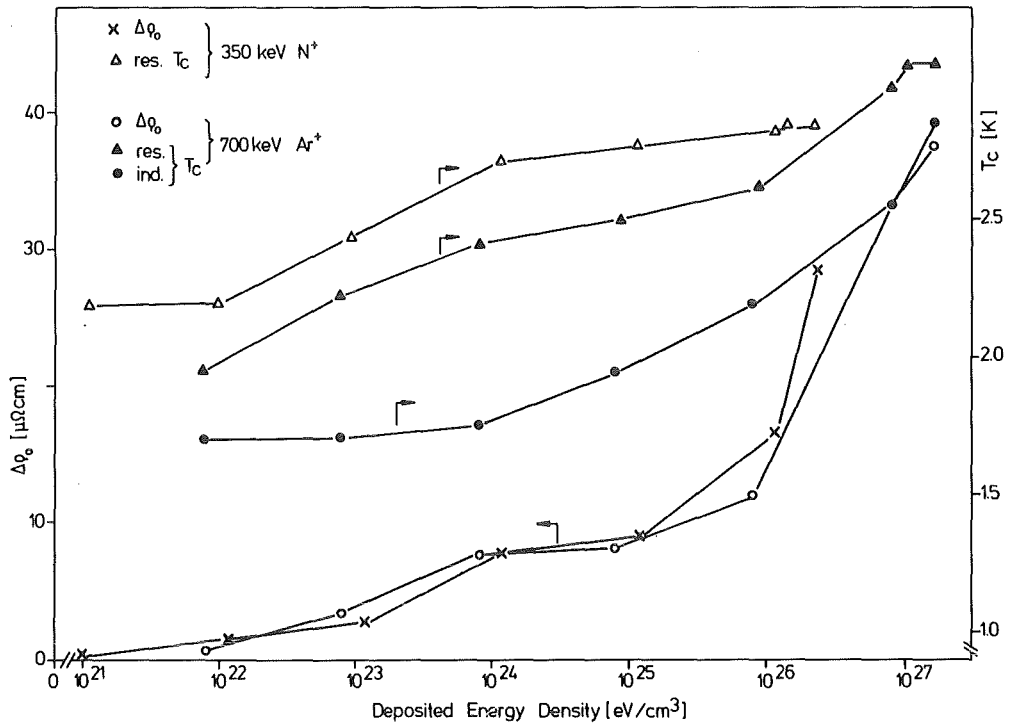

Fig. 15 Changes of the residual resistivity $\Delta\rho_0$ and the superconducting transition temperature T_c of Re as a function of the deposited energy density during irradiation with N^+- and Ar^+-ions /55/.

In summary, compounds have been improved by compensating deviations in composition from stoichiometry. New metastable compounds have been synthesized. The application of ion implantation and pulse annealing is of limited success for well-ordered systems with complex crystal structures with regard to superconductivity as this property is strongly affected by antisite defects and local displacement fields.

2.3 Radiation Damage

It is well known that intrinsic defects may affect the physical properties of materials. The introduction of extended defects by plastic deformation or irradiation could lead to a hardening. The Debye temperature is then reduced followed by a decrease of the specific heat. The vibration spectrum of the atoms next to a vacancy in contrast may be shifted to lower frequencies and thus may enhance the electron-phonon-coupling in some metals as will be discussed here for the case of Re. In metals containing small amounts of impurities special intrinsic defect impurity associates may form during irradiation and may alter the physical properties. With increasing density of extended defects or with increasing strain around point defects in solid solutions the free energy of the material may increase to values larger thanthose of other possible metastable phase. Thus a spontaneous transformation to metastable or amorphous phases may occur.
The following examples are given to illustrate the influence of such defect structures on the superconductivity.

3.2.1 Defects in Elements

It has been observed /56/ that T_c of Re single crystals increases when this crystals were heated close to the melting point and then rapidly quenched. The T_c increase was attributed to vacancies which are thought to shift the vibrational spectrum to lower energies and thus to strenghten the electron-phonon-coupling. In Re isolated vacancies are stable for temperatures up to 500 K.

The influence of radiation induced defects on T_c, ρ_o (residual resistivity at 4.2 K) and the structure of Re films was studied in irradiated samples as a function of nitrogen and argon ion fluence /55/. The film thickness used was smaller than the ion ranges, thus most of the ions could penetrate the film and come to rest in the substrate. The nuclear energy loss of Ar is about 6 times larger than the nuclear energy loss of N ions. In order to compare the resistivity and the T_c changes on a common scale after irradiation the deposited energy density has been calculated. In Fig. 15 the T_c and $\Delta\rho_o$ (change of the residual resistivity) is shown as a function of the deposited energy density Q. An increase for the resistively measured T_c^{res} and $\Delta\rho$ is seen for increasing Q up to 10^{24} eV/cm^3 ($\sim$ 15 eV/at). T_c^{res} is nearly independent on Q, however a strong increase of $\Delta\rho_o$ is noted for $Q \geq 10^{26}$ eV/cm^3. The inductively measured T_c^{ind} for Ar irradiation shows a quite different behavior as a function of Q as T_c^{res}. This difference, which has not been observed to occur for N irradiated Re films, is thought to be due to a rather inhomogeneous distribution of the vacancies after Ar-irradiation. The further increase of T_c^{ind} at high Q is thought to be due to vacancies trapped at dislocation. The annealing behavior of high and low dose irradiated films support this trapping model. For low dose irradiated samples complete annealing was observed for ρ_o and T_c in stage III ($\sim 0.19 * T_m$), clearly indicating that the vacancies are responsible for the T_c increase. For high dose irradiated samples the annealing behavior can be explained in terms of vacancies pinned to dislocations and successively being released during the annealing procedure /55/.

In chapter 2.2.1 it was discussed that the formation of supersaturated interstitial solid solutions will strongly distort the host lattice by weakening the transition metal bonding and by reducing the electron density. Lowering the electron density in Mo will shift the Fermi energy into a region of increased density of electronic states (DOS) and thus will enhance the electron-phonon-coupling. Broadening of the DOS will result

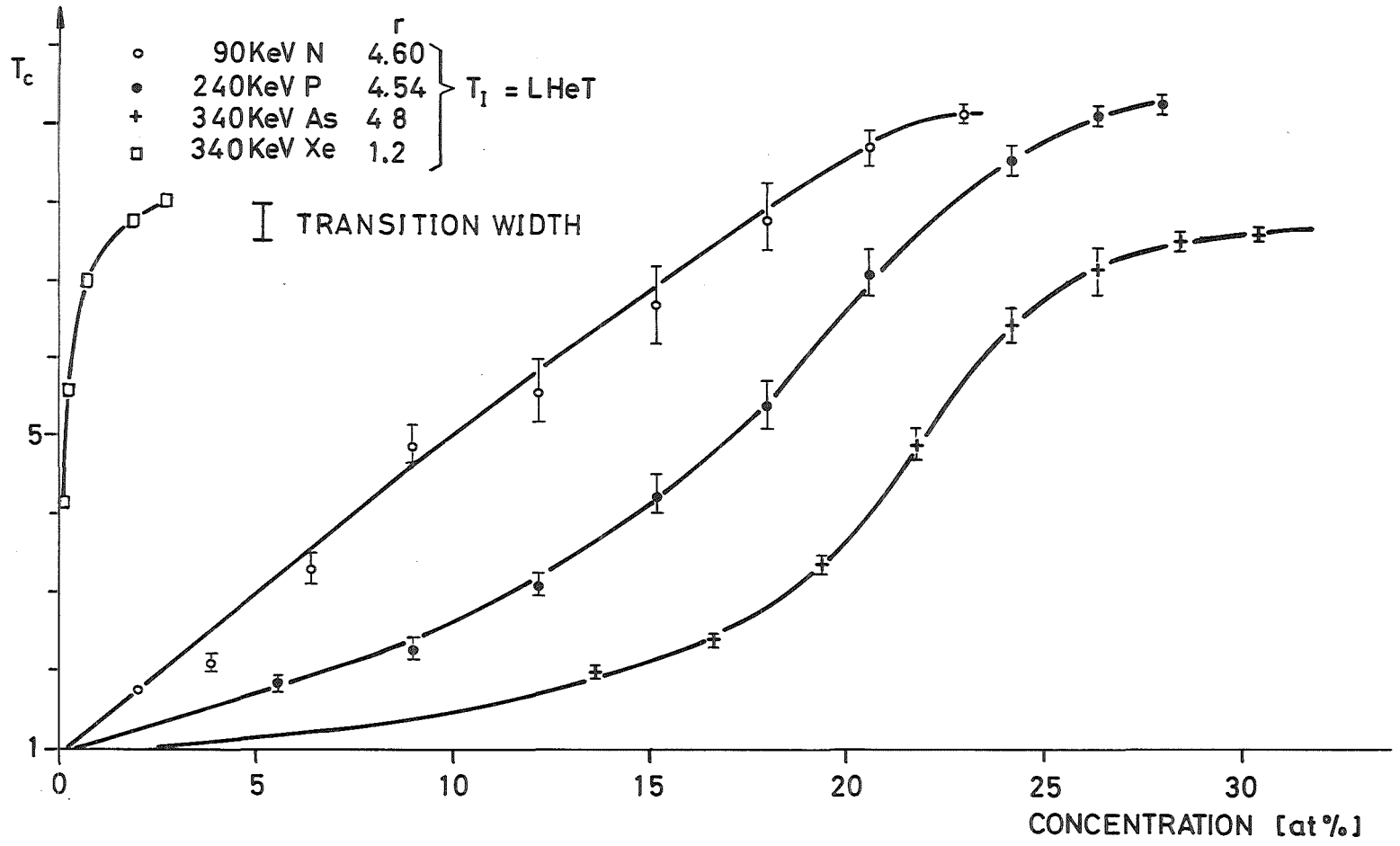

Fig. 16 Increase of T_c as a function of the concentration of implanted N, P, As and Xe ions in Mo films with various oxygen impurity contents /43/.

a similar enhancement. In Fig. 16 it is shown that T_c increases with increasing implnated impurity content. Implantation of very pure Mo films (residual resistivity ratio $\rho_{RT}/\rho_o \geq 4$) with noble gas ions will not affect T_c. For oxygen-contaminated however the Mo layers T_c will increase upon irradiation with Xe ions very steeply as it is shown in Fig. 16. As an explanation it is suggested that Mo-oxides are dissolved by Xe irradiation and that oxygen is recoiled into interstitial lattice sites and thus produces strong displacement fields with all the consequences as discussed above. Although the irradiations have been performed at liquid-helium temperature the solute-defect complexes are stable up to high temperatures /43/.

In conclusion, both intrinsic defects as well as irradiation induced impurity-defects complexes may strongly affect the physical properties of materials. Prior to implantation irradiations should be performed in order to see if such effects will influence the ion implantation results.

2.3.2 Defects in Compounds

Important intrinsic defects in compounds are deviations from the stoichiometric composition and anti-site lattice occupation. In refractory transition-metal compounds these deviations are due to the existence of vacancies on both sublattices. In compounds with A15 structure all lattice sites are usually occupied however deviations from stoichiometry may occur and atoms may be exchanged called anti-site defects. Most of the materials properties are strongly affected by deviations from the stoichiometric composition. For NbC_{1-c} T_c decreases from 11.8 to 1.2 K for the vacancy concentration increasing from 1 to 30%. In order to explain this large variation of T_c due to deviations from the stoichiometry, exact knowledge of the structural changes is necessary. Ion channeling measurements have been performed in NbC_{1-c} in the composition range $0.02 < c < 0.18$ in order to determine the local atomic displacements around carbon vacancies /56/. Angular yield curves measured on $NbC_{0.82}$, $NbC_{0.89}$ and $NbC_{0.98}$ single crystals

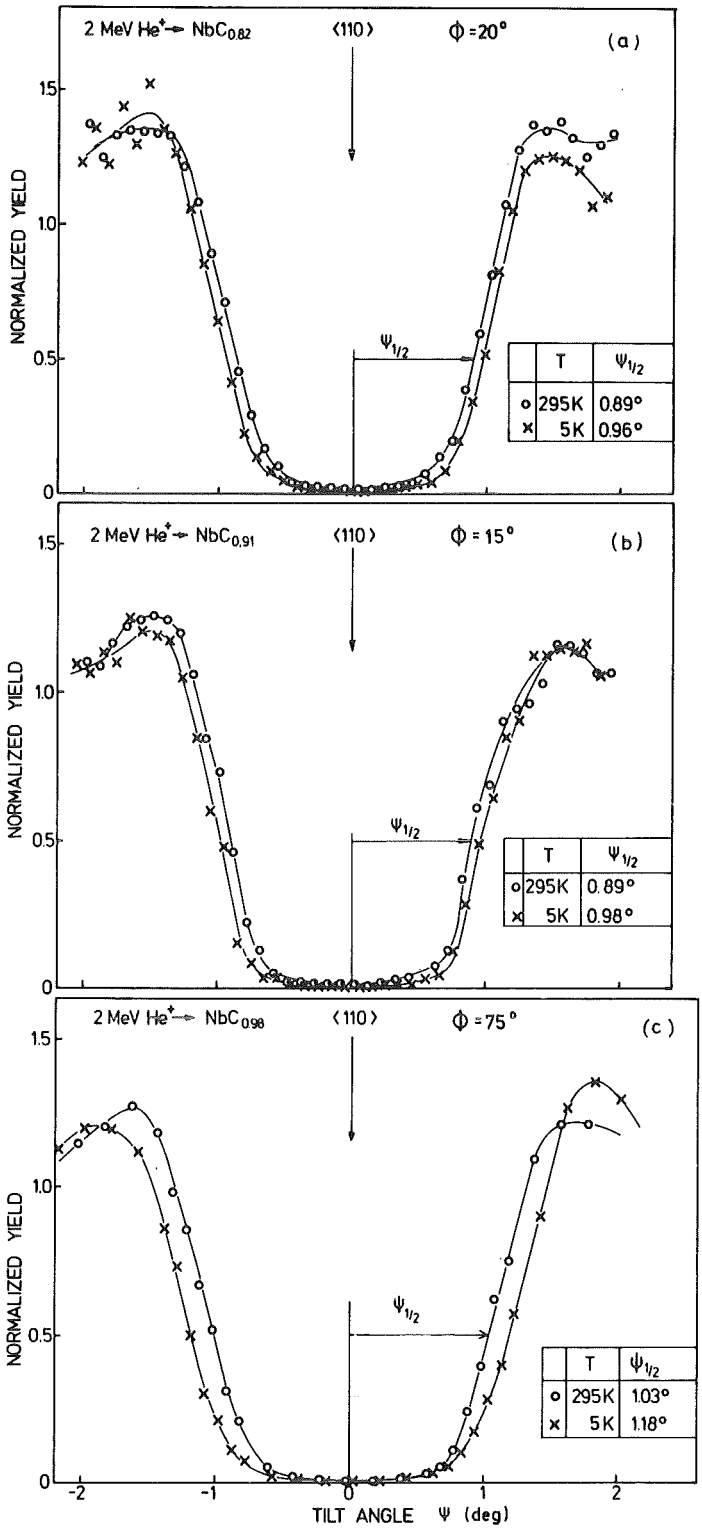

Fig. 17 Angular scans through the <110> direction of NbC_{1-c} single crystals with c = 0.18, 0.11 and 0.02 respectively, at temperatures of 295 and 5 K /56/.

at temperatures of 295 and 5 K are shown in Fig. 17. The critical angle $\psi_{1/2}$ and the minimum yield are both a measure of the average total (dynamic and static) atomic displacements. Assuming that the dynamic contribution is independent of c, the criticle angle is largest for the stoichiometric sample. The difference $\psi_{1/2}$ at 295 and 5 K is then largest and is due to temperature dependence of dynamic component. The absolute value is in agreement with the value obtained from neutron scattering measurements indicating that there is no contribution of static displacements (Fig. 17c). With increasing deviation from stoichiometry (Fig. 17b and Fig. 17a) $\psi_{1/2}$ decreases indicating the increasing value of the average static component. In the range of low vacancy concentration ($c \leq 0.1$) the displacements of the first Nb neighbors around a C-vacancy were $u_1 = 0.12$ Å obtained by using a specific local defect model in the Monte Carlo simulations (solid lines in Fig. 17 /56/). For high vacancy concentration the analysis with a model of mean Gaussian-distributed displacements of all atoms yields the same values as for the specific defect model.

Recent irradiation results of stoichiometric, reactively sputtered NbC and NbN thin films have shown a strong decrease of T_c and of the lattice parameter a_o with increasing fluence, indicating that vacancies and displaced host lattice atoms are produced by irradiation with He and Ar ions /57/.

High T_c superconductors with A15 crystal structure are very sensitive to radiation damage as has been discussed already in chapter 2.2.2. In V_3Si thin films T_c was found to decrease from 17 to 1.4 K upon irradiation at room temperature with $4 \cdot 10^{16}$ He-ions at 300 keV /58/. The nature of the defects present has been studied applying the channeling analysis to a V_3Si single crystal irradiated with a similar He fluence and energy /59/. Angular yield curves as shown in Fig. 18 from V-rows in the <100> as well as in the <110> channeling directions performed near the surface at a thickness corresponding to the thickness of the thin films revealed a noticable narrowing after implantation of $4 \cdot 10^{16}$ He/cm^2 at room temperature. The defect model assumed in the computer

simulation (solid lines in Fig. 18) consisted of all V atoms slightly displaced from their lattice sites. The displacements were assumed to have Gaussian distribution with a rms-amplitude of 0.05 Å perpendicular to the <100> and <110> channeling directions.

In summary, static displacements and anti-site defects have been observed by channeling and by thin film X-ray analysis and are probably both responsible for the large T_c degradation observed in irradiated high T_c superconductors with A15 structures. In refractory materials T_c decreases with increasing vacancy concentration. The influence of static displacement fields on the physical properties is not clarified up to now.

2.3.3 Radiation Induced Phase Transformations

Compounds with complex crystal structures may during irradiation undergo a complete phase transformation into simpler alloy structures or may be rendered into a structure having no long-range periodicity. Up to now it is not yet possible to predict which phase will be stable, for example a simple supersaturated alloy, compound, or the amorphous phase. In general the transformations occur more readily the heavier the incident particle and the lower the substrate temperature during irradiation. Besides phase transformations observed during irradiation of compounds with complex crystal structures, implantation of metalloid ions known as "glass-formers" may transform transition metals into the amorphous state. In this case the transformation process can be studied with the concentration of the glass-former as a parameter. Two different crystalline to amorphous transition mechanisms have been observed and will be discussed in the following.

The problem of irradiation induced phase transformations of superconductors with A15 structure and subsequent thermally activated retransformation into crystalline A15 phases has drawn con-

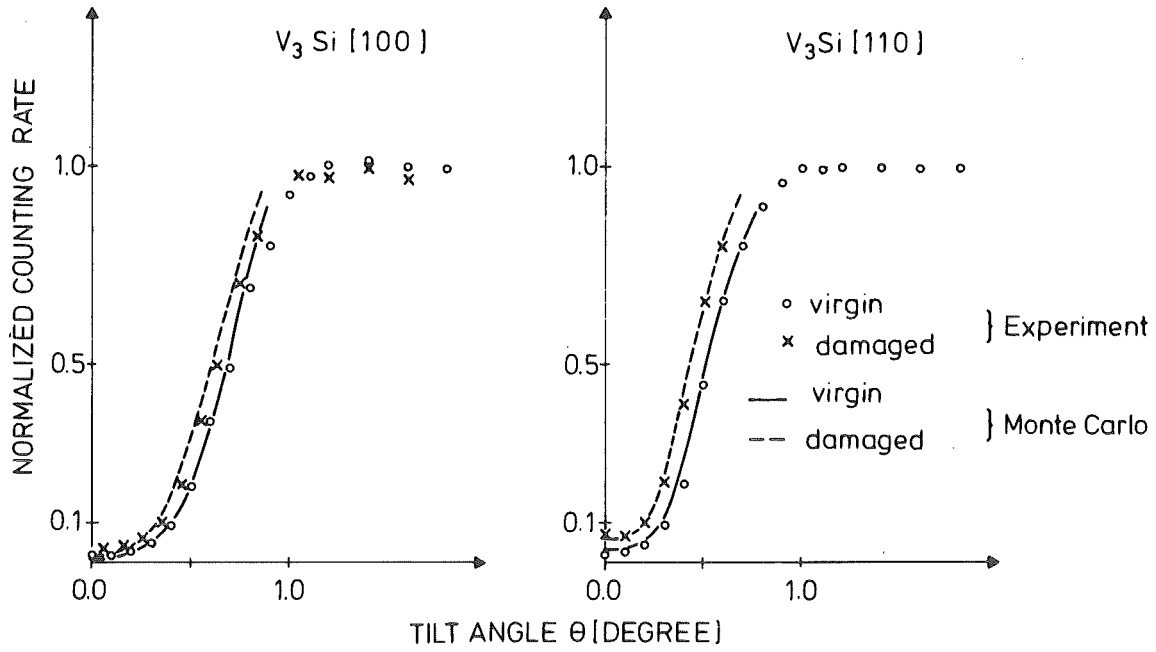

Fig. 18 Angular scans through the ‹100›- and ‹110›-crystal directions of V_3Si. Results are presented before and after irradiation with 4 x 10^{16} He/cm^2, 300 keV at RT and are compared to calculated angular scan curves /56/.

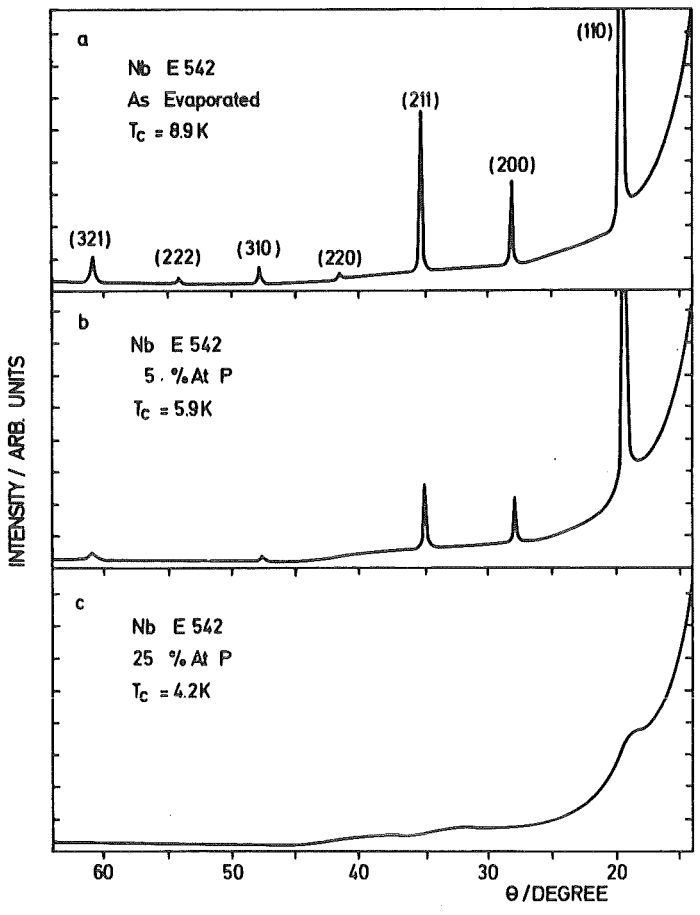

Fig. 19 X-ray spectra of a Nb-film before (a) and after homogeneous implantation of 5% At (b) and 25% At (c) P /66/.

siderable interest in recent years. The transformation behavior has been studied for V_3Si /60/ for Nb_3Ge /61/ and for Nb_3Ir /62/ where amorphous material was formed upon irradiation. The annealing behavior of V_3Si yields the A15 phase irrespective of the annealing procedure used. For Nb_3Ge the annealing results have been discussed in chapter 2.2.2.

The amorphization process of Nb_3Ge thin films irradiated with He as well as with Ar-ions was studied using X-ray diffraction. With increasing ion fluence the static Debye-Waller factor and the lattice parameter were found to increase steeply. At higher fluences a total loss of X-ray intensity is noted and is attributed to the formation of amorphous regions. From these results it may be argued that the formation of amorphous zones does not occur in a direct manner by rapid quenching from collision cascade regions but is probably forced by strain fields which cause the measured displacements fields. These observations are in good agreement with results obtained from channeling experiments on He- and Ar-irradiated V_3Si single crystals where static displacements fields and amorphous zones have also been observed /60/. For He-irradiations of V_3Si at room temperature the displacement amplitude and thus the accompanying strain is too small to cause a crystalline to amorphous transition.

Radiation damage usually causes a depression of T_c in high T_c A15 superconductors whereas some low T_c A15 materials reveal an increase of T_c with increasing disorder. T_c of Nb_3Ir (T_c = 2 K) was found to increase up to 5.7 K with increasing Kr-ion fluence. Defect analysis resulted in the following interpretation a) the amorphous phase has a T_c of 5.7 K, b) the A2 phase has a T_c below 2 K, c) static displacements probably cause a T_c-increase of the A15 phase up to about 3 K /62/.

Irradiation of Nb_3Al results in the formation of a supersaturated A2 solid solution. Upon annealing of this solid solution, A15 material is formed with a T_c-value higher than that of the starting material /63/. In the transformation process the A15 X-ray line intensity was found to decrease without braodening.

The average static amplitudes were small and increased only slightly during the transformation process.

Irradiations were also performed on sputtered $Nb_{1-x}Si_x$ films containing a mixture of different phases: A2, A15, Ti_3P, Cr_5B_3 /64/. After irradiation with $1 \cdot 10^{16}$ Ne/cm^2 at 350 keV at room temperature the A15, Ti_3P and Cr_5B_3 phases transformed into the amorphous phase, whereas the A2 phase was little affected. The thermally activated retransformation into the A15 phase was found to depend on the degree of disorder introduced during irradiation as was discussed for Nb_3Ge in chapter 2.2.2.

Amorphization processes by ion implantation have been extensively studied in semiconductors /4,6/ while much less work has been performed in metals /43,45,65/. In metals the size and the chemical bonding abilities of the implanted ion species are important parameters for the stabilization of defect structures. The amorphization process of Nb layers by phosphorus ion implantation will be discussed here in more detail /66/. Evaporated Nb thin films were homogeneously implanted with phosphorus ions in the concentration range from 2.5 to 20 at.%. Typical X-ray spectra before and after implantation are shown in Fig. 19. With increasing phosphorus concentration the X-ray lines from the crystalline material decreases until the lines disappear complete at concentrations of 20% At (≡ 16.7 at.%). In contrast to the large displacement amplitudes noted for N implanted in Nb (see chapter 2.2.1) the modified Wilson plots for P in Nb shown in Fig. 20 yield a displacement amplitude of 0.1 Å independent of the P concentration. From the axial section values in Fig. 20 the volume transformed into amorphous material can be obtained and is 5, 23 and 58 % of the layer for the P concentration of 2.5, 5 and 7.5 % respectively. The results from the channeling analysis (see Fig. 21) indicating a direct backscattering peak at 10 at.% P and reaching the random level at 15 at.% P are in good accordance with the X-ray results. The amorphization process depends on the implanted ion species. While with N implantation the host lattice is distorted with static

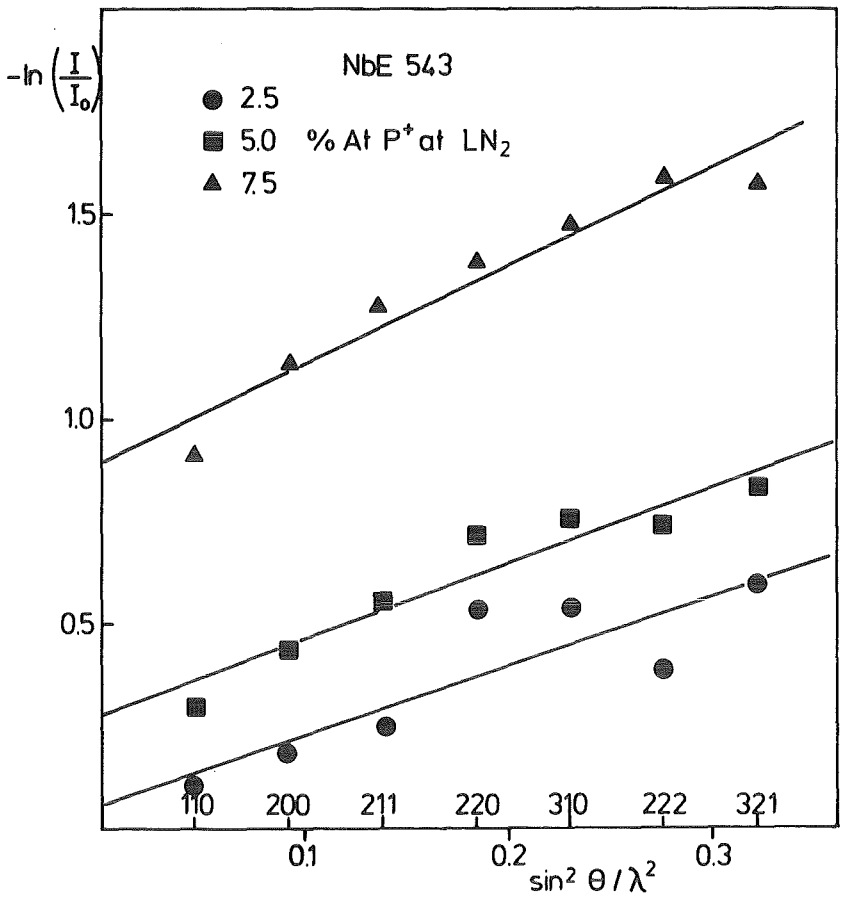

Fig. 20 Modified Wilson plots from a P-implanted Nb-film for three P-concentrations /66/.

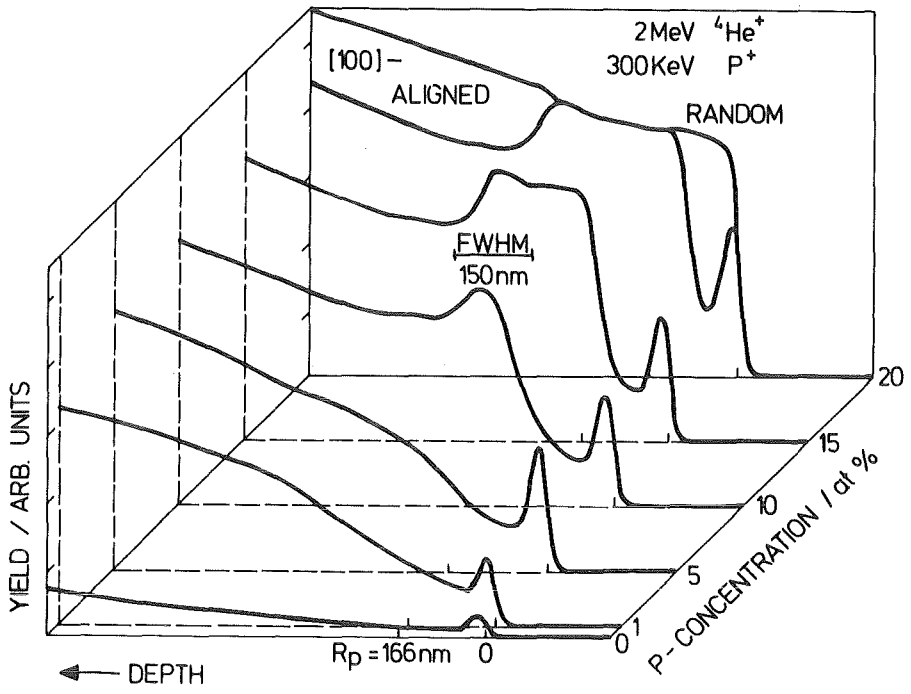

Fig. 21 Backscattering spectra from a <100>-aligned Nb-single crystal implanted with different concentrations of P^+ ions /66/.

displacements and a strong increase of the lattice parameters occurs accompanied by a weakening of the bonds of all the host atoms, by P implantation the disordering process is discontinuous in a sense that amorphous regions are present in a less distorted crystalline matrix. The amorphization process as a function of impurity concentration can be explained by quenching from high energy density cascades however further experiments are necessary to draw more definite conclusions on the dynamical processes together with the impurity defect interaction leading to amorphization.

In summary metastable solid solutions and amorphous phases can easily be obtained by ion irradiation and implantation. The results obtained for metals can not simply be treated by collisional theories. The amount of volume transformed into the amorphous state depends on the substrate temperature during irradiation and thus on thermal or radiation enhanced diffusion properties as well as on the chemical abilities of the atoms in the mixture. Differences in the free energies of the different competing metastable phases during irradiation will provide driving forces for phase transformations.

Materials modification by ion irradiation and implantation is a very exciting and fruitful area as well as from a pure scientific and an applied point of view. In this short review some examples have been summarized to demonstrate the potentials in this field of materials science.

References

/1/ G. Carter and J.S. Colligon; Ion Beam Bombardment of Solids, Heinemann Educational Books Ltd., London (1968).

/2/ M.W. Thompson; Defects and Radiation Damage in Metals Cambridge, Univ. Press (1969).

/3/ Chr. Lehmann; Interaction of Radiation with Solids and Elementary Defect Production, North-Holland Publishing Company, Amsterdam (1977).

/4/ J.W. Mayer, L. Eriksson and J.A. Davies, Ion Implantation in Semiconductors, Academic Press (1970).

/5/ R.S. Nelson, G. Dearnaley, J.H. Freeman and J.L. Stevens; Ion Implantation in Semiconductors, North-Holland (1973).

/6/ G. Carter and W.A. Grant; Ion Implantation of Semiconductors, Contemporary Electrical Engineering Series, Edward Arnold, London (1976).

/7/ Treatise on Materials Science and Technology, Vol. 18, Ion Implantation, ed. J.K. Hirvonen, Academic Press, New York (1980).

/8/ Applications of Ion Beam to Metals, eds. S.T. Picraux, E.P. EerNisse, F.L. Vook, Plenum Press, New York (1974).

/9/ Conf. Proc. on Ion Beam Modification of Materials (IBMM) Budapest (1978), ed. J. Gyulai, T. Lohner, E. Pasztor in Rad. Eff. 48 (1980).

/10/ IBMM, Albany (1980), eds. R.E. Bennenson, E.W. Kaufmann, G.L. Miller, W.W. Scholz, Nucl. Instr. and Meth. 182/183 (1981).

/11/ IBMM, Grenoble (1982), eds. B. Biasse, G.L. Destefanis, J.P. Gailliard, Nucl. Instr. and Meth. 209/210 (1983).

/12/ J. Lindhard, V. Nielson and M. Scharff, Mat. Fys. Medd. 36, 10 (1968).

/13/ J.A. Davies in Surface Modification and Alloying, eds. J.M. Poate, G. Foti, Plenum Publishing Corp. (1983).

/14/ O.B. Firsov, Sov. Phys. JETP 5, 1133 (1957).

/15/ W.S. Johnson and J.F. Gibbons, Projected Range Statistics in Semiconductors (Stanford Univ. Bookstore, 1969).

/16/ D.K. Brice, Ion Implantation Range and Energy Deposition, Sandia Labs. Albuquerque, New Mexico, SAND 75-0622 Report, (1977).

/17/ K.B. Winterbon, Ion Implantation Range and Energy Deposition Distribution, Vol. 2, Plenum Press, New York (1975).

/18/ J.P. Biersack, L.G. Haggmark, Nucl. Instr. and Meth. 174 (1980) 257.

/19/ J. Lindhard, M. Scharff, H.E. Schiott, Mat. Fys. Medd. 33 (1963) 14.

/20/ W.K. Chu, J.W. Mayer and M.-A. Nicolet, Backscattering Spectrometry, Academic Press, N.Y. (1978).

/21/ J.P.S. Pringle, J. Electrochem. Soc. 121 (1974) 45.

/22/ L. Eriksson, Phys. Rev. 161 (1967) 235.

/23/ H.J. Smith, Rad. Effects 18 (1973) 55, 65 und 73.

/24/ E.V. Kornelsen, F. Brown, J.A. Davies, B. Domeij and G.R. Piercy, Phys. Rev. 136 (1964) A849.

/25/ O. Meyer, Nucl. Instr. and Meth. 70 (1969) 279/285.

/26/ Y. Yamamura, Y. Kitazoe, Rad. Effects 39 (1978) 251.

/27/ R.S. Walker and D.A. Thompson, Rad. Effects 37 (1978) 113.

/28/ G.H. Kinchin and R.S. Pease, Report Prog. Phys. 18 (1955) 1.

/29/ D.A. Thompson and R.S. Walker, Rad. Effects 26 (1978) 91.

/30/ O. Meyer in Ref. /7/, p. 415
J. Geerk, K.G. Langguth, G. Linker, O. Meyer, Transactions on Magnetics IEEE 13 (1977) 662.
J. Geerk, K.G. Langguth, Solid State Commun. 23 (1977) 83.
J.M. Lombaard, O. Meyer, Rad. Effects 36 (1978) 83.
J. Geerk, Rad. Effects 48 (1980) 35.
R. Kaufmann and O. Meyer, Rad. Effects 52 (1979) 53.

/31/ H. Bülow and W. Buckel, Z. Phys. 145 (1956) 141.

/32/ M. Holz, P. Ziemann and W. Buckel, Phys. Rev. Lett. 51 (1983) 1584.

/33/ R. Kaufmann, G. Linker and O. Meyer, Nucl. Instr. and Meth. 218 (1983) 647.

/34/ D.K. Brice, Inst. Phys. Conf. Ser. No. 28 (1976) 334.
P.H. Dederichs, Chr. Lehmann, H. Wegener, phys. stat. sol. 8 (1965) 213.
W.W. Anderson, Solid State Electronics 11 (1968) 481.

/35/ J.M. Poate and A.C. Cullis, in Ref. /7/, p. 85.

/35b/ D.K. Sood and G. Dearnaley, Rad. Effects 39 (1978) 157.

/36/ H.W. Alberts, O. Meyer and J. Geerk, Rad. Effects 69 (1983) 61.

/37/ O. Meyer and G. Haushahn, Nucl. Instr. and Meth. 56 (1967) 177.

/38/ A. Turos, O. Meyer and J. Geerk, Applied Physics A28 (1982) 99.

/39/ J. Geerk and O. Meyer, Rad. Effects 63 (1982) 133.

/40/ T. Hussain and G. Linker, Solid State Commun. 44 (1982) 133.

/41/ B. Stritzker and H. Wühl, in G. Alefeld, J. Völkl (eds.); Hydrogen in metals, Springer, Berlin (1978).

/42/ C.C. Koch, J.O. Scarbrough and D.M. Kroeger, Phys. Rev. B9 (1974) 888.

/43/ O. Meyer, Inst. Phys. Conf. Ser. No. 28 (1976) 168.

/44/ G. Linker, Rad. Effects 47 (1980) 225 and Nucl. Instr. and Meth. 182/183 (1981) 501.

/45/ G. Linker and O. Meyer, Sol. State Commun. 20 (1976) 695.

/46/ A. ul Haq and O. Meyer, J. of Low Temp. Phys. 50 (1983) 123.

/47/ G. Linker, Nucl. Instr. and Meth. 209/210 (1983) 969.

/48/ K. Gamo, H. Goshi, M. Takai, M. Iwaki, K. Masuda and S. Namba Jap. Appl. Phys. 16 (1977) 1853.

/49/ S. Matteson, B.M. Paine, M.G. Grimaldi, G. Mazey and M.A. Nicolet, Nucl. Instr. and Meth. 182/183 (1981) 43.

/50/ G. Linker, R. Smithey, O. Meyer, J. of Phys. F (1984).

/51/ O. Meyer, E. Friedland, B. Scheerer, Sol. State Commun. 39 (1981) 1217.

/52/ J.M. Lombaard, G. Linker, O. Meyer, J. of the Less-Common Metals 96 (1984) 191.

/53/ O. Meyer, Trends in Physics: 5th General Conf. of the EPS, Istanbul (Dorobantu, I.A. ed.) Central Inst. of Physics, Bucharest 1982, p. 821.

/54/ J. Geerk, Sol. State Commun. 33 (1980) 761.

/55/ A. ul Haq and O. Meyer, J. of Low Temp. Phys. 49 (1982) 151.

/56/ R. Kaufmann and O. Meyer, Phys. Rev. B28 (1983) 6216.

/57/ V. Jung, M. Kraatz, O. Meyer, R. Smithey, Verhandl. DPG (VI) 19 (1984) 488.
N. Kobayashi, R. Kaufmann, G. Linker, Verhandl. DPG (VI) 19 (1984) 489.

/58/ O. Meyer and B. Seeber, Sol. State Commun. 22 (1977) 603.
O. Meyer, J. Nucl. Mat. 72 (1978) 182.
O. Meyer, R. Kaufmann, B.R. Appleton, Y.K. Chang, Solid State Commun. 39 (1981) 825.

/59/ R. Kaufmann and O. Meyer, Rad. Effects 40 (1979) 161.

/60/ O. Meyer, G. Linker, J. of Low Temp. Phys. 38 (1980) 747.

/61/ J. Pflüger, O. Meyer, Solid State Commun. 32 (1979) 1143.

/62/ O. Meyer, R. Kaufmann, R. Flükiger, Proc. Superconductivity in d- and f-Band Metals (1982), eds. W. Buckel and W. Weber, KfK 1982, ISBN 3-923704 00 3, p. 111.

/63/ U. Schneider, G. Linker, O. Meyer, J. of Low Temp. Phys. 47 (1982) 439.

/64/ J. Ruzicka, E.-L. Haase, O. Meyer, Proc. Superconductivity in d- and f-Band Metals (1982), eds. W. Buckel and W. Weber, KfK 1982, ISBN 3-923704 00 3, p. 103.

/65/ W.A. Grant, Nucl. Instr. and Meth. 182/183 (1981) 809.

/66/ G. Linker, Nucl. Instr. and Meth. 209/210 (1983) 969.